UNIVERSITY COLLEGE LONDON

Faculty of Mathematics and Physical Sciences

Department of Physics & Astronomy

CLUSTERS AND COSMIC ONIONS: A DESCRIPTION OF GALAXY DYNAMICS IN THE QUASI-LINEAR REGIME

Thesis submitted for the Degree of Doctor of Philosophy of the University of London

by

Emily Anne Hall

Supervisors:
Prof Sarah Bridle
Dr Filipe Abdalla

Examiners:
Prof Catherine Heymans
Dr Benjamin Joachimi

September 27, 2018

For my wonderful, eccentric and truly inspirational family

I, Emily Anne Hall, confirm that the work presented in this thesis is my own. Where information has been derived from other sources, I confirm that this has been indicated in the thesis.

Abstract

This thesis investigates the dynamics of galaxies around clusters in the quasi-linear regime, with the ultimate aim of providing cluster mass constraints which can be combined with weak lensing measurements in order to perform tests of General Relativity. Dark matter simulations are populated with galaxies using a halo occupation distribution, and used to develop and test models which describe different aspects of galaxy dynamics around clusters. A heuristic analytical model is presented describing the infall profile of galaxies onto a cluster of given mass, which is shown to fit the simulations remarkably well on quasi-linear scales. The velocity dispersion of galaxies in the simulations is also examined, and a model developed which describes how this effect varies as a function of position relative to the cluster centre. These models of galaxy infall and velocity dispersion are combined to provide predictions of the cluster-galaxy redshift space correlation function, or cosmic onion, which show a relatively good agreement with the simulations. The cosmic onion model is used to obtain cluster mass constraints from redshift space distortions observed in the simulations, in order to demonstrate the robustness of this method. In this work the uncertainty on cluster mass was estimated with all other halo parameters fixed, and was found to be approximately 2% at the 2σ confidence level for a halo mass of $\sim 10^{13}$ $\mathrm{M}_{solar}h^{-1}$. However in practice the accuracy of these constraints depends on how many free parameters are considered in the halo occupation distribution, as some are degenerate with the cluster mass. The techniques developed here can be applied to observational data from the upcoming generation of spectroscopic galaxy surveys, potentially improving constraints on the dynamic mass of clusters measured from redshift space distortions.

Acknowledgements

First and foremost, I would like to thank my supervisor Sarah Bridle for everything she has done for me over the past several years, both academically and in helping me overcome personal challenges. She has been utterly invaluable as both a mentor and friend, and it is hard to imagine how I would have completed this PhD without her understanding and support - thank you.

During the course of my PhD I have been privileged to work with many people who have inspired me academically, and contributed to the work presented in this thesis. Firstly I would like to thank my fellow UCL cosmologists, including Adam Hawken, Donnacha Kirk, Filipe Abdalla, Joe Zuntz and Tomasz Kacprzak, for many interesting chats which helped develop my understanding of fundamental cosmological principles. I would especially like to thank Cristiano Sabiu for his academic support and friendship, and his very effective 'pints for plots' scheme. I am indebted to Ravi Sheth for providing inspiration and ideas which contributed to the work in this thesis, and also to Bhuvnesh Jain for many interesting discussions. I am extremely grateful to Anna Cabre for her help in both obtaining and processing simulation data, which provided a vital contribution to the work presented here. I would also like to thank Rachel Bean and Eva-Maria Mueller for an exciting collaboration, and providing helpful insights into the potential applications of this work during many enlightening discussions. Finally, I would like to express gratitude to my PhD examiners Catherine Heymans and Benjamin Joachimi, and also to Jodrell Bank Centre for Astrophysics at the University of Manchester for hosting me as a visitor while I completed this thesis.

I have been lucky enough to form some of the best friendships in my life whilst at UCL, and would like to thank Helen, Harps, Farah, my fellow musketeers Ingo and Luke, Silvia,

Patrick, Steph and Roger amongst others for their continued support, and for making my time at UCL unforgettable. I am extremely grateful to my wonderful friends Zoe, Debs, Ellie, Hev, Suzanne and Karen for all their encouragement while I was thesis writing, and would especially like to thank Sam and Alec for their kindness and support during this time. I owe a great deal to my teacher David Fishwick for nurturing my interest in Astrophysics at school, and inspiring me to pursue this as a career. I would also like to thank Pete for his help and encouragement when I applied to do a PhD in the first place. I am grateful to all my other close friends, particularly Yssy, Caroline, Jo, Amadi, Sam S, Jim and Alex, for their incredible support and lots of stress relieving trips to the pub over the past several years. A heartfelt thank you to Tony for all his patience, love and support especially towards the end of my PhD, and for having faith in me both as a scientist and a person - I will always be grateful to you.

Finally, I would like to thank my family to whom this thesis is dedicated, for all their love, encouragement and inspiration over the years. I am infinitely grateful to my mum who has always believed in me and given her unconditional support in every way possible, and also for her wonderful musical interpretation of my thesis. I want to hugely thank my dad, who understands me probably better than anyone, for always being there to provide his wise and often darkly comic perspective on things. I am incredibly grateful to my brother John for inspiring strength and bringing out the best in me, and somehow managing to make me laugh even in the most difficult of situations. I would also like to thank Milo for his humour, kindness and faith in me, and Nestor for all his support and generosity. I am hugely indebted to Tia for her unwavering and relentless encouragement during the final stages of my PhD, and sincerely appreciate the psychological support which has helped me to discover what I'm really capable of. I would lastly like to thank my nana, whose resilience and zest for life has always inspired me to never give up.

"The Big Bang... Everyone stood well back"

Eddie Izzard

Contents

This page was intentionally left blank

List of Figures

List of Tables

This page was intentionally left blank

Chapter 1

Introduction

The concept of an expanding universe is one which is taken for granted in modern cosmology, however this is an idea which only recently became widely acknowledged in historical terms. At the beginning of the last century the prevailing belief was in a static universe, which existed in a constant state unchanged by the passing of time. The theory was accepted despite the fact that when the law of gravity was first discovered, Isaac Newton himself realised that if this was true then a finite universe would collapse in on itself due to gravitational attraction. When Albert Einstein developed the General Theory of Relativity in the early 1900s his equations predicted that the universe must be either expanding or contracting, however an assumption that this was not the case led him to introduce a constant term into the solution which would cancel out the effect of gravity on large scales, resulting in a static universe. This so called cosmological constant Λ was later described by Einstein as his "greatest blunder", when it was discovered by Edwin Hubble in 1929 that the universe appeared to be expanding. Hubble's observations of Cepheid variable stars in distant galaxies showed a linear relation between their distance and redshift, indicating that the further away a galaxy was the faster it seemed to be receding. These measurements provided conclusive evidence that the universe is in a state of continual expansion, and it was soon realised that the logical consequence of this was that at some time in the past the entire universe and everything it contains must have existed at a single point. This idea later came to be known as the Big Bang theory, and provides the basis for our current understanding of the universe and how it has evolved from the initial

singularity up to the present day.

The universe contains a large quantity of matter in various different forms, all of which exert a gravitational force causing an attractive pull between any objects which have mass. However small the magnitude of this force is, it should cause the expansion to slow producing either a perpetually expanding universe which continually decelerates or, in the case of a high enough matter density, a contraction which eventually results in a big crunch. The surprising discovery made at the turn of this century that the expansion currently appears to be accelerating provides arguably the biggest puzzle in modern cosmology, and has brought the concept of a cosmological constant back to the forefront of scientific thinking in order to explain these unexpected observations. It has been suggested that a mysterious fluid known as dark energy, which produces a similar effect to that arising from Λ in the equations of General Relativity, could exist throughout the universe and come to dominate at late times when the matter density becomes sufficiently low. The idea has also been postulated that some correction needs to be made to General Relativity itself, effectively altering the effect of gravity on large scales. Obtaining methods by which to differentiate observationally between these scenarios provides one of the most exciting challenges in cosmology today, and is the primary motivation behind the work that will be presented here.

1.1 The evolving universe

Since the groundbreaking discovery that we reside in a universe which is currently in a state of continual expansion, the attempt to accurately measure and parameterise its evolution has been at the forefront of modern cosmology. The relation between distance and recession velocity of galaxies provides evidence of how the expansion rate has evolved over time, and was initially measured by Hubble (1929) as shown in figure 1.1. The observed expansion history provides a fundamental measure of both the contents and geometry of the universe, and also the physical laws which governed its evolution from the Big Bang up to the present day. This endeavour to study the expansion history using observations of distant galaxies has allowed cosmologists to gain a greater understanding of the nature of space and the different components which contribute to the energy density in the universe, and also make predictions about its subsequent evolution and ultimate fate. In this section the parameterisation used to describe an expanding universe within

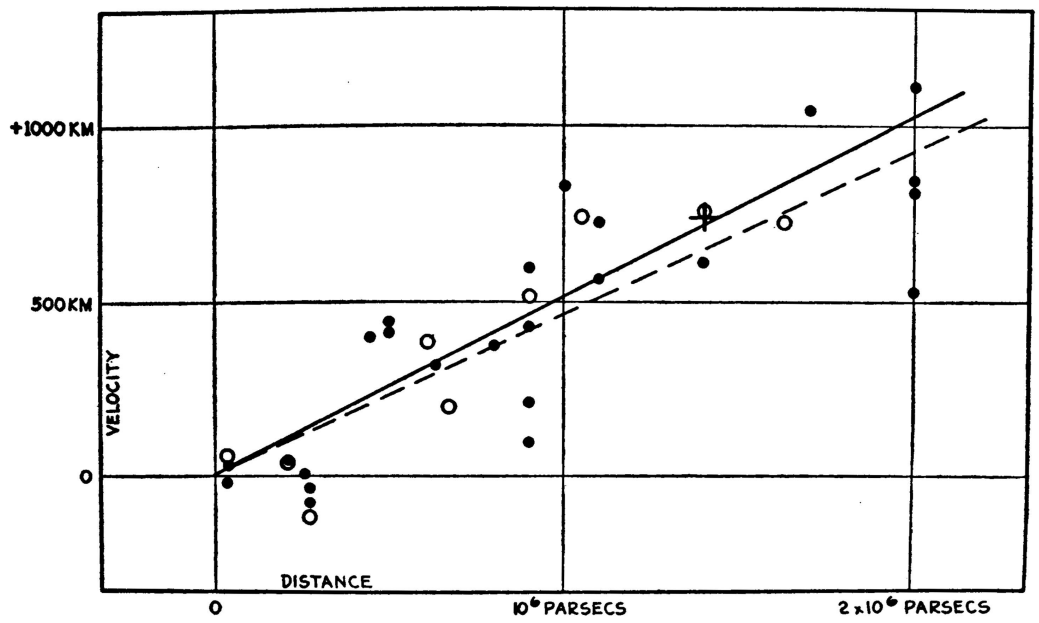

Figure 1.1. The first evidence for an expanding Universe (Hubble 1929).

the framework of General Relativity is introduced, and the dependence on both spatial curvature and the density evolution of its constituents is discussed. This is known as the Standard Model of Cosmology, and currently provides the most accurate description of how the universe behaves on large scales. An in depth discussion of the concepts outlined below can be found in several textbooks and review papers, see for example Weinberg (1972), Misner et al. (1973), Peebles (1980), Padmanabhan (1993), Peacock (1999), Bartelmann & Schneider (2001), Ryden (2003) and Schneider (2006).

1.1.1 Framework of General Relativity

The General Theory of Relativity was first published in 1916 by Albert Einstein, and almost a century later still provides the foundation for our current understanding of the large scale universe. The theory offered a new and revolutionary perspective on the nature of gravity, describing it as an effect which arises from the curvature of space and time around matter. This was eloquently summarised in the words of eminent theoretical physicist John Wheeler: "Spacetime tells matter how to move; matter tells spacetime how to curve". In General Relativity, spacetime is described as a four-dimensional manifold in which the separation between two events is governed by the metric tensor $g_{\mu\nu}$, which

is a dynamic field that can be effected by the presence of mass-energy. Einstein's field equations provide the following relation between $g_{\mu\nu}$ and the stress-energy tensor $T_{\mu\nu}$ of a given mass:

$$R_{\mu\nu} - \frac{1}{2}g_{\mu\nu}R + g_{\mu\nu}\Lambda = \frac{8\pi G}{c^4}T_{\mu\nu} \tag{1.1}$$

where $R_{\mu\nu}$ is the Ricci curvature tensor, R is the scalar curvature, Λ is the cosmological constant, G is Newton's gravitational constant and c is the speed of light in a vacuum. The indices μ and ν represent the tensor components and range from 0 to 3, denoting the four basis vectors of time plus three spatial dimensions. The above equation describes how spacetime is distorted by mass-energy, and the resulting effect on the motion of nearby particles. Thus the observed deflection of matter and light around massive objects, which we attribute to a gravitational force, is actually due to particles following the shortest possible path between two points, a geodesic in curved spacetime.

General Relativity provides a fundamental basis for the Friedmann-Lemaître-Robertson-Walker (FLRW) cosmological model, which was developed over the subsequent decades and uses assumptions of homogeneity and isotropy to obtain an exact solution of Einstein's field equations. In this model, a comoving spatial coordinate system is defined which is at rest relative to the Hubble expansion, and it is assumed that all measurements taken by fundamental observers from within this frame of reference are both isotropic and homogeneous, when averaged over sufficiently large scales. The comoving separation $\mathbf{x}$ can therefore be related to the physical or proper distance $\mathbf{d}(t)$ using a time-dependent scale factor $a(t)$ as follows:

$$\mathbf{d}(t) = a(t)\mathbf{x} \tag{1.2}$$

where the present day value is taken to be $a_0 = 1$. It is important to note that the scale factor does not display any spatial dependence, as if this were the case then the expansion rate would vary between different locations resulting in an inhomogeneous universe. The FLRW cosmological model outlined below describes the time evolution of the scale factor, and how this depends on the different energy-density components which make up the universe.

In the four dimensional spacetime of General Relativity, two events with an infinitesimal coordinate displacement dx^μ are separated by the line element ds^2 which is given

by

$$ds^2 = g_{\mu\nu} dx^\mu dx^\nu \tag{1.3}$$

where $g_{\mu\nu}$ is the metric tensor defined previously. In comoving coordinates, the mean motion is zero and the spatial part of the above metric vanishes to give $ds^2 = g_{00}dt^2$, providing an expression for the cosmic time. If this is equal to the eigentime, defined as $dt = c^{-1}ds$, of fundamental observers then it can be inferred that $g_{00} = c^2$. In an isotropic universe, it is required that clocks can be synchronised such that the metric tensor components $g_{0i} = 0$, where i denotes the spatial index ranging from 1 to 3. This prevents the identification of a particular direction in spacetime, which would violate the principle of isotropy. The above assumptions significantly constrain the metric given in equation 1.3, allowing its form to be simplified as follows:

$$ds^2 = c^2dt^2 - a^2(t)dl^2 \tag{1.4}$$

where dl^2 is the line element in comoving spatial coordinates. The above expression provides a description of the spacetime separation between two events in a universe that is either expanding or contracting, and which is both isotropic and homogeneous on cosmological scales.

In a uniformly curved three dimensional space, the line element dl^2 for an infinitesimal displacement described by the comoving spherical polar coordinates $dr, d\theta, d\phi$ is given by

$$dl^2 = dr^2 + S_\kappa^2(r)(d\theta^2 + d\phi^2 \sin^2\theta) \tag{1.5}$$

where $S_\kappa(r)$ depends on the spatial curvature as follows:

$$S_\kappa(r) = \begin{cases} \frac{1}{\sqrt{\kappa}} \sin(r\sqrt{\kappa}) & \kappa > 0 \\ r & \kappa = 0 \\ \frac{1}{\sqrt{|\kappa|}} \sinh(r\sqrt{|\kappa|}) & \kappa < 0 \end{cases} \tag{1.6}$$

where κ is the curvature constant, with $\kappa > 0$ indicating a positively curved space, $\kappa < 0$ a negatively curved space, and $\kappa = 0$ describing a flat, Euclidean geometry. The above definition of dl^2 can be substituted into equation 1.4 to give a general expression for

the separation of two events in four dimensional spacetime, assuming an isotropic and homogeneous universe, known as the FLRW metric:

$$ds^2 = c^2dt^2 - a^2(t)[dr^2 + S_\kappa^2(r)(d\theta^2 + d\phi^2 \sin^2\theta)] \tag{1.7}$$

This metric displays a high degree of symmetry, and was independently derived by Robertson (1935) and Walker (1935) who applied the principles of homogeneity and isotropy even before the observational evidence was available to support these assumptions. In reality the local universe is both anisotropic and inhomogeneous, with gravitationally bound systems such as galaxy clusters which do not expand along with the Hubble flow. However, on scales above ~ 100 Mpc current observations indicate that the conditions assumed by the FLRW cosmological model provide a valid approximation, and hence it can be used to accurately describe the large scale evolution of the universe.

The FLRW metric given in equation 1.7 is highly symmetric, and consequently it allows a solution describing the dynamics of spacetime to be derived from the field equations of General Relativity. In this cosmological model, the stress-energy tensor defined in equation 1.1 describes a homogeneous ideal fluid which is characterised by its density and pressure, both of which are time dependent. This allows Einstein's field equations to be simplified, resulting in two independent expressions as shown by Friedmann (1922) which describe the evolution of $a(t)$ as follows:

$$\left(\frac{\dot{a}}{a}\right)^2 = \frac{8\pi G}{3}\rho - \frac{\kappa c^2}{a^2} + \frac{\Lambda}{3} \tag{1.8}$$

and

$$\frac{\ddot{a}}{a} = -\frac{4\pi G}{3}\left(\rho + \frac{3p}{c^2}\right) + \frac{\Lambda}{3} \tag{1.9}$$

where $\rho(t)$ is the density and $p(t)$ is the pressure of an ideal fluid, which represents the total matter and energy contained within the universe. It is important to note that both $\rho(t)$ and $p(t)$ do not display any spatial dependence, as this would violate the principle of homogeneity. The Friedmann equations shown above can be combined to obtain the following relation, known as the fluid equation:

$$\dot{\rho} + 3\frac{\dot{a}}{a}\left(\rho + \frac{p}{c^2}\right) = 0 \tag{1.10}$$

This expression states that, for a given comoving volume, the decrease in energy is equal to the pressure multiplied by the increase in proper volume, and hence the fluid equation is equivalent to the first law of thermodynamics in a cosmological context. The above relations describe the evolution on large scales of an isotropic and homogeneous universe, and how this depends on both its geometry and the different physical properties of its contents.

1.1.2 The ΛCDM universe

The standard cosmological model which provides predictions consistent with current observations, known as ΛCDM, describes a spatially flat universe containing matter, radiation and a cosmological constant Λ. The fundamental components include both baryonic and cold dark matter (CDM), and radiation which consists of relativistic particles. The cosmological constant which is defined in equation 1.1 behaves effectively as a form of dark energy, producing the accelerated expansion observed at late times. On cosmological scales these individual components can be approximated as continuous ideal fluids, whose bulk properties are governed by a linear equation of state. This relates the energy density $\rho(t)c^2$ and pressure $p(t)$ of an ideal fluid as follows:

$$p = w\rho c^2 \tag{1.11}$$

where w is the equation of state parameter, which characterises the density evolution of each component as the universe expands. Although matter, radiation and Λ all have different equations of state, their contributions can be summed to obtain the total energy density and pressure. Consequently the fluid equation can be used to describe each of these components separately, provided there is no interaction between them. The scale factor dependence of ρ is derived by inserting the above relation into equation 1.10 to give

$$\rho = \rho_0 a^{-3(1+w)} \tag{1.12}$$

where ρ_0 is the component density at the present day, and w is assumed to be constant. This expression can be used to predict the density evolution of matter, radiation and Λ from their individual equations of state. The energy density contribution from each of these components is often expressed as a fraction of the critical density $\rho_c(t)$, defined as

the threshold value below which a universe containing only matter will continue to expand indefinitely. This corresponds to a spatially flat universe where $\kappa = 0$ and $\Lambda = 0$, which when substituted into the first Friedmann equation gives

$$\rho_c = \frac{3H^2}{8\pi G} \tag{1.13}$$

where $H(t) = \dot{a}/a$ is the Hubble parameter. The contribution from each individual component is then characterised by its density parameter, defined as $\Omega = \rho/\rho_c$. It is important to note that Ω represents the comoving density, and is therefore often expressed in the more physical form Ωh^2 to include the effect of spatial expansion.

The ΛCDM universe contains three fundamental components, each of which is governed by a different equation of state. The first of these is radiation, which includes all relativistic particles i.e. those that have a high mean thermal energy compared to their rest mass. Photons make up the largest fraction of this radiation component, with their energy density dominated by the Cosmic Microwave Background. There is also a significant contribution from relativistic neutrinos, the majority of which originate from the cosmic neutrino background. The radiation fluid exerts a pressure $p_r = \rho_r c^2/3$, which corresponds to an equation of state parameter $w = 1/3$. It can be seen from equation 1.12 that the radiation density therefore evolves as $\rho_r \propto a^{-4}$, which is a result of the spatial expansion between particles combined with their decrease in energy due to cosmological redshift. The radiation component has a current density parameter $\Omega_r \sim 10^{-4}$, and therefore provides a negligible contribution to the total energy density at the present day.

The second component of the standard cosmological model consists of non-relativistic matter, which contributes just over a quarter of the current total energy density in the universe. The majority of this component is made up of cold dark matter, which is an as yet unknown substance that does not interact electromagnetically. It therefore neither absorbs nor emits light, and has only been detected via its gravitational effect on visible objects. The remaining part of the matter component consists of baryons, which in an astronomical context are defined as all particles made up of protons and neutrons with their associated electrons. This baryonic matter is composed largely of light atomic nuclei formed during Big Bang Nucleosynthesis, with small quantities of heavier elements which are produced in stars by nuclear fusion. As both baryonic and dark matter are non-

relativistic, they can be considered as pressureless fluids and therefore have an equation of state parameter $w = 0$. The total matter density consequently evolves as $\rho_m \propto a^{-3}$, which is due to the increase in a given volume with time as the universe expands. The energy density of matter therefore falls less sharply than that of radiation, causing it to become dominant early in the expansion at $t \sim 50000$ yr. Observations by the Planck Collaboration et al. (2015) give a current best estimate of the present day matter density parameter $\Omega_m = 0.308 \pm 0.012$, with contributions from baryonic and CDM components of $\Omega_b h^2 = 0.02226 \pm 0.00023$ and $\Omega_c h^2 = 0.1186 \pm 0.0020$, respectively.

The final and most elusive component in the ΛCDM universe is dark energy, which exerts a negative pressure resulting in accelerated expansion at late times. In the standard model this takes the form of a cosmological constant Λ, which can be treated as a fluid with pressure $p_\Lambda = -\rho_\Lambda c^2$ and therefore has an equation of state parameter $w = -1$. The energy density of Λ therefore remains constant with spatial expansion, causing it to eventually become dominant over matter at $t \sim 10$ Gyr. The cosmological constant is consequently the largest component of the present day universe, with an estimated current density parameter $\Omega_\Lambda = 0.692 \pm 0.012$ based on observations by the Planck Collaboration et al. (2015). It is important to note that the observational data do not exclude more complex dark energy models, in which the equation of state can deviate from $w = -1$ and also potentially be time dependent. This dynamic dark energy can be parameterised in its simplest form by $w(a) = w_0 + (1-a)w_a$, where w_0 and w_a characterise the evolving equation of state. Modified gravity theories (a detailed discussion of which is given in section 1.6) also potentially provide an alternative explanation for accelerated expansion, without the need to include dark energy. However the currently available data are consistent with a universe containing time invariant dark energy described by the equation of state $w = -1.006 \pm 0.045$, which is in agreement with the inclusion of a cosmological constant in the ΛCDM model.

The rate of spatial expansion is governed by the standard model components described above, the physical properties of which are summarised in table 1.1. The density evolution of each individual component can be substituted into equation 1.8 to give the following expression:

$$H^2 = H_0^2(\Omega_r a^{-4} + \Omega_m a^{-3} + \Omega_\kappa a^{-2} + \Omega_\Lambda) \tag{1.14}$$

Component	Ω	w	$\rho(a)$	Domination era
Radiation	$\sim 10^{-4}$	1/3	$\propto a^{-4}$	$t \lesssim 50000$ yr
Baryonic matter	0.048	0	$\propto a^{-3}$	50000 yr $\lesssim t \lesssim$ 10 Gyr
Cold dark matter	0.258	0	$\propto a^{-3}$	50000 yr $\lesssim t \lesssim$ 10 Gyr
Dark energy (Λ)	0.692	-1	constant	$t \gtrsim 10$ Gyr

Table 1.1. Density parameters taken from Planck Collaboration et al. (2015)

where H_0 and Ω_κ are the present day values of the Hubble and curvature density parameters, respectively.

1.1.3 Cosmological redshift

In order to test the predictions of different cosmological models, a method is required with which to accurately measure how the universe has evolved up to the present day. The observed redshift of light emitted by distant galaxies can be used to infer their recession velocities, which when combined with distance information provides a probe of the expansion history. Cosmological redshift occurs as light travels through an expanding space, which causes an increase in its wavelength between the time of emission and observation. The light follows a null geodesic where $ds = 0$ and both θ and ϕ are constant, which simplifies the FLRW metric in equation 1.7 to yield the below relation:

$$r = c \int_{t_e}^{t_0} \frac{1}{a(t)} dt \tag{1.15}$$

where r is the comoving distance which the light has travelled from the time of emission t_e to its present observation at t_0. In the limiting case where $t_e \to 0$ the above expression gives the maximum separation at which events can be causally connected, known as the particle horizon. It can be seen from equation 1.15 that the wavelengths of emitted and observed light, λ_e and λ_0, can be related via the scale factor as follows:

$$\frac{\lambda_e}{a(t_e)} = \frac{\lambda_0}{a(t_0)} \tag{1.16}$$

assuming that the universe expands by an insignificant amount between the emission of two successive wave crests. Using the definition of redshift $z = (\lambda_0 - \lambda_e)/\lambda_e$ and the

present day scale factor $a_0 = 1$, the below expression can be derived:

$$a(z) = \frac{1}{1+z} \tag{1.17}$$

which relates the redshift z due to spatial expansion to the scale factor a when the light was emitted. This cosmological redshift provides a direct measure of the scale factor at t_e, and can therefore be used as an observational probe of how the universe has evolved over time.

The physical separation between distant galaxies and an observer increases with the expansion of space, causing these objects to recede with relative velocity $v = \dot{d}$. The relation between this recession velocity and the proper distance d of a galaxy at the current time, known as Hubble's Law, can be obtained from equation 1.2 as follows:

$$v = \frac{\dot{a}}{a} d = H_0 d \tag{1.18}$$

where H_0 is the present day value of the Hubble parameter, which is currently estimated as 67.8 ± 0.9 km s^{-1}Mpc^{-1} by the Planck Collaboration et al. (2015). The Hubble constant H_0 characterises the expansion rate at the present time, and is frequently expressed in the dimensionless form $h = H_0/100$ km s^{-1}Mpc^{-1}. For galaxies with $v \ll c$, the recession velocity is related to cosmological redshift via the linear expression $v \approx cz$. As such the observed redshift is approximately proportional to d for objects in the local universe, and is commonly used as a measure of distance in the cosmological context. It is important to note that galaxies may also experience motion relative to the comoving frame, known as peculiar velocity, in addition to the Hubble flow described by equation 1.18. Motion along the line of sight will produce a Doppler effect, which distorts the observed redshift and therefore apparent position of an object. For galaxies with large peculiar velocities, such as those in the vicinity of massive clusters, this can cause a significant deviation from Hubble's Law. However the dominant form of motion in the universe arises from spatial expansion, and therefore distance and redshift observations for a large number of objects can be combined to accurately measure H_0. Redshift surveys of distant galaxies provide an observational probe of the expansion history, which can be compared to theoretical predictions of cosmic evolution.

1.2 Expansion history

In the standard cosmological model, the universe originates from an initial singularity which begins to expand in an event known as the Big Bang. There are several theories as to the conditions which preceded the Big Bang, however these speculations are very difficult to test observationally. Also current knowledge of the expansion history is limited to events which occur after the Planck time $t_P \approx 5 \times 10^{-44}$s, as the physics required to describe timescales shorter than this does not yet exist. The measurements of galaxy recession velocities made by Hubble (1929) provided the first observational evidence for cosmic expansion, which implied that the universe would have been in a state of extreme density at some point in the past. However an alternative to the Big Bang theory which could also explain these observations was the Steady State model, first proposed by Hoyle (1948) and Bondi & Gold (1948). This described an expanding universe of infinite age, in which matter is continuously created to maintain a constant density. The Steady State model remained popular until the discovery of the Cosmic Microwave Background by Penzias & Wilson (1965), which was widely regarded as providing definitive evidence in favour of the Big Bang theory. Observational data confirms that the physical properties of the universe evolve over time, and its age is currently estimated to be 13.799 ± 0.038 Gyr based on results from the Planck Collaboration et al. (2015). The expansion history is comprised of several epochs during which different factors are dominant, as summarised in figure 1.2, which shows the main stages of cosmic evolution from the first moments after the Big Bang up to formation of structure observed at the present day.

In the very early stages of its evolution, the universe is thought to have undergone a period of rapidly accelerated expansion known as inflation. This epoch is believed to have begun around 10^{-34}s after the Big Bang, and lasted for only $\sim 10^{-33}$s before reverting to radiation dominated growth. During this brief inflationary phase the universe expanded exponentially, and consequently increased by at least a factor of 10^{26} in size. The accelerated growth is thought to be driven by a hypothetical scalar field, the inflaton, which exerts a negative pressure. A detailed discussion of this can be found in several review papers, such as Baumann & Peiris (2008) and Baumann (2009). The theory of inflation was first proposed by Guth (1981), and provided a single cosmological mechanism which resolved several fundamental issues with the Big Bang model. There were three main features which seemed inconsistent with observational evidence, known as the horizon,

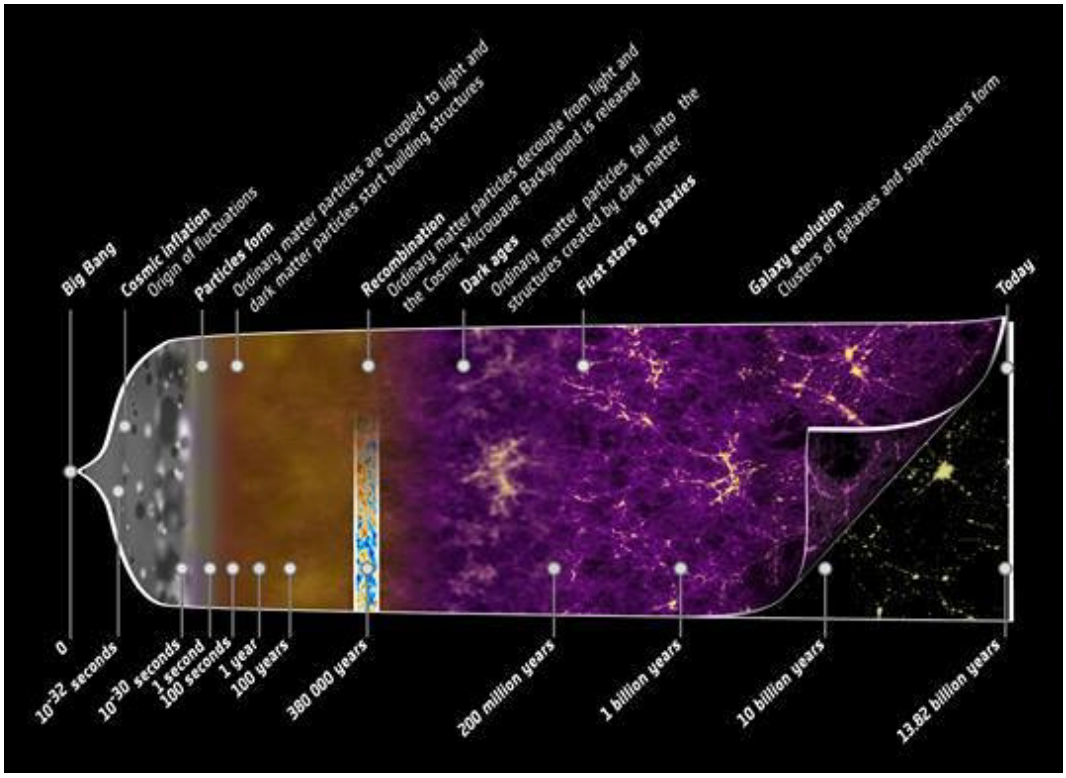

Figure 1.2. Illustrated timeline for the history of a ΛCDM universe, based on results from the WMAP survey. Image is credited to the NASA/WMAP Science Team.

flatness and monopole problems. The first of these concerns the homogeneous and isotropic nature of the universe on very large scales; measurements of the CMB show a remarkable uniformity in temperature across the sky, with fluctuations of less than one part in 10^5. However in the standard Big Bang theory (without inflation), regions with an angular separation of $\gtrsim 1^\circ$ are causally disconnected and therefore would not have been able to achieve thermal equilibrium. The observed isotropy of the CMB is difficult to explain using this model, and this is known as the horizon problem. The second conceptual puzzle with the standard Big Bang theory is the lack of spatial curvature measured at the present day, where $\Omega_\kappa \simeq 0$. Observations of the CMB show that the universe is nearly flat, and this requires very specific initial conditions in order to prevent curvature becoming dominant. Current measurements of Ω_κ imply that its value at the Planck time would have to be $\leqslant 10^{-60}$, and this extreme level of fine tuning is known as the flatness problem. Finally, there is an issue which arises from combining the standard Big Bang model with Grand Unified Theories (GUT), which describe the unification of the electromagnetic,

weak and strong nuclear forces at very high energies. It is predicted by GUT that the universe underwent a phase transition at $t \sim 10^{-36}$s, during which symmetry between the electroweak and strong nuclear forces was spontaneously broken. This phase transition is thought to have produced topological defects in the form of magnetic monopoles, which should be abundant in the present day universe. These objects have in fact never been observed, and this is known as the monopole problem.

The inclusion of an inflationary phase in the Big Bang model provides a solution to the issues described above, and also predicts how large scale structure can emerge from quantum fluctuations in the very early universe. During the period of exponential growth, the physical length scale of a fluctuation increases faster than the horizon distance d_H. Prior to inflation, the region of space containing the currently observable universe was much smaller than d_H, and therefore in causal contact. This allowed thermal equilibrium to be reached before the inflationary epoch began, thus resolving the horizon problem. A phase of accelerated expansion in the very early universe also provides a mechanism to smooth out spatial curvature, resulting in Ω_κ being driven very close to zero. Inflation therefore predicts that the universe should be nearly flat at the present day, without the need for fine tuning of the initial conditions. The observed absence of magnetic monopoles can also be explained by a period of exponential expansion, which would have greatly reduced their number density resulting in a negligible level of abundance today. After the inflationary phase the universe undergoes a process of reheating, during which energy associated with the inflaton field is released in the form of relativistic particles. This reheats the universe to its pre-inflation temperature, and ensures that the photon density vastly exceeds that of magnetic monopoles at the present day. In addition to solving the horizon, flatness and monopole problems, inflationary theory provides an explanation for the emergence of large scale structure observed today. During the period of accelerated expansion, quantum fluctuations in the inflaton field grew to macroscopic scales providing the seeds of structure formation. These density fluctuations are predicted to be strongly Gaussian in nature, which is in agreement with observations of anisotropy in the CMB. A wide range of models have been proposed which describe the physical mechanism behind inflation, a review of which can be found in Lyth & Riotto (1999). The measurement and characterisation of non-Gaussianity in primordial density fluctuations, see for example Maldacena (2003), provides a potential method with which to test these different models. Although the fundamental physics underlying this epoch is not yet fully understood, the

inflationary scenario is extremely consistent with observations and provides an elegant description of how large scale structure arose from quantum fluctuations in the very early universe.

1.3 Evidence for dark matter

In the standard cosmological model only a small fraction of matter in the universe is baryonic, with the majority consisting of cold dark matter. While this cannot be directly observed, its presence can be inferred due to its gravitational effect on visible matter. Theories which attempt to explain these effects using modifications to gravity, such as Modified Newtonian Dynamics (MOND), have been shown to be inconsistent with current observational evidence. The mass contribution from non-luminous baryonic matter, for example black holes, is significantly lower than that required to account for the effects of dark matter. This suggests a new type of particle which does not interact with the electromagnetic force, and therefore cannot emit (and absorb) light or undergo friction. There are several different forms of evidence which support the existence of dark matter, which provides a fundamental component of the standard cosmological model.

1.3.1 Galaxy dynamics

The first astronomer to make a strong case for the existence of dark matter was Fritz Zwicky in the 1930s, using observations of the Coma cluster. The radial velocity dispersion of galaxies in this cluster, which was measured by Zwicky (1937) to be around 1000 km s^{-1}, is much larger than that expected from the amount of visible matter. The first detailed evidence for dark matter was provided by Rubin & Ford (1970), who accurately measured the rotation curves of nearby galaxies. The radial dependence of orbital speed within a galaxy is directly related to its matter density profile, and the rotation curve arising from observed luminous matter is predicted to drop off with distance from the galactic centre. The discovery that stellar orbital velocities remain approximately constant with increasing radius, an example of which is shown in Fig. 1.3, provided the first compelling evidence for the existence of dark matter. The flat rotation curves observed in both our own and nearby galaxies, see for example Roberts & Whitehurst (1975) and Rubin et al. (1980), infer the presence of dark matter halos which extend beyond the visible galaxy boundary.

In addition to galactic rotation curves described above, detailed observations of galaxy

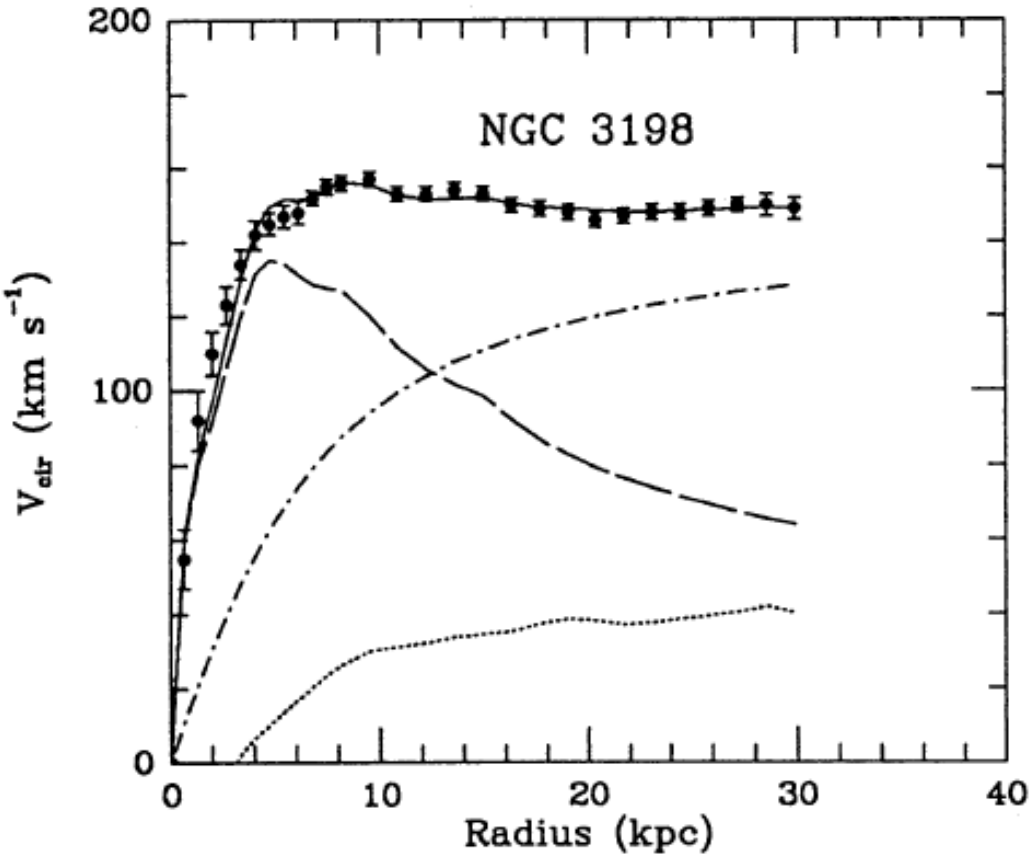

Figure 1.3. A galaxy rotation curve (Begeman et al. 1991).

motions within a cluster can also be used to accurately measure the underlying dark matter distribution. The mean streaming velocity of galaxies in the infall region around a cluster is dependent on the matter density profile and can be well described by linear theory on suitably large scales. The radial velocity dispersion of galaxies within a cluster also provides an observational probe of its mass, which can be predicted using the virial theorem. Measurements of galaxy virial motion have been used to estimate the masses of several different clusters, for example the Coma cluster, providing further observational evidence which indicates the presence of dark matter. The gravitational effect of dark matter on galaxy dynamics provides a fundamental probe of its underlying density distribution, and shows that it forms the majority of mass contained within the universe.

1.3.2 Gravitational lensing

The presence of dark matter not only has an effect on the motion of nearby luminous matter, but also on the path of photons in the form of gravitational lensing. Any large concentration of matter will act as a gravitational lens, which distorts and focuses light as predicted by General Relativity. This effect was first confirmed experimentally by Dyson et al. (1920), who observed the deflection of light due to the Sun's gravity during a total eclipse. Gravitational lensing can distort the images of distant objects in a number of ways, depending on both the lens mass and alignment with the background source. These effects range from multiple images of a single object and Einstein rings produced by strong gravitational lensing, to the more subtle image distortion resulting from weak lensing. Observations of gravitational lensing effects can be used to probe the lens mass distribution, and therefore provide an important method for detecting dark matter. The process of gravitational microlensing, where stellar size lenses amplify the light from background stars, can also be used to measure the abundance of massive astrophysical compact halo objects (MACHOs) within our galaxy. The observed population of MACHOs in the dark halo of our galaxy is found to be relatively small, implying that most of the matter content is smoothly distributed. This provides strong evidence that non-luminous baryonic matter does not contribute significantly to the mass of our galaxy, and a new type of particle is required to account for the gravitational effects of dark matter.

Clusters of galaxies can also act as large gravitational lenses, producing distortions which can be resolved in the images of background galaxies. Observations of gravitational shear, which results from both strong and weak lensing, provide an important method with which to measure the dark matter distribution in galaxy clusters. Weak lensing observations of the Bullet cluster by Clowe et al. (2006) were used to compare the distribution of its different mass components, as shown in Fig. 1.4, and provided some of the most compelling evidence to date for the existence of dark matter. Gravitational lensing provides a fundamental probe of the underlying mass distribution, and compliments galaxy dynamics as a method for determining the nature of dark matter.

1.3.3 Dark matter candidates

Although there is compelling evidence which supports the existence of dark matter, its physical nature is still currently unknown. The low abundance of non-luminous baryonic

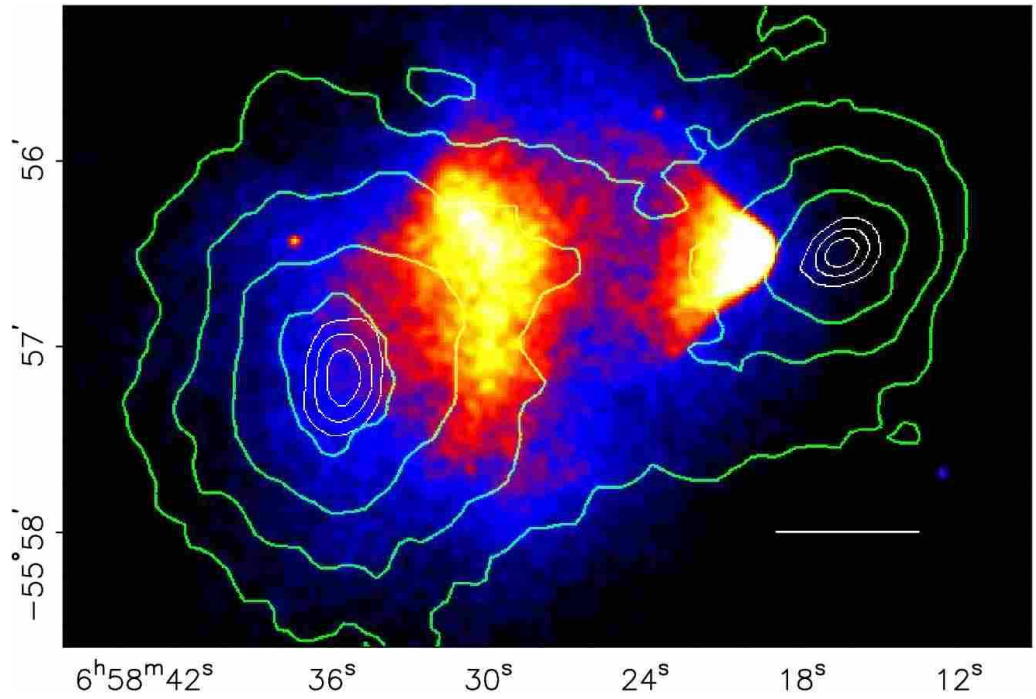

Figure 1.4. The bullet cluster (Clowe et al. 2006).

matter implies the presence of a new type of exotic material, which is not composed of quarks or leptons. Two different forms of this material have been postulated, known as hot and cold dark matter, the former of which consists of high-energy particles moving with relativistic velocities. In contrast, cold dark matter (CDM) is formed of weakly interacting non-relativistic particles, and current observational evidence strongly favours a CDM cosmological model. One non-baryonic particle known to exist is the neutrino, which has been shown to have a tiny but non-zero mass. These weakly interacting particles are thought to have decoupled from matter shortly after the Big Bang, forming the cosmic neutrino background. Although this has never been directly observed, the number density for each flavour (electron, muon and tau) of neutrino can be theoretically predicted in the standard cosmological model. Massive neutrinos provide a potential CDM candidate, however current constraints on their mass suggest it is too low to account for the effects of dark matter.

Another possible candidate for CDM are weakly interacting massive particles (WIMPs), although there is at present no direct evidence for their existence. This class of dark matter candidates includes several different hypothetical particles, with masses generally ranging

from 1 GeV up to around 1 TeV. Supersymmetry theory predicts that each elementary particle in the standard model has a partner, for example photinos and sneutrinos, which takes the form of a massive non-baryonic particle. The lightest of these supersymmetric particles is expected to be stable and interact only via gravity and the weak nuclear force, providing a potential candidate WIMP for dark matter. The Large Hadron Collider (LHC) is now running at sufficient energies to detect particles predicted by Supersymmetry theory, and should produce results on the validity of this model in the near future. In addition to WIMPs, other hypothetical objects such as primordial black holes, cosmic strings and axions have also been postulated as potential CDM candidates, however there is currently a lack of observational evidence for their existence. There are several different possible candidates at present for the composition of dark matter, and its direct detection remains one of the biggest challenges in particle physics.

1.4 Growth of structure

The complex large scale structure observed at the present day originated as minute matter overdensities, which arose from quantum fluctuations in the very early universe. These small scale overdensities became stretched out as the universe expanded and cooled, providing the seeds for structure formation. Matter is drawn towards the gravitational potential in an overdense region, causing it to grow increasingly dense over time. The rate at which overdensities grow is dependent on both the expansion and contents of the universe, and also the behaviour of gravity on cosmological scales. The observed galaxy distribution traces underlying structure in the dark matter, and can be used to obtain statistical measurements of growth. Observations of large scale structure therefore provide an important method for measuring the physical properties of the universe, and also probing the nature of gravity itself.

1.4.1 Density perturbation growth

The rate at which overdensities grow varies for different eras of the expansion history, depending on which component of the universe is dominant. During the radiation dominated era, the growth of density perturbations is suppressed below the horizon scale. At matter-radiation equality overdensities begin to grow, and the formation of structure occurs during the matter dominated epoch. This continues until late times when the

universe becomes dominated by dark energy, and subsequent growth is frozen out due to the accelerated expansion. The overdensity $\delta(\mathbf{x}, a)$ at a given position can be defined in relation to the mean background density $\bar{\rho}_m(a)$ as

$$\delta(\mathbf{x}, a) = \frac{\rho(\mathbf{x}, a) - \bar{\rho}_m(a)}{\bar{\rho}_m(a)} \tag{1.19}$$

where $\rho(\mathbf{x}, a)$ is the density at position $\mathbf{x}$. Although δ is a continuous field, it is often described in terms of discrete Fourier modes with a characteristic scale λ. The evolution of a primordial overdensity immediately after inflation can be described in terms of the growth factor $D(a)$ as

$$\delta(\mathbf{x}, a) = D(a)\delta_0(\mathbf{x}) \tag{1.20}$$

where $\delta_0(\mathbf{x})$ is the present day density contrast.

During the radiation dominated era, a density perturbation will initially undergo super-horizon growth at the rate $\delta \propto a^2$, while λ is greater than the expanding horizon scale d_H. The overdensity becomes causally connected when d_H reaches the scale λ, and subsequent gravitational collapse is then opposed by radiation pressure. The sub-horizon growth of density perturbations is therefore suppressed during the radiation dominated epoch, which causes acoustic oscillations to form in the baryon-photon fluid. These propagate at a high sound speed from overdense regions, which gives rise to anisotropies in the CMB and also baryon acoustic oscillations (BAO) that can be observed in the present day galaxy distribution. At matter-radiation equality the growth of density perturbations resumes, as the energy-density of matter becomes dominant over radiation. Overdense regions of pressureless CDM undergo gravitational collapse, producing the initial seeds for structure formation. During the matter dominated era, overdensities grow at a linear rate where $\delta \propto a$, allowing large scale structure to form over this epoch. Figure 1.5 shows the growth of δ during both radiation and matter domination, and its dependence on the scale factor. Density perturbations continue to grow linearly on cosmological scales, until late times when the expansion becomes dominated by dark energy.

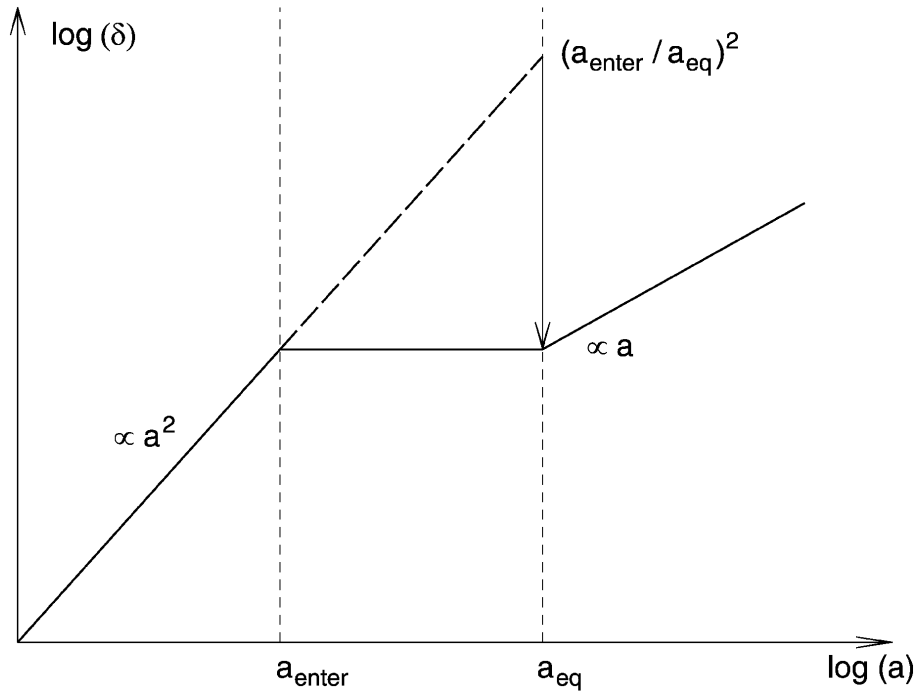

Figure 1.5. The growth of overdensities as a function of scale factor Schneider (2006).

1.4.2 Linear theory

On suitably large scales, the growth of overdensities during the matter dominated era can be accurately described using linear perturbation theory. In this model it is assumed that the universe contains only pressureless matter, which can be treated as a fluid with density $\rho(\mathbf{r}, t)$ and velocity field $\mathbf{v}(\mathbf{r}, t)$. The growth of density perturbations in linear theory is described using Newtonian gravity, and is therefore only valid on scales significantly smaller than the Hubble radius. For sufficiently low overdensities where $\delta \ll 1$, the fluid equations can be linearised to obtain an analytic solution which predicts their growth. The standard equations describing an ideal fluid are as follows:

$$\frac{\partial \rho}{\partial t} + \nabla \cdot (\rho \mathbf{v}) = 0 \tag{1.21}$$

$$\frac{\partial \mathbf{v}}{\partial t} + (\mathbf{v} \cdot \nabla)\mathbf{v} = -\frac{\nabla p}{\rho} - \nabla \Phi \tag{1.22}$$

where the pressure $p \equiv 0$ and Φ is the gravitational field, which satisfies the Poisson equation:

$$\nabla^2\Phi = 4\pi G\rho \tag{1.23}$$

The first of these expressions is known as the continuity equation, and describes the conservation of matter with diverging velocity field. The second is known as the Euler equation, which expresses fluid behaviour due to self-gravity and conservation of momentum. Assuming that $\delta \ll 1$, the ideal fluid equations can be combined to derive the following expression for linear growth:

$$\ddot{\delta} + 2H\dot{\delta} - 4\pi G\bar{\rho}_m\delta = 0 \tag{1.24}$$

where the middle term represents the effect of spatial expansion opposing gravitational collapse, which is described by the last term and dominates until late times. The fluid equations can also be used to derive an expression which describes peculiar velocity $\mathbf{v_{pec}}(\mathbf{x}, t)$ in the linear regime:

$$\dot{\delta} + \frac{1}{a}\nabla \cdot \mathbf{v_{pec}}(\mathbf{x}, t) = 0 \tag{1.25}$$

It is important to note that here, partial time derivatives of δ are taken at fixed comoving coordinate $\mathbf{x}$. A full derivation of the linear growth equations can be found in the literature, see for example Peebles (1980) and Schneider (2006). Linear theory provides a good description of density perturbations above a scale of ~ 10 Mpch^{-1}, even if they exhibit strongly nonlinear behaviour on smaller scales. As δ approaches unity the linear approximation begins to break down, and more complex models are required to describe subsequent growth. Linear perturbation theory provides a vital tool for describing the growth of overdensities, and formation of structure on a cosmological scale.

1.4.3 Peculiar velocity

In the linear regime, a direct relation between the peculiar velocity field and overdensity δ can be derived, which is valid at sufficiently large scales. In order to obtain an expression for the velocity field around a given density perturbation, the Fourier transform of equation

1.25 is taken to yield:

$$\frac{d\delta_k}{d\eta} + ikv_{pec}(k,\eta) = 0 \tag{1.26}$$

where the derivative of δ_k is taken with respect to the conformal time η. The density contrast scales as the growth factor D, which allows the continuity equation in Fourier space to be rewritten as follows:

$$v_{pec}(k,\eta) = \frac{i\delta_k}{kD}\frac{dD}{d\eta} \tag{1.27}$$

Substituting the relation $da = a^2 H d\eta$ into the above equation yields the following expression:

$$v_{pec}(k,\eta) = \frac{ifaH\delta_k}{k} \tag{1.28}$$

where the dimensionless linear growth rate f is defined as:

$$f \equiv \frac{a}{D}\frac{dD}{da} \tag{1.29}$$

Here $v_{pec}(k,\eta)$ represents the Fourier component of the peculiar velocity that is parallel to the wave vector $\mathbf{k}$, and therefore equation 1.28 can be written in its explicit form at low redshift as follows:

$$\mathbf{v_{pec}}(\mathbf{k}) = ifH_0\delta_k\frac{\mathbf{k}}{k^2} \tag{1.30}$$

The above expression provides a description of the velocity field in an overdense region, on suitably large scales where linear theory applies. The observed peculiar velocities of galaxies around a cluster can therefore be used as a measure of its overdensity, and consequently provide a direct probe of the surrounding gravitational potential.

1.4.4 Nonlinear growth

When an overdensity becomes sufficiently large the linear approximation is no longer valid, and an alternative approach is required to describe its growth. There are various different analytical methods for modelling nonlinear growth, which can be used to predict how structure forms on small scales. An important example is the Zel'dovich approximation,

which extrapolates the paths of matter particles from linear theory in order to predict nonlinear growth. The method presented by Zel'dovich (1970) describes the formation of flattened discs, filaments and ten points, and its predictions are confirmed by the structure observed in N-body simulations of dark matter. Another method for describing nonlinear growth is provided by the Spherical Collapse model, which was first proposed by Gunn & Gott (1972). This model assumes an Einstein de Sitter universe, and describes a density perturbation as an evolving sphere with uniform matter distribution. It is therefore required that the overdense region is spherically symmetric, and also has an average density which is significantly greater than that of the background universe. The Spherical Collapse model predicts how the perturbation boundary evolves with time, and provides a description of peculiar velocity in the limit of complete collapse. This applies in the case of sufficiently high overdensity, and is therefore only valid on scales smaller than a few $\mathrm{Mpc}h^{-1}$. The formation of dark matter halos and subhalos is predicted by the Spherical Collapse model, which is in agreement with the structure observed in N-body simulations.

During nonlinear growth, small deviations in spherical symmetry allow kinetic energy to be dissipated as random velocities, eventually resulting in a state of virial equilibrium. An overdensity stabilises at the virial radius when it reaches this state of equilibrium, halting further gravitational collapse. A density perturbation that has become virialized consists of a central halo bounded by the virial radius, which is surrounded by an infall region. The mean streaming of matter towards an overdensity is linear at sufficiently large scales, but undergoes a transition into nonlinear behaviour as it approaches the central halo. An accurate method for predicting the effects of nonlinear growth is therefore essential in order to fully describe the dynamics of matter within galaxy clusters.

1.4.5 N-body simulations

Although analytic models provide a good approximation for nonlinear growth, a more detailed description can be obtained by directly simulating the density field. A large number of dark matter particles can be simulated which trace the density field in a given comoving volume, and then subsequently allowed to evolve under self gravity. For each individual particle, the combined gravitational force which acts due to all other particles in the simulation is calculated. The resulting change in its position and velocity over a given timestep is then predicted using Newtonian dynamics, in order to obtain the new particle density distribution. This process is repeated for each timestep, and although

computationally expensive provides an effective method for describing nonlinear growth in the evolving density field.

In recent years several large N-body simulations have been developed, which describe the nonlinear growth of structure in various cosmological frameworks. Current examples of the largest simulations include the Dark Energy Universe Simulation (DEUS), Millennium-II and Millennium-XXL, descriptions of which can be found in Alimi et al. (2012), Prada et al. (2012) and Angulo et al. (2012*b*) respectively. The datasets produced by these simulations are extremely large, for example DEUS contains 550 billion particles in a volume the size of the observable universe. The N-body simulations described above employ methods such as standard Particle-Mesh (PM), where the fields are computed on a discrete grid, in order to improve computational efficiency. These dark matter simulations show the emergence of intricate structure where massive halos are separated by huge voids, and filaments connect overdense regions to form a large scale cosmic web. Figure 1.6 shows a visualisation of the present day matter density field from the Millennium-XXL simulations, illustrating the structure observed on different length scales.

N-body simulations can be used to predict the effects of nonlinear growth at different scales, and provide a detailed description of the underlying dark matter distribution. From observing the output of simulations it was found by Navarro et al. (1996) that dark matter halos have a characteristic density profile, which is dependent on their mass. This is known as a Navarro-Frenk-White (NFW) profile, and was obtained empirically by measuring the structure seen in N-body simulations. A sufficiently massive dark matter halo will also contain a galaxy population, the size of which is dependent on its mass. Consequently, baryonic effects such as feedback from active galactic nuclei (AGN), stars and supernova winds become significant on sub-halo scales, which has an impact on the growth of structure. High resolution hydrodynamical simulations, for example those described in Vogelsberger et al. (2014), can be used to predict small scale changes in overdensity due to baryonic effects. These simulations employ computational methods such as smoothed-particle hydrodynamics (SPH), in order to model complex processes like galaxy formation. Both baryonic and dark matter simulations provide an important tool for describing nonlinear growth, and also testing the predictions of analytic structure formation models.

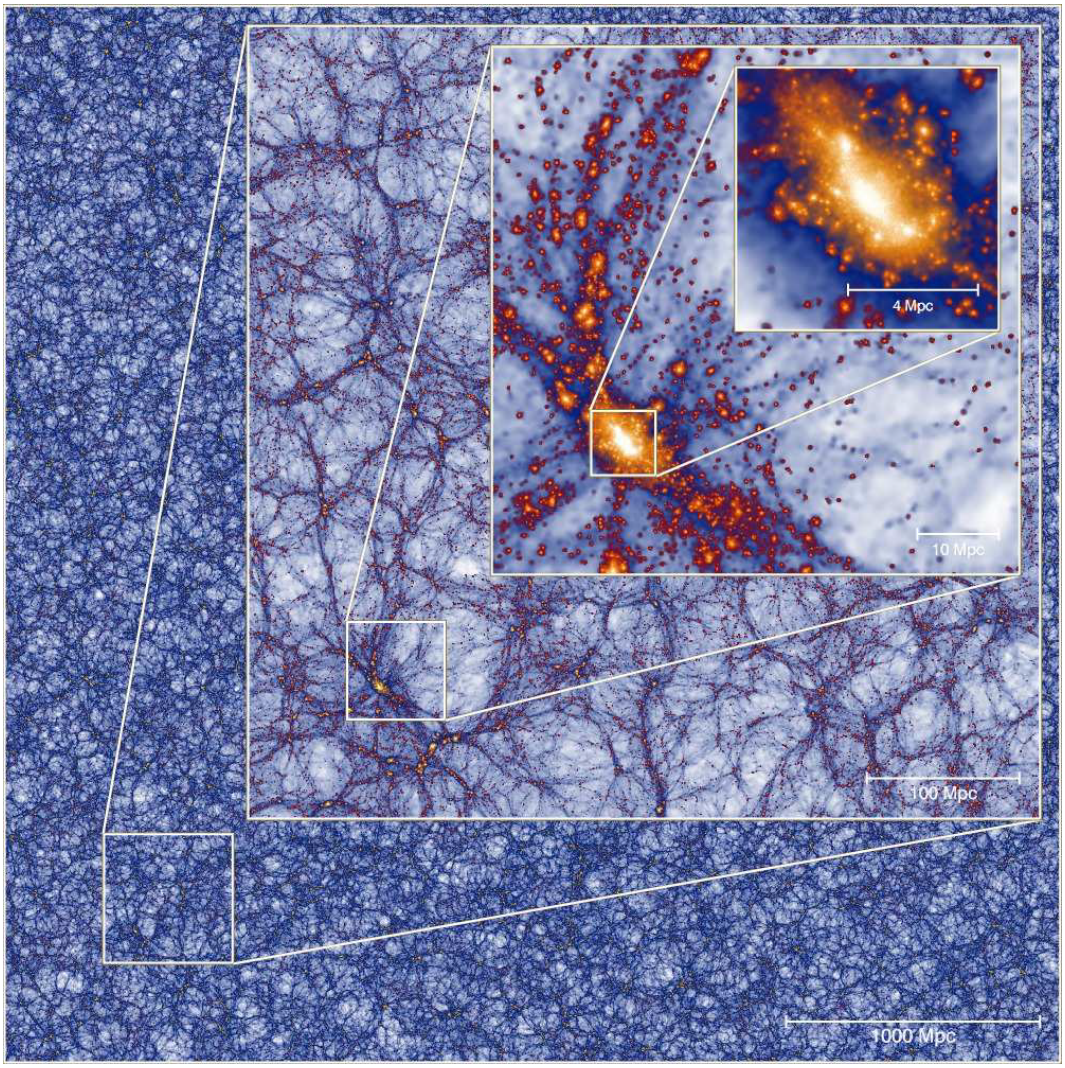

Figure 1.6. Illustration of an n-body simulation, from Angulo et al. (2012*a*).

1.4.6 Growth at late times

Density perturbations undergo linear growth during matter domination, however at late times their evolution becomes determined by the effects of dark energy. The universe enters an epoch of exponential expansion during the dark energy dominated era, where the scale factor grows as $a(t) \propto e^{\sqrt{\Omega_\Lambda} H_0 t}$. At late times the effect of spatial expansion on overdensities, known as Hubble drag, becomes dominant over their self gravity. During this epoch the mean background density drops exponentially, and the linear growth equation reduces to

$$\ddot{\delta} + 2H_\Lambda \dot{\delta} \approx 0 \tag{1.31}$$

where the Hubble parameter has a constant value of H_Λ. The above equation can be solved to obtain an expression for the overdensity as follows:

$$\delta(t) \approx C_1 + C_2 e^{-2H_\Lambda t} \tag{1.32}$$

where C_1 and C_2 are constants of integration. It is important to note that the above solution for δ is only valid in the linear approximation, and a numerical integration is required in order to include nonlinear effects. The growth of density perturbations becomes frozen out during the dark energy dominated era, as each point in the δ field is smoothed towards an asymptotic value by the expansion. At late times the average matter density falls as the universe expands exponentially, and growth of large scale structure effectively ceases during this epoch.

1.4.7 Statistical measures of structure

In order to compare the observed distribution of matter with predictions from cosmological models, a measure of its statistical properties is required. An important example is the two-point correlation function $\xi(r, a)$, which describes the clustering amplitude of matter at different scales. For two positions $\mathbf{x}$ and $\mathbf{y}$ which are separated by distance r, the matter correlation function can be defined as follows:

$$\langle \rho(\mathbf{x})\rho(\mathbf{y}) \rangle = \bar{\rho}_m^2 \left[1 + \xi(\mathbf{x}, \mathbf{y})\right] \tag{1.33}$$

where the angular brackets denote taking the average over all points. The dark matter correlation function can be predicted using linear theory, and describes how the clustering amplitude drops off with increasing scale. The inclusion of nonlinear effects increases the amplitude on small scales, and can be described analytically using methods such as the halo model. This predicts the clustering of matter both on sub-halo scales and the distribution of separate halos, known as the one and two-halo terms respectively. The nonlinear dark matter correlation function can also be determined empirically using results obtained from N-body simulations, as shown in figure 1.7. The correlation functions which describe the clustering of different objects, such as galaxies and halos, can be related to that of the dark matter via a quantity known as the bias factor. This characterises how these objects trace the underlying dark matter distribution, and can exhibit both time and scale

dependence. The matter correlation function can be expressed in many different forms, for example angular, projected and volume averaged. It can also be extended to produce general n-point correlation functions, which describe higher order clustering in the matter distribution. The matter correlation function evolves with the growth of structure, which increases the clustering amplitude at all scales over time.

Another important statistical measure of structure is provided by the power spectrum, which characterises the distribution of matter in Fourier space. This describes the amplitude of fluctuations at different length scales $L \simeq 2\pi/k$, where k is the wave number. The matter power spectrum $P(k, a)$ is related to the correlation function $\xi(r, a)$ via a three-dimensional Fourier transform as follows:

$$P(k) = 2\pi \int_0^\infty r^2 \frac{\sin kr}{kr} \xi(r) dr \tag{1.34}$$

where the integrals over angular coordinates are evaluated explicitly, as ξ is only dependent on the separation r. The initial power spectrum immediately after inflation can be predicted using scaling arguments, and is well described by a power law of index $n_s \simeq 1$ which is known as the Harrison-Zeldovich spectrum. During the radiation dominated era sub-horizon growth is suppressed, resulting in a peak in the present day power spectrum. The position of this peak is fixed at matter-radiation equality, after which the amplitude of fluctuations grows on all scales.

In linear theory, the present day power spectrum $P_0(k)$ can be described in terms of the transfer function $T(k)$, which is defined as:

$$P_0(k) = Ak^{n_s} T^2(k) \tag{1.35}$$

where A is a normalisation constant which can only be determined empirically from observations. The transfer function can be calculated for a particular cosmological model from the Boltzmann equations, and used to predict the present day linear power spectrum. On small scales nonlinear effects such as BAO and neutrinos become significant, producing additional features in the power spectrum. Corrections to $P(k)$ in the form of both analytic expressions and fitting formulae are therefore required to include nonlinear effects, which increase its amplitude at large k. Figure 1.8 shows a comparison between the linear and nonlinear power spectra for a ΛCDM universe at different redshifts, generated using the iCosmo code which is described in Refregier et al. (2011). The specified cosmological

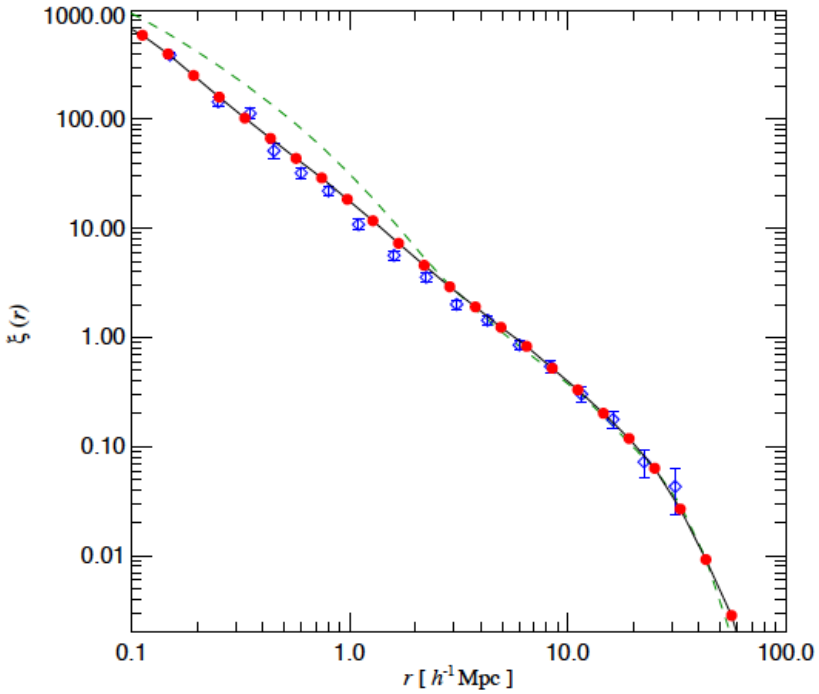

Figure 1.7. Present day galaxy correlation function measured from N-body simulations by Springel et al. (2005), compared to observational data from the 2dFGRS spectroscopic redshift survey. The two-point correlation function is shown for simulated galaxies (red symbols) and the survey data (blue diamonds), with results for the dark matter (dashed line) given for comparison.

parameters are consistent with observations by the Planck Collaboration et al. (2015), and the generated power spectra will be used for future calculations in this thesis.

1.5 Observational cosmology

A wide range of cosmological observables have been used to place constraints on the quantity and nature of the contents of the universe, and the properties of the expansion of the universe, described above. Here we summarise supernovae, which are commonly cited as the main evidence for the dominant component of the universe, dark energy. We then overview the primary cosmological observable: the cosmic microwave background. Finally we describe the two observables of most relevance to this thesis: gravitational lensing and velocities.

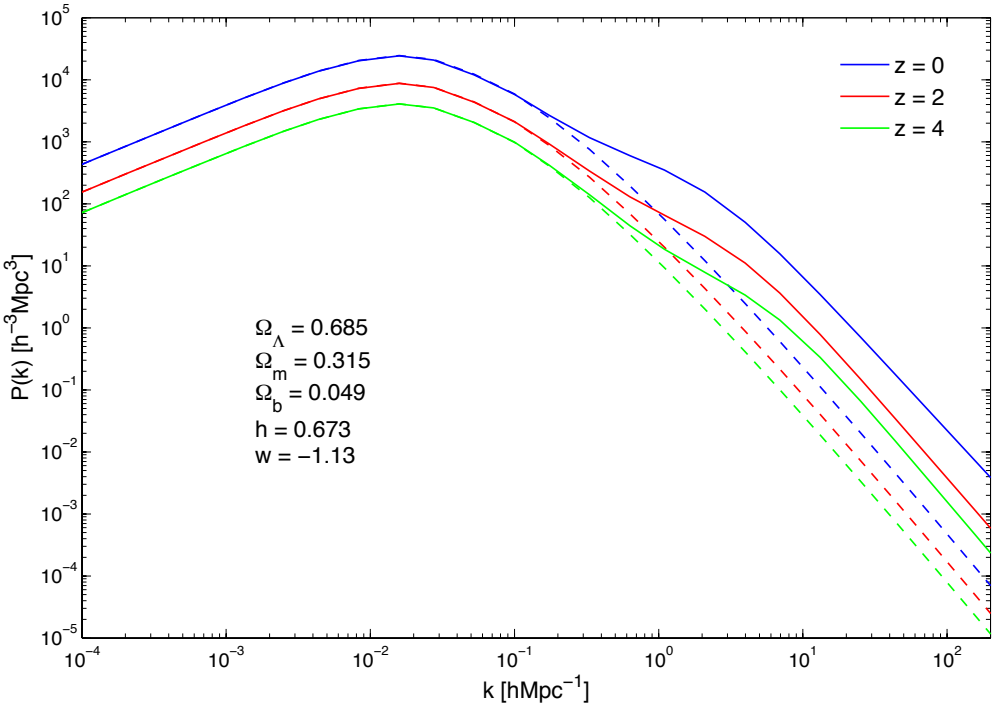

Figure 1.8. Predicted matter power spectra for a ΛCDM universe at three different redshifts, generated using the iCosmo code described in Refregier et al. (2011). Results are shown for both the linear (dashed lines) and nonlinear (solid lines) power spectra, which are predicted from the stated cosmological parameters.

1.5.1 Supernovae

The expansion of the Universe was first measured using the luminosities of galaxies, assuming these were standard candles (objects which all have the same luminosity). Later more sophisticated standard candles were developed, including Cepheids variable stars and Type 1a Supernovae. Because Type 1a supernovae are believed to occur when a white dwarf mass exceeds the Chandrasekhar mass, they are thought to be excellent standard candles. In practice all standard candles must be used with caution as they may depend on quantities that vary with the age of the universe, such as metalicity. Observations by Riess et al. (1998) and Perlmutter et al (1998) of type Ia supernovae led to the discovery that the expansion of the universe is accelerating. This discovery fitted well with the accumulating evidence from other datasets at the time from large scale structure and the cosmic microwave background (see below). The discovery of accelerated expansion is a highly unexpected result for a universe containing only matter, which should be decelerating. The current observed accelerated expansion led to the postulation of a mysterious

fluid called dark energy, which has a negative pressure. Current observations show that the properties of dark energy are consistent with a cosmological constant Λ, however its physical nature is unknown.

1.5.2 Cosmic Microwave Background

The Cosmic Microwave Background (CMB) radiation was formed when the Universe had expanded enough for the electrons and protons to combine (recombination) and thus the photons could travel freely towards us from that time (around 300, 000 years after the Big Bang). Just as we can see the bottom of a cloud when we look at the sky on a cloudy day, we can see the Universe at the time of recombination when we look into the sky. This is often referred to as the "last scattering surface".

Fluctuations in the CMB provides the tightest and most reliable constraints on cosmology. This has so far culminated in the Planck 2015 papers (Planck Collaboration et al. 2014*b*,*a*), with of order 100 precise measurements of the CMB power spectrum (see Fig. 1.10). The data points trace out the theoretical prediction almost perfectly, with the adjustment of only 7 cosmological parameters. The relatively well-understood physics of recombination predicts alternating peaks and troughs due to the collapse and expansion of primordial perturbations since the end of inflation. The largest scale peak, on the scale of about 1 degree, corresponds to the scale that has just had time to collapse to maxium density since inflation. The second largest peak (to the right on the angular power spectrum plot) corresponds to the scale that has collapsed and then expanded since inflation, and so on.

The angular position of the first peak therefore depends on the speed of collapse, the time between inflation and recombination, and the angular diameter distance to the last scattering surface. Crudely this measures the curvature of the Universe, which turns out to be very close to flat. The height of the first peak constrains the amount of non-baryonic dark matter - if the Universe were made only of baryons then it would be much higher. The overall shape of the angular power spectrum constrains the shape of the primordial power spectrum that seeded it.

The best fit parameters from the CMB are given in Table 1.1. These are widely considered the most reliable and tightest constraints on cosmological parameters today.

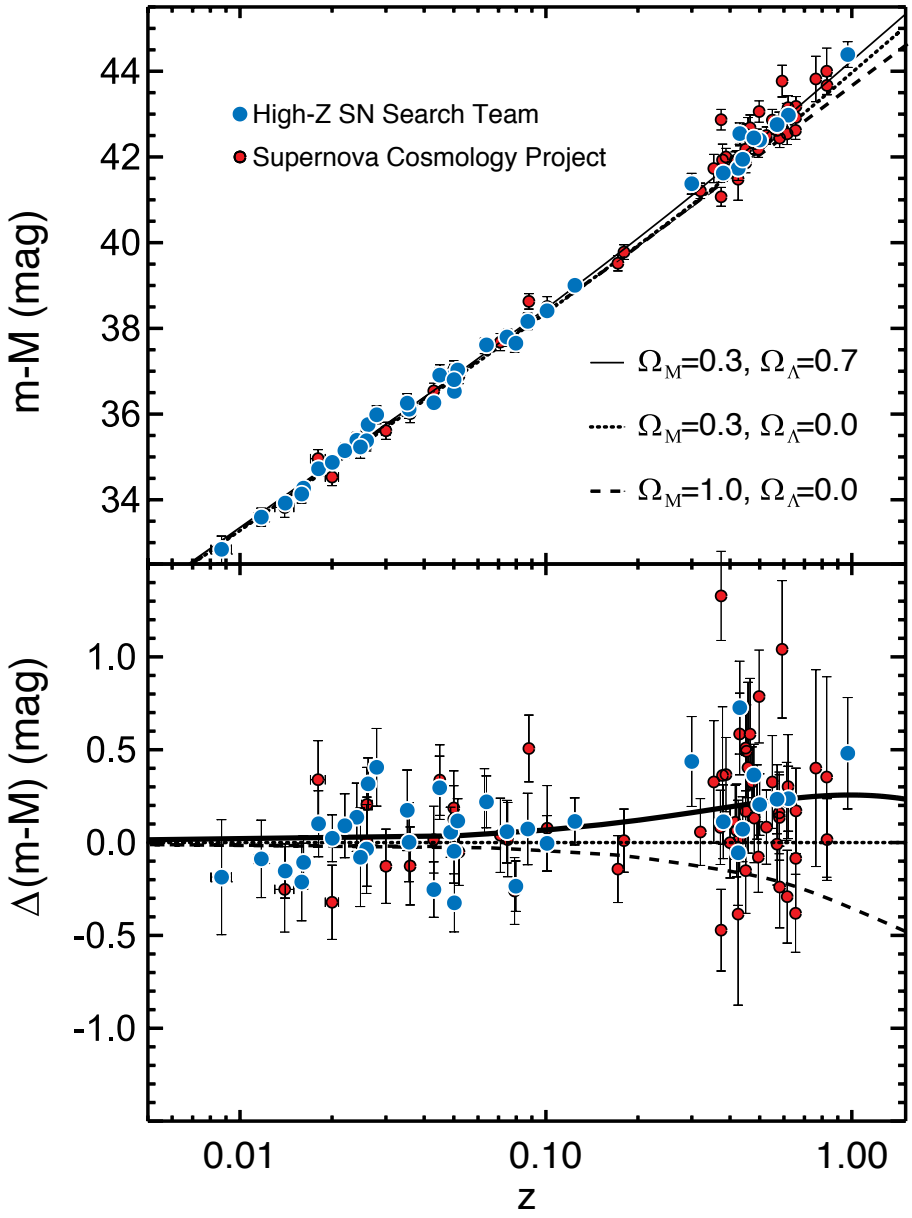

Figure 1.9. The first supernova observations indicating the presence of a cosmological constant. Copyright the High-Z Supernova Search Team.

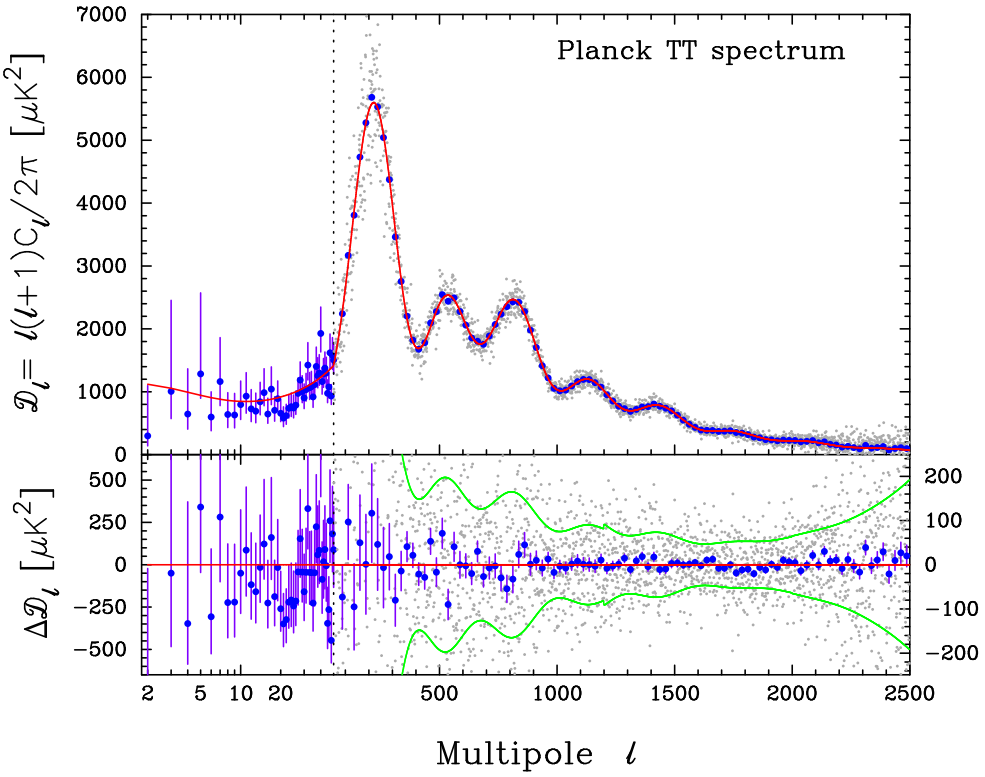

Figure 1.10. The CMB angular power spectrum, from Planck Collaboration et al. (2014*b*).

1.5.3 Gravitational lensing

As predicted by Einstein, when light passes a massive object, its path is distorted. and many measurements have been made since, most recently from the Deep Lens Survey (Jee et al. 2013), the Canada France Hawaii Telescope Lensing Survey (CFHTLenS, Heymans et al. 2012), the Dark Energy Survey (The Dark Energy Survey Collaboration et al. 2015) and the Kilo-Degree Survey (KiDS) (Kuijken et al. 2015; Hildebrandt et al. 2017).

1.5.4 Redshift space distortions

The clustering of galaxies viewed in redshift space appears distorted in relation to the shape in real space, due to a deviation of the galaxy velocities from pure Hubble flow as they fall into the gravitational potential wells. These peculiar velocities cause structures to seem squashed along the line of sight on linear scales, and this effect was first described by Kaiser in 1987. Using linear perturbation theory, Kaiser derived an expression for the galaxy power spectrum in redshift space $P_S(\vec{k})$ which relates it to the power spectrum in

real space $P_R(\vec{k})$ as follows:

$$P_S(\vec{k}) = P_R(\vec{k})(1 + \beta\mu^2)^2 \tag{1.36}$$

where μ is the cosine of the angle between the wave vector $\vec{k}$, and the line of sight. The parameter β is defined as $\beta = \frac{\Omega_m^{0.6}}{b}$, where Ω_m is the current matter density parameter and b is the bias which describes how galaxies trace the underlying dark matter density. It can be seen that in redshift space the matter power spectrum, unlike in real space, is anisotropic i.e. it has angular dependence. The correlation function in redshift space ξ_S can also be similarly related to its real space counterpart. Using these descriptions of both the power spectrum and correlation functions, the clustering of galaxies in redshift space is frequently used to constrain the cosmological parameters Ω_m and β. In this work, however, we use a numerical model of the cluster-galaxy redshift space correlation function in order to directly obtain the effective infall velocity profile for galaxies around a cluster. This infall velocity profile can then be used to calculate the gravitational potential in the region of that cluster.

The infall picture includes only those redshift space distortions which are due to galaxies infalling onto the cluster, and is therefore only accurate down to a certain scale. Towards the centre, where motions are virialized and highly non-linear, the large velocity dispersion means that the galaxy positions in redshift space are elongated in both directions along the line of sight, known as the 'fingers of God' effect.

1.6 Modified gravity

Arguably one of the most puzzling scientific discoveries made in recent times has been the revelation that the universe is currently undergoing an accelerated expansion. The first evidence of this was provided by observations of type Ia supernovae, which showed that their host galaxies appear to be moving away from us at an ever increasing rate. To explain this observed expansion, within the framework of General Relativity, requires a mysterious fluid referred to as dark energy, which exerts a negative pressure causing the expansion to accelerate. However, the unexplained nature of dark energy, which unlike dark matter does not have a theoretical basis in particle physics, has precipitated a wave of alternative theories in which General Relativity itself is altered in some way. These modified gravity theories, for example f(R) and DGP, account for the cosmic acceleration by changing the

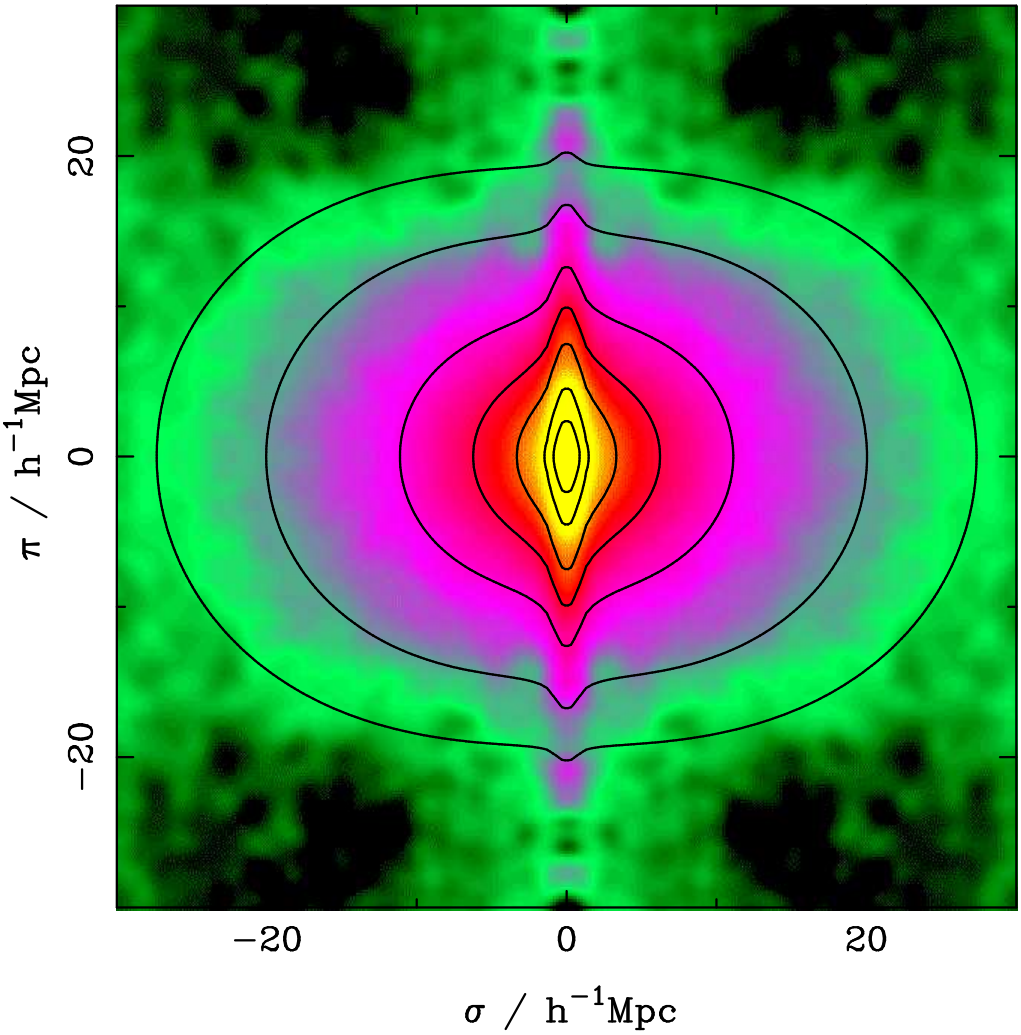

Figure 1.11. Infall and fingers of God as observed in the 2dFGRS (Peacock et al. 2001).

way gravity behaves at very large scales. As they are designed to produce the observed expansion history, these models can only be tested using perturbations in the background matter density. It is important to find a model independent way to differentiate between the dark energy and modified gravity scenarios, and the observational test of General Relativity described below is one such way of doing this which has been proposed in recent years.

In the Newtonian gauge, a scalar perturbation to the metric can be described as follows:

$$ds^2 = -(1+2\psi)dt^2 + (1-2\phi)a^2(t)d\vec{x}^2 \tag{1.37}$$

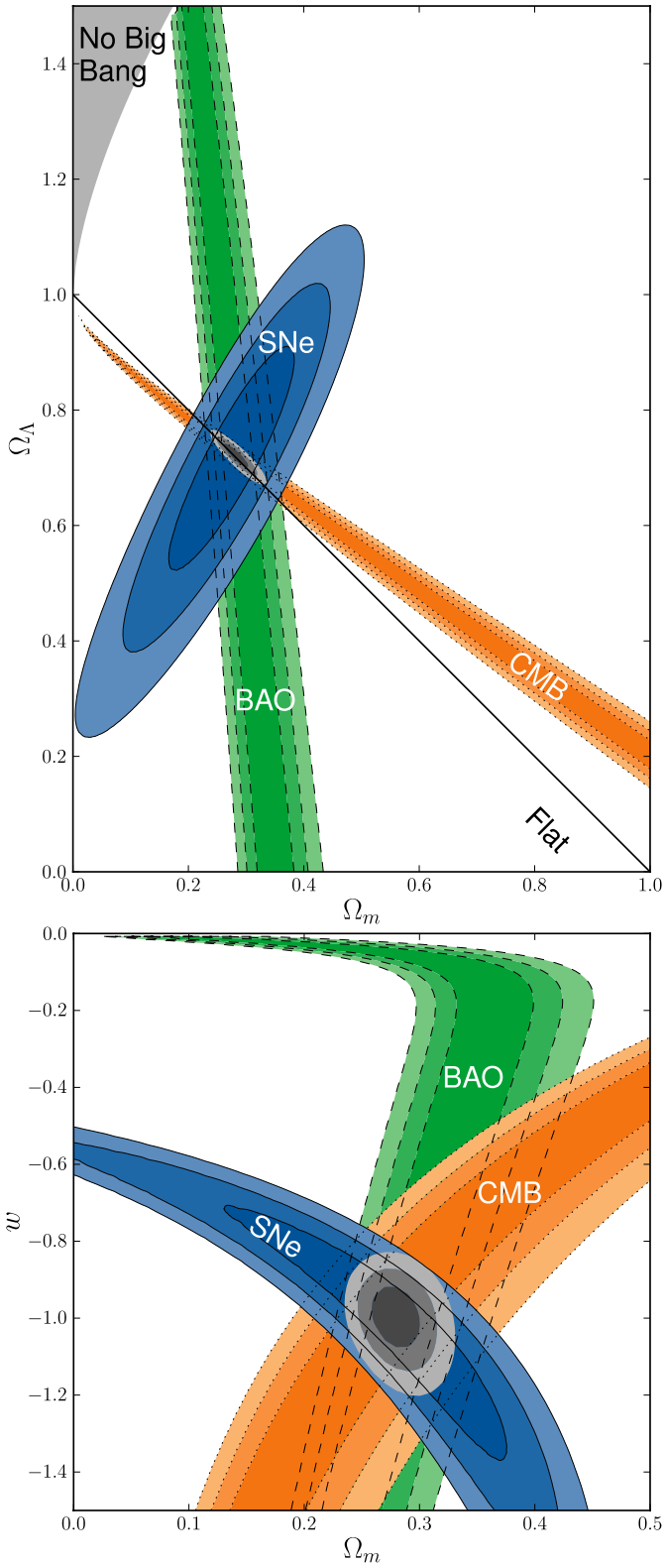

Figure 1.12. Constraints from type 1a supernovae taken from Suzuki et al. (2012).

where ψ and ϕ are scalar potentials which are equal in GR, in the absence of anisotropic stresses. Matter is sensitive only to the temporal potential ψ, also known as the Newtonian potential. Light however, which is traveling relativistically, is sensitive to both of the potentials ψ and ϕ. The dynamics of matter on large scales such as the clustering of galaxies around local overdensities can therefore be used as a probe of the Newtonian potential ψ, whereas the effect of these overdensities of matter on light, i.e. gravitational lensing, can be used to probe the sum of the potentials $\psi + \phi$. These two independent probes of the potentials can be combined to calculate the scale-dependent parameter η, defined as

$$\eta(k) = \frac{\phi}{\psi} \tag{1.38}$$

which in GR should be equal to unity. In modified gravity theories however, this quantity is expected to deviate from the GR case at very large scales.

1.7 Structure of this thesis

In Chapter 2 I summarise the n-body simulations used in this thesis and the halo catalogue that came with them. I then describe how I populated these simulations with galaxies used in the rest of the thesis. In typical observations data from many clusters must be combined to produce a statistically significant result. I also describe how the clusters were stacked in Chapter 2.

In Chapter 3 I develop a model for galaxy infall based on the linear regime on large scales and the spherical collapse model on small scales. I obtain a transition model based on simulations and provide a fitting formula.

In Chapter 4 I study the velocity dispersion of galaxies in the simulations and show that this varies as a function of distance to the cluster center, and that this is different in the directions parallel and perpendicular to the line-of-sight. I develop a model for this variation which is used in the following chapter.

Chapter 5 uses the tools developed in the preceeding chapters to make a full predicted redshift-space correlation function which is then compared with the simulations as a test of how the cluster mass may be constrained from this observable.

Finally the thesis ends with some concluding remarks in Chapter 6.

This page was intentionally left blank

Chapter 2

Population of N-body Simulations via the Halo Model

The various models required to provide a full description of redshift space distortions in the galaxy distribution around clusters will be discussed in the following chapters, and in this work data from N-body simulations of dark matter will be used for the purposes of both development and testing of these models. However in order to make a comparison with the predictions which relate to the dynamics of galaxies, these simulations which describe the evolution of the DM density field need to first be populated. The approach taken here is based on the halo model, which uses a localised description of how galaxies trace the underlying density via a statistic known as the halo occupation distribution (HOD). This gives a relation between the mass of a DM halo and the number of galaxies it's expected to contain, and provides a useful method with which to populate the halos in order to obtain a realistic prediction for the galaxy distribution at a given redshift. In this chapter the N-body simulations that will be referred to throughout this work are described, and an HOD used to populate the halos with galaxies so that mock observations can be generated and then compared to the model predictions for different aspects of galaxy dynamics in clusters on quasi-linear scales.

2.1 The simulations

The N-body data which will be used here are taken from GADGET-2 simulations, a full description of which is given in Heitmann et al. (2010). In these simulations a particle-mesh (PM) algorithm is combined with a tree-PM approach to model the evolution of 1024^3 DM particles under gravity, in a comoving volume of $(936\ \mathrm{Mpc}h^{-1})^3$. The DM particle mass is $5.3 \times 10^{10}\ \mathrm{M}_{solar}h^{-1}$, with an inter-particle spacing of approximately $1\ \mathrm{Mpc}h^{-1}$. These methods effectively sample the phase space distribution, solving the equations of motion for the resulting set of tracer particles to provide a description of the evolving DM density field. The data which will be populated with galaxies consists of a single realisation of a ΛCDM universe at redshift 0.67, with the following cosmological parameters: $\Omega_m = 0.25$ and $\Omega_\Lambda = 0.75$ for the contributions from the total matter content and cosmological constant respectively, a baryon density given by $\Omega_b = 0.024h^{-2}$, a dimensionless Hubble constant of $h = 0.72$, the normalisation set by $\sigma_8 = 0.8$ and a spectral index fixed at $n_s = 0.97$. These parameters correspond to the five-year Wilkinson Microwave Anisotropy Probe (WMAP) observations, which are described in Dunkley et al. (2009).

The raw data takes the form of several unformatted GADGET files containing a list of DM particle positions and velocities, which must first be processed in order to populate the simulations with galaxies. A halo catalogue is also provided which describes the virial masses and locations of DM halos in the simulations, in addition to their concentration parameters and the most gravitationally bound particle. This halo catalogue will be used in combination with the raw data in order to assign the DM particles to their parent halos, so that the number of galaxies predicted by the HOD for a given halo can be selected at random from these particles. This will provide a galaxy catalogue corresponding to a luminosity threshold determined by the HOD parameters used, which can be used to generate mock data with which to compare predictions from the various models presented here.

2.2 The halo catalogue

The halo catalogue which is provided with the simulations uses a friends-of-friends (FOF) method to define DM halos within the simulations (please see Heitmann et al. (2010) for more details), and contains a list of the resulting halos found which includes both the FOF and virial mass, position, concentration parameter and most bound particle for

each halo. The friends-of-friends method selects particles separated by less than a given linking length from their nearest neighbour, grouping these particles together to define a DM halo. The linking length used here is 0.168 Mpch^{-1}, and the resulting halo catalogue has a mass range of approximately 10^{11} to 10^{15} M$_{solar}h^{-1}$. It is important to note here that the virial mass given in the halo catalogue is calculated relative to the comoving critical density, and this needs to be taken into account in cases where predictions assume a different definition taken relative to the mean background density. In developing the models which are introduced in the following chapters, we need an accurate method with which to predict the mean density for halos of a specified mass. For this purpose the halo mass function presented in Sheth & Tormen (1999) is used, which gives an expression for the mean density $\bar{\rho}_h$ for halos of virial mass M_h as follows:

$$\bar{\rho}_h(M_h) = \frac{A\bar{\rho}_m}{M_h^2}\left(1 + \frac{1}{(a\nu^2}^p\right)\sqrt{\frac{a\nu^2}{2\pi}}\exp\left(\frac{-a\nu^2}{2}\right)\frac{d\ln\nu^2}{d\ln M_h} \tag{2.1}$$

where $\bar{\rho}_m$ is the comoving mean background density, $A = 0.322$, $a = 0.707$, $p = 0.3$ and $\nu = \delta_c/\sigma(M_h)$ with $\delta_c \approx 1.686$ and $\sigma^2(M_h)$ describes the variance in the initial density field in spheres with the same virial radius R_{200} corresponding to the given halo mass. It is important to emphasise that the virial mass in the above expression is calculated relative to the mean background density $\bar{\rho}_m$ and therefore the equivalent masses need to be calculated from those given in the halo catalogue, which are defined relative to the critical density, in order to make a direct comparison with the halo mass function observed in the simulations.

Figure 2.1 shows the mean density of halos as a function of virial mass predicted by equation 2.1, compared to that observed in the simulations. These results are obtained by measuring the total count from the halo catalogue for a given mass bin, and dividing this by the simulation volume. It can be seen that the predicted mean halo density shows good agreement with that observed in the simulations, except for at very low virial masses which are approaching the DM particle mass in the simulations of $\sim 5 \times 10^{10}$ M$_{solar}h^{-1}$ and therefore not included in the halo catalogue. However, in the mass range of interest, the halo mass function provided by Sheth & Tormen (1999) can be considered sufficiently accurate for the purposes here.

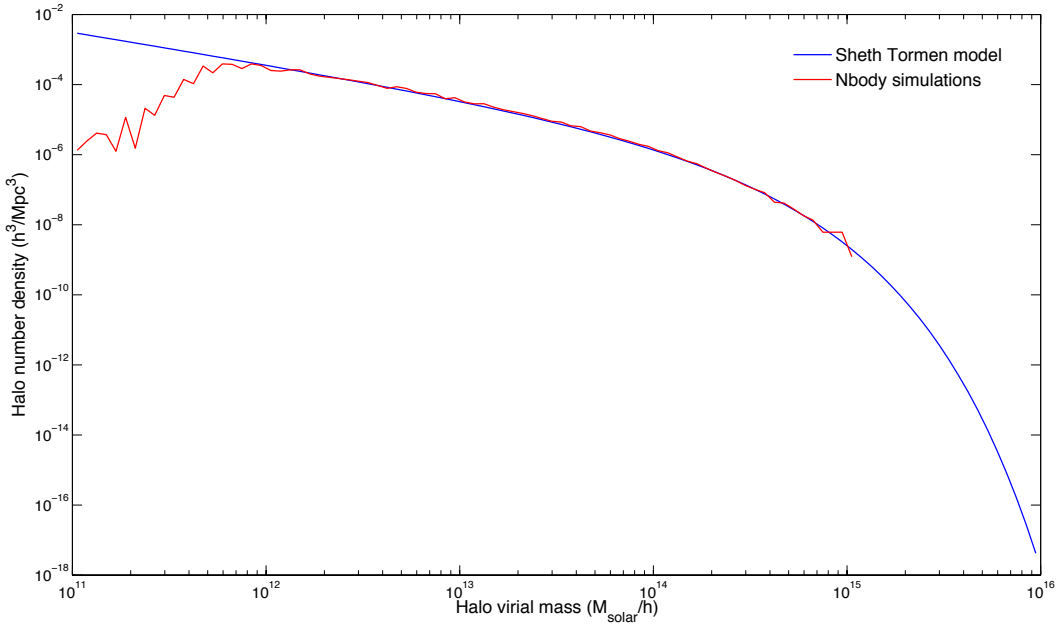

Figure 2.1. Mean halo number density as a function of virial mass as predicted by the halo mass function (blue line), compared to results observed in the simulations (red line) for a wide range of different halo mass bins.

2.3 Populating the simulations

In order to populate the halos given in the catalogue described above, a halo occupation distribution is required to predicted the expected number of galaxies in a halo of given mass. The HOD used here is described in Zehavi et al. (2011) and gives the following relation for the expected galaxy population $\langle N_{\rm gal}(M_h)\rangle$ within a halo with virial mass M_h:

$$\langle N_{\rm gal}(M_h)\rangle = \frac{1}{2}\left[1+\mathrm{erf}\left(\frac{\log M_h - \log M_{min}}{\sigma_{\log M}}\right)\right]\left[1+\left(\frac{M_h - M_0}{M_1'}\right)^{\alpha}\right] \tag{2.2}$$

where the parameters M_{min}, $\sigma_{\log M}$, M_0, M_1' and α depend on the luminosity threshold to which the galaxy populations correspond to. The first term in equation 3.25 represents the mean occupation function for central galaxies, characterised by a minimum mass scale M_{min} with width $\sigma_{\log M}$. The second term describes the satellite galaxy mean occupation function, which has a cutoff mass scale M_0 with normalisation M_1'. The high mass slope α characterises the increase in $N_{\rm gal}$ with halo mass, in the case where multiple satellite galaxies are expected. The predicted number of galaxies as a function of halo virial mass calculated from equation 3.25 is shown in figure 2.2 for a variety of different absolute

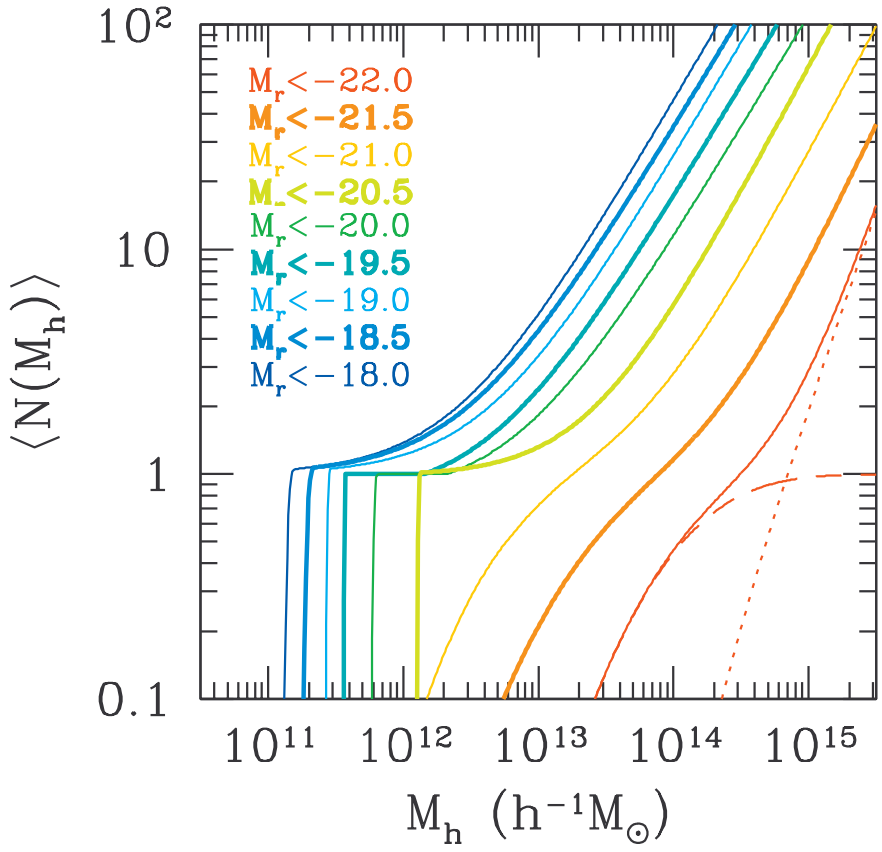

Figure 2.2. Expected galaxy population as a function of parent halo mass, for a range of different luminosity thresholds. This figure is adapted from Zehavi et al. (2011).

magnitude thresholds, each of which is described by a specified set of HOD parameters. This can be used to populate halos in the simulations with galaxies which correspond to a given maximum luminosity, and therefore produce mock observations which emulate a particular redshift survey. It can be seen from figure 2.2 that there is a kick down in the halo occupation distribution corresponding to luminosity thresholds of $M_r < -20.5$ and below, as there is a minimum halo mass required in order for it to contain a central galaxy. For luminosity thresholds of $M_r < -21$ and above only the more massive halos are expected to contain any galaxies, and the HOD is therefore dominated by the high mass slope parameter α resulting in a smooth shape.

The HOD parameter values used here are $\log M_{min} = 12.11$, $\sigma_{\log M} = 0.01$, $\log M_0 = 11.86$, $\log M_1' = 13.41$ and $\alpha = 1.13$, which corresponds to a galaxy luminosity threshold of absolute magnitude -20.5. At the simulation redshift of 0.67 this provides mock observations equivalent to a survey with an apparent magnitude limit of 22.5, similar for example

to the Dark Energy Survey (DES) first year observations. The distribution of $N_{\rm gal}$ about the mean for a given halo mass is assumed to be Poissonian, and the galaxy positions and velocities are obtained by selecting dark matter particles at random from the parent halo. It is important to note that the most gravitationally bound particle is always selected as the central galaxy, and then satellite galaxies subsequently selected randomly from the remaining DM particles associated with the given halo. The process of populating the simulations, for a given set of HOD parameters, using the provided GADGET data and halo catalogue is summarised in the flow chart shown in figure 2.3.

Figure 2.4 shows the overdensity given by $\delta = (\rho - \bar{\rho})/\bar{\rho}$ measured in a slice through the simulations at $x = 400$ Mpch^{-1} for both the dark matter, and the galaxies after the halos have been populated. It can be seen that the DM distribution is significantly smoother that that of the galaxies, which show regions of tight clustering and also empty voids.

Note that HOD modelling differs from semi-analytic modelling because it considers just the final positions of the dark matter particles, whereas semi-analytic modelling considers the complete halo merger tree when populating with galaxies. Baryons should ideally be included in the simulations because they allow cooling in the centres of halos allowing a steeper profile, but also can puff up the halos due to feedback processes. These all have an impact at the smaller scales which overlap to some extent with those considered in this thesis and therefore should be considered in future work.

2.4 Stacking clusters

In order to compare observations of galaxy dynamics around clusters from the simulations with theoretical predictions, a measure of their statistical properties is required. This is achieved by stacking large numbers of clusters with a given primary halo mass, to obtain a combined dataset of their surrounding galaxies. The process of stacking clusters allows the accurate measurement of their statistical properties, such as the cluster-galaxy correlation function. It also provides a method with which to calculate the effective galaxy infall velocity profile for a cluster of a given mass, which can then be compared to the predictions from different models. In order to obtain a stacked dataset from the N-body simulations, all halos which fall within the specified cluster mass bin are firstly selected from the catalogue. It is important to note that the virial mass used when selecting halos is calculated relative to the mean background density, as this is the definition used in

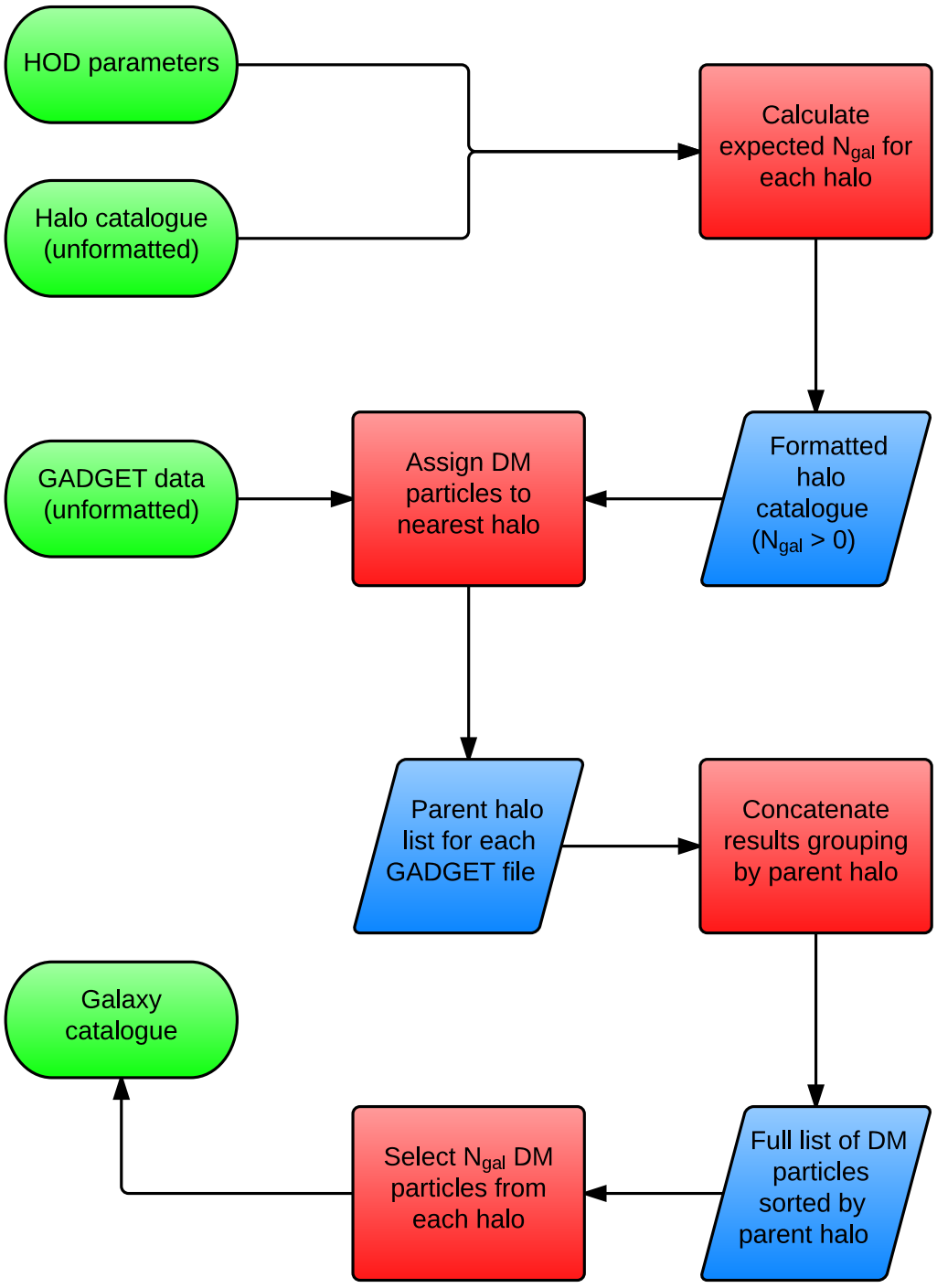

Figure 2.3. Flow chart illustrating the method used to populate the simulations with galaxies, for a given set of HOD parameters. The main inputs and output are indicated in green, and red boxes describe each stage of the process with intermediate inputs and outputs for the model shown in blue.

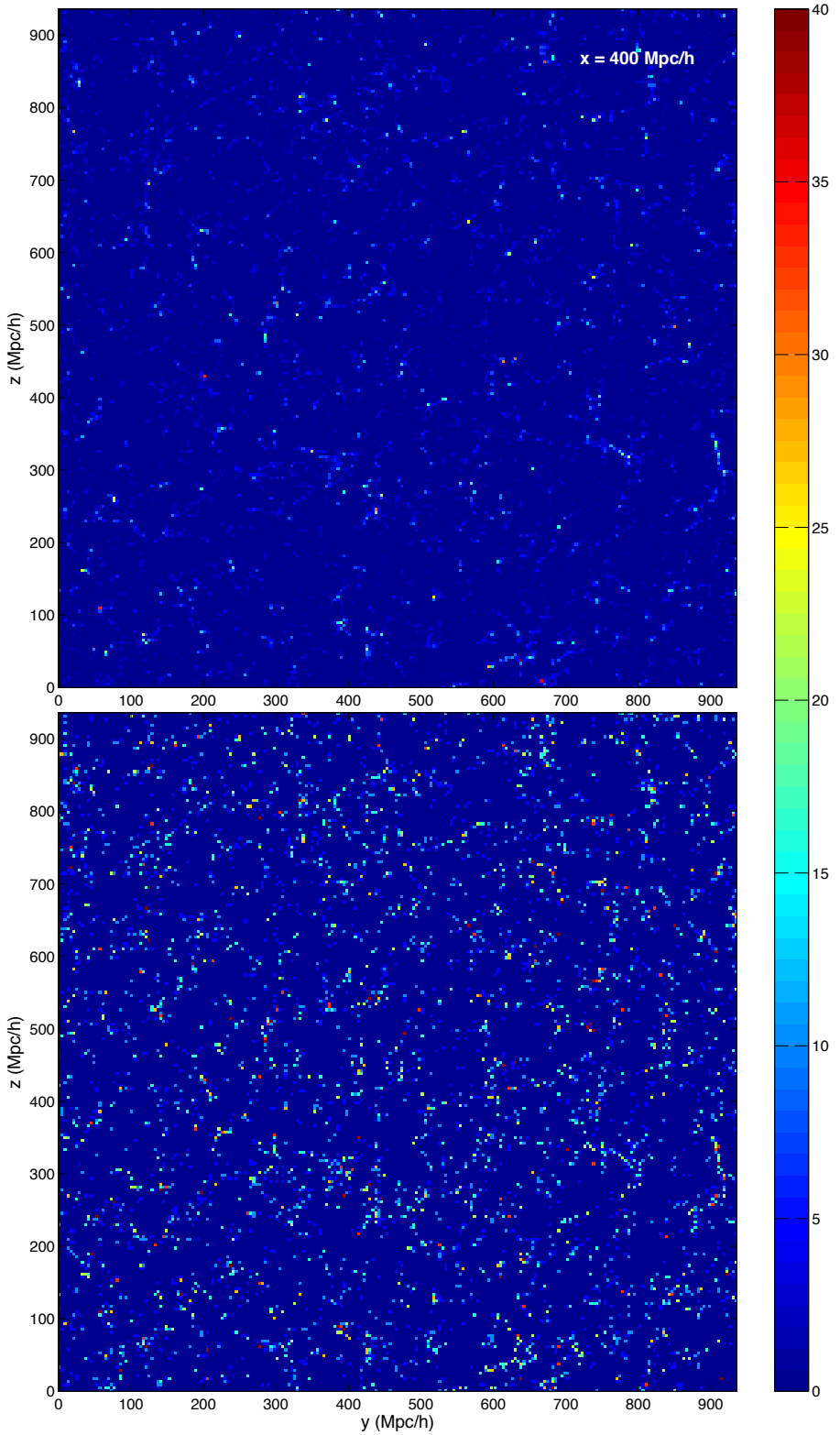

Figure 2.4. Overdensity field for the dark matter (top) and galaxies (bottom) in the populated N-body simulations, measured in a slice trough the comoving volume at $x = 400$ Mpch^{-1}. The colour bar represents the overdensity δ for the dark matter and galaxies.

the subsequent theoretical relations. Velocities are then obtained for the stacked halos by calculating the average motion of their associated galaxy populations. For each individual halo the set of galaxies which reside in a radius of 100 Mpch^{-1} are then selected from the catalogue. The galaxy positions and velocities relative to the primary halo are calculated in each case, and then combined to produce one large dataset for the specified cluster mass bin.

The above method was used to generate stacked cluster datasets from the N-body simulations, selecting halos and galaxies from the catalogues described in previous sections. Clusters were stacked for four different primary halo mass bins, the properties of which are summarised in table 2.1. It can be seen that the datasets for more massive clusters require a significantly wider mass bin, in order to include an adequate number of stacked halos for statistical accuracy. This is due to the low abundance of very massive clusters in the simulations, as predicted by the halo mass function. It is important to note that the use of a wider halo mass bin results in a greater deviation between its central and average values, as shown in table 2.1. This needs to be taken into account when comparing with theoretical predictions.

The stacked datasets were used to calculate the average galaxy number density around the clusters in both real and redshift space, for the four different primary halo mass bins described above. The galaxy distribution in redshift space was obtained by shifting their positions in the z direction, taken as the line of sight, by the amount $\Delta z = v_z/H_0$ where v_z is the line-of-sight velocity relative to the primary halo. Figure 2.5 shows the observed galaxy number density from the simulations as a function of position relative to the cluster centre, for the halo mass bins summarised in table 2.1. Results are compared for both real and redshift space, and clearly show the line-of-sight distortions which arise due to galaxy infall. The Fingers of God effect resulting from high galaxy velocity dispersion within the primary halo can also be seen, and becomes more prominent with increasing cluster mass. Figure 2.5 also shows a greater level of noise in the average density distribution around more massive primary halos, which have datasets with a much smaller number of stacked clusters due to their low abundance in the simulations.

In subsequent chapters of this thesis, models will be introduced which describe the dynamics of both halos and galaxies observed in stacked cluster from the simulations. In each dataset the positions and velocities are taken relative to the primary halo, which has mass $M_{\rm ph}$ defined as the average of the specified primary halo mass bin. This is

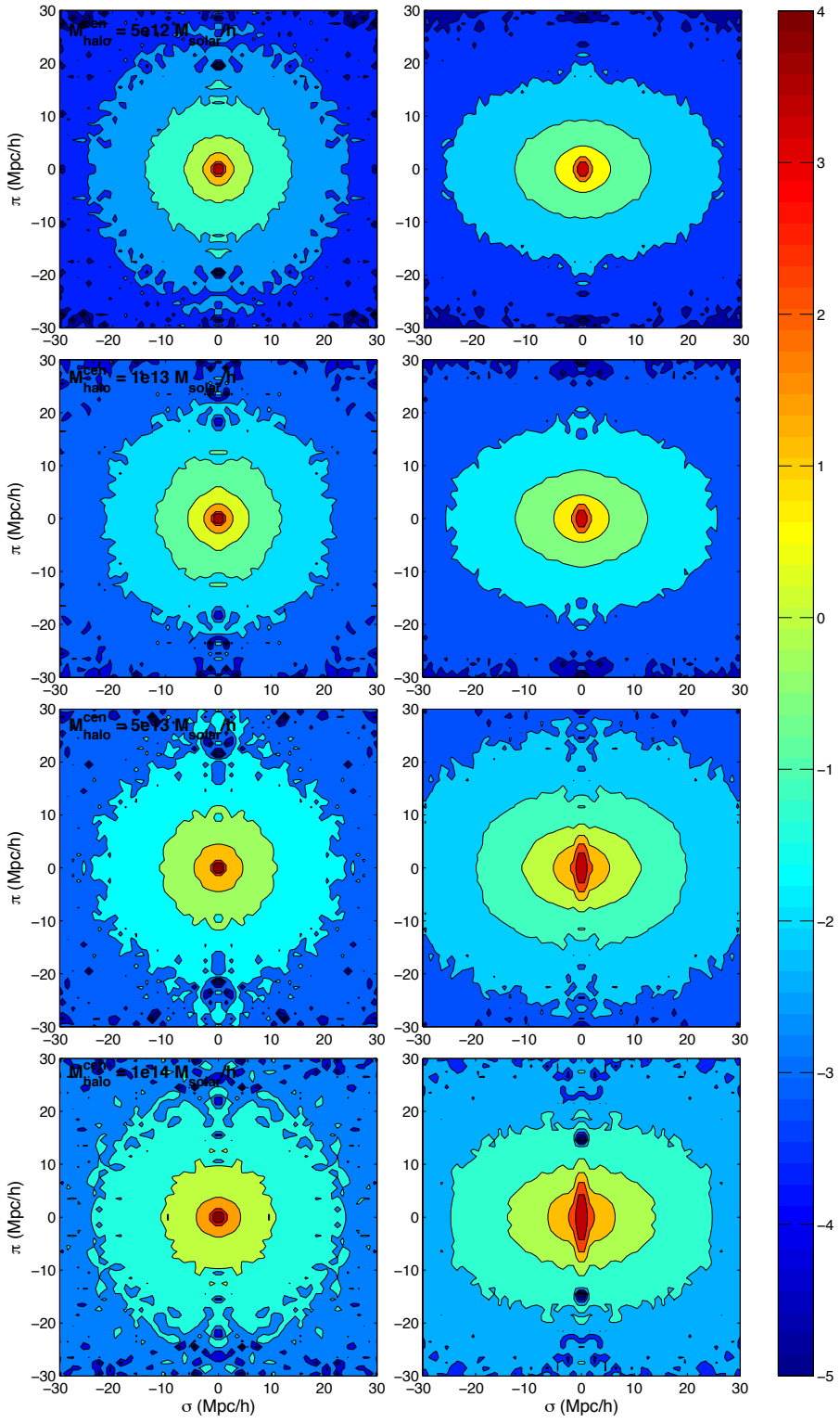

Figure 2.5. Galaxy number density in real (left panels) and redshift (right panels) space for stacked clusters in the simulations, as a function of position relative to the primary halo. Results are shown for four different cluster mass bins, centred on (from top to bottom) 5×10^{12}, 1×10^{13}, 5×10^{13} and 1×10^{14} $\mathrm{M}_{solar}h^{-1}$. The colour bar represents a logarithmic scale of the galaxy number density in units of $\mathrm{Mpc}^{-3}h^3$, and the figure labels $\pi = r_\pi$, $\sigma = r_\sigma$ and $M^{\mathrm{cen}}_{\mathrm{halo}} = M_{\mathrm{ph}}$.

$M_{\rm ph}$	Bin width	Average $M_{\rm ph}$	N_{clus}	$N_{gal}^{tot}(r_{max})$
5.00×10^{12}	2.50×10^{11}	5.01×10^{12}	10985	1.28×10^{8}
1.00×10^{13}	1.00×10^{12}	9.97×10^{12}	10119	1.19×10^{8}
5.00×10^{13}	1.00×10^{13}	4.98×10^{13}	3008	3.55×10^{7}
1.00×10^{14}	2.00×10^{13}	9.92×10^{13}	1018	1.21×10^{7}

Table 2.1. Properties of stacked clusters from the simulations with four different primary halo mass bins, used to measure the mean galaxy number density relative to the cluster centre in both real and redshift space. The halo mass bin centres, widths and average values are stated in each case, all given in units of $\mathrm{M}_{solar}h^{-1}$. The number of halos stacked is also shown, and the total count of galaxies which reside within a distance of 100 Mpch^{-1} from the cluster centre.

surrounded by secondary halos of different masses $M_{\rm sh}$, which covers the full mass range in the simulations (note that this includes halos for which $M_{\rm sh} > M_{\rm ph}$). The mean infall velocity $v_r^{\rm sh}(r)$ of secondary halos is defined along the line of separation r from the cluster centre, where the predicted tangential velocity components are zero when averaged over all halos. The velocity dispersion of secondary halos is considered separately in the radial and tangential directions, defined as $\sigma_r^{\rm sh}(r)$ and $\sigma_\perp^{\rm sh}(r)$ respectively. The number of galaxies $N_{\rm gal}$ contained in a given parent halo is dependent on its mass, as described by the HOD used to populate the simulations. The mean infall velocity of galaxies towards the primary halo is defined as $v_r^{\rm gal}(r)$, with predicted tangential components of zero when averaged for all galaxies. The velocity dispersion of galaxies is defined as $\sigma_r^{\rm gal}(r)$ and $\sigma_\perp^{\rm gal}(r)$ for the radial and tangential directions, respectively. In this work galaxy dynamics around a cluster are described by modelling the motion of their parent halos, and averaging over all values of $M_{\rm sh}$ weighted by $N_{\rm gal}(M_{\rm sh})$ in order to obtain predictions for $v_r^{\rm gal}(r)$, $\sigma_r^{\rm gal}(r)$ and $\sigma_\perp^{\rm gal}(r)$. The velocity dispersion of galaxies within a given halo is also examined, however their mean motion is assumed to equal that of the parent halo. A schematic diagram illustrating the properties of halos and galaxies in a stacked cluster dataset is shown in figure 2.6, including each of the different components which will be modelled in this work.

2.5 Conclusions

The technique of stacking clusters described here provides a vital tool with which to measure their statistical properties, and is also used with galaxy redshift survey data in order to observe the cluster-galaxy correlation function. The stacked cluster datasets

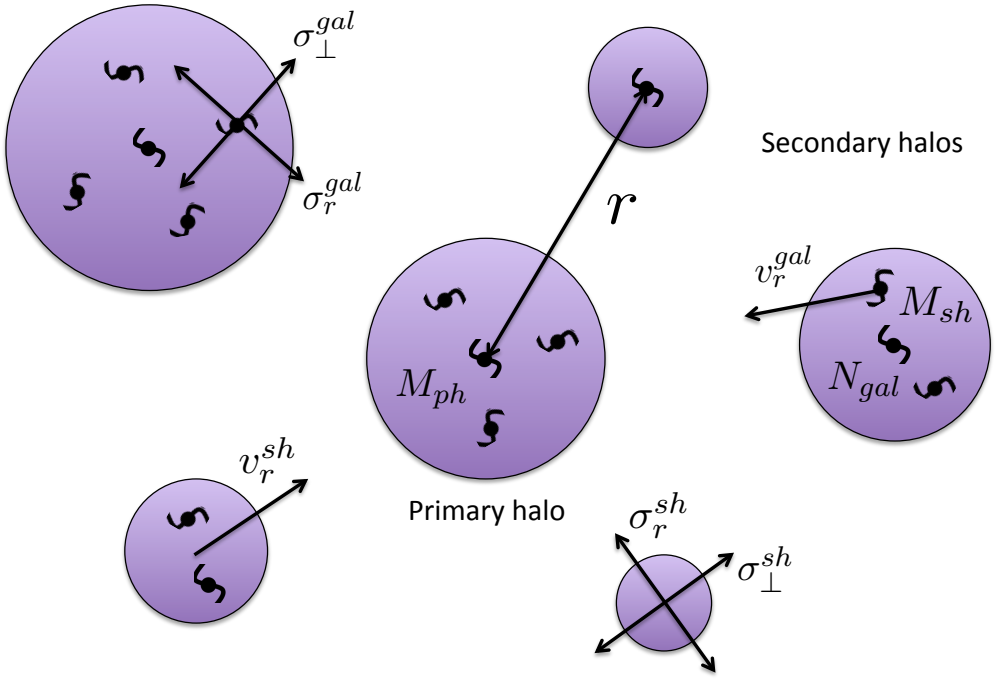

Figure 2.6. Schematic diagram of a stacked cluster dataset, defining the individual components of both halo and galaxy dynamics which are modelled in this work.

generated from the N-body simulations are used to create mock data, which are used in the following chapters to test models of infall and velocity dispersion. A numerical method for modelling the cluster-galaxy redshift space correlation function will also be applied to these mock data with the objective of reconstructing the primary halo mass. The galaxy dynamics observed around clusters in the N-body simulations will be used both to develop the models described above, and also to test their robustness in the quasi-linear regime.

Chapter 3

Infall of Galaxies onto Clusters in the Quasi-linear Regime

The mean streaming motion of galaxies towards an overdense region of space provides a direct measure of the local gravitational potential, and therefore a useful means by which to determine the matter density within that region. The infall of galaxies onto a cluster can consequently be used to probe the mass of the dark matter halo which resides at the centre, which compliments observations of large scale structure and gravitational lensing in providing a map of the dark matter distribution on cosmological scales. Galaxy infall is well understood in the linear regime, and can be accurately described on sufficiently large scales using linear perturbation theory. However the infall which occurs closer to the cluster centre, where the density is high compared to that of the background universe, begins to deviate from the predictions provided by linear theory, and an alternative approach is required at distances less than a few tens of Mpch^{-1} from the primary halo. These scales are of interest for many reasons including performing tests of General Relativity, and therefore it is important to have an accurate method with which to predict galaxy infall in this quasi-linear regime.

In this chapter, a model is presented which describes the mean streaming motions of galaxies around a cluster with given primary halo mass, and gives the radial dependence of this infall velocity relative to the cluster centre. The approach taken in this work is to combine the predictions from linear theory with the spherical evolution model which

provides a small scale approximation for galaxy peculiar velocity, introducing a method by which to transition smoothly between these two models and therefore obtain a full description of the infall velocity profile across both regimes. The predictions from this model are compared to the galaxy infall observed in stacked clusters from the N-body simulations, in order to determine its accuracy on quasi-linear scales. The model developed here is then used, together with a description of the galaxy density profile, to calculate the redshift space distortions which occur due to infall onto a cluster. This can be combined with a model which predicts the line of sight velocity dispersion for a given primary halo mass, to provide a complete description of the galaxy distribution in redshift space around a cluster.

3.1 Halo streaming model

3.1.1 Dark matter pairwise velocities

In linear theory, the mean pairwise velocity of dark matter particles at separation r can be calculated from the correlation function $\xi(r, a)$, which is related to the matter power spectrum $P(k, a)$ as follows:

$$\xi(r, a) = \int \frac{dk}{k} \frac{k^3 P(k, a)}{2\pi^2} j_0(kr) \tag{3.1}$$

where j_0 is a 0th order spherical Bessel function. The average relative velocity v_r^{dm} for a pair of dark matter particles is dependent on their separation, and can be derived from the pair-conservation equation given in Peebles (1980). This relation can be expressed in the following form, as described by Nityananda & Padmanabhan (1994):

$$\frac{\partial\ (1 + \bar{\xi})}{\partial\ \ln a} = -\frac{v_r^{dm}(r)}{Hr}\ 3\left[1 + \xi(r)\right] \tag{3.2}$$

where H is the Hubble constant at scale factor a. The volume averaged correlation function $\bar{\xi}(r, a)$ is defined as:

$$\bar{\xi}(r, a) = \frac{3}{r^3} \int_0^r \xi(x, a) x^2 dx \tag{3.3}$$

which is evaluated at the proper separation r. Equation 3.2 allows the mean pairwise velocity to be calculated from the evolution of $\bar{\xi}(r, a)$, assuming the number of pairs is

conserved. In linear theory, the volume averaged correlation function depends on the growth factor $D(a)$ as follows:

$$\bar{\xi}(r,a) = \left[\frac{D(a)}{D_0}\right]^2 \bar{\xi}(r,a_0) \tag{3.4}$$

where D_0 is the present day growth factor. Substituting the above relation and the dimensionless linear growth rate $f(\Omega) \equiv \partial \ln D / \partial \ln a$ into equation 3.2 yields the following expression:

$$-\frac{v_r^{dm}}{Hr} = \frac{2}{3} f(\Omega) \frac{\bar{\xi}(r,a)}{1+\xi(r,a)} \tag{3.5}$$

where $f(\Omega) \approx \Omega_m^{0.56}$ for a flat ΛCDM cosmology. The velocity v_r^{dm} describes the mean relative motion of pairs of dark matter particles along their line of separation r. The velocity components perpendicular to this are zero in linear theory, when averaged over all dark matter particle pairs.

The above relation between the dark matter density and velocity fields provides a prediction for the mean streaming motions of dark matter particles, however is only accurate on large scales ($r \geqslant 10$ Mpch^{-1}) where linear theory applies, and significantly underestimates the velocities on smaller scales (Juszkiewicz et al. (1999); Sheth et al. (2001)). This can be improved by calculating an expression for the evolution of $\xi_{dm}(r,a)$ and inserting this into the continuity equation as presented by Nityananda & Padmanabhan (1994), which was shown by Hamilton et al. (1991) to better describe the dark matter streaming on nonlinear scales.

In order to extend this description to predict the streaming motions of galaxies, which can be directly compared with observations, we need to understand how they trace the underlying dark matter distribution. The approach taken in this work is to develop a model for the pairwise velocities between dark matter halos of different masses, which is accurate on quasi-linear scales i.e. down to a few times the halo virial radius. These predictions can then be combined with halo occupation statistics and used to calculate the effective infall velocity profile of galaxies around a given cluster mass.

3.1.2 Halo pairwise velocities

In the first instance a description of the mean streaming motions for dark matter halos on linear scales is examined, with the aim of then extending this to accurately predict halo velocities in the quasi-linear regime. The halo streaming model used for this purpose is described in Sheth et al. (2001), and relates the mean pairwise velocity of dark matter particles to that of the halos they belong to. In order to derive this relation, a description of the halo-halo correlation function $\xi_{hh}(r, a)$ and its evolution is required. For halos with two different masses m_1 and m_2, the correlation function is related to that of the dark matter $\xi_{dm}(r, a)$ as follows:

$$\xi_{hh}(r, a) \approx b_1(m_1)b_2(m_2)\xi_{dm}(r, a) \tag{3.6}$$

where b_1 and b_2 are the bias values corresponding to the different halo masses. The bias factor $b(m)$ is well approximated for a halo of mass m by the following expression, as described by Mo & White (1996):

$$b(m) = 1 + \frac{\nu^2(m) - 1}{\delta_c \; D(a)/D_0} \tag{3.7}$$

where δ_c is the linearly-extrapolated critical density for collapse at the present day, and $\nu(m) \equiv \delta_c/\sigma(m)$. The term $\sigma(m)$ is defined as the r.m.s. overdensity fluctuation, calculated for a sphere with radius corresponding to the given halo mass. In this approximation the bias factor evolution is therefore given by:

$$\frac{\partial \; b(m)}{\partial \; \ln a} = f(\Omega) \left[1 - b(m)\right] \tag{3.8}$$

The expression for $\xi_{hh}(r, a)$ can be inserted into the pair-conservation formula given in equation 3.2, assuming that the present day velocity of a halo is equal to that of its centre-of-mass DM particle. The above approximations for the evolution of $b(m)$ and $\bar{\xi}_{dm}(r, a)$ can be used to obtain the following relation for the mean approach velocity $v_r^h(r)$ between two halos of different masses:

$$\frac{-v_r^h(r)}{Hr} 3 \left[1 + b_1 b_2 \xi_{dm}(r, a)\right] = \bar{\xi}_{dm}(r, a) f(\Omega) \left[b_1 + b_2\right] \tag{3.9}$$

The linear approximation for $v_r^{dm}(r)$ given in equation 3.5 can be substituted into the above expression to yield:

$$\frac{v_r^h(r)}{Hr} \approx \frac{v_r^{dm}(r)}{Hr}\left(\frac{b_1+b_2}{2}\right)\frac{1+\xi_{dm}(r,a)}{1+b_1b_2\xi_{dm}(r,a)} \tag{3.10}$$

where $v_r^h(r)$ is the mean relative velocity between halos along their line of separation r, with the perpendicular components equal to zero when averaged over all pairs. The above model provides a description of the mean streaming motion of halos and how it relates to that of the dark matter, and is accurate in the linear regime.

Here a fitting function introduced by Tinker et al. (2010) is used to calculate the bias value for a halo of virial mass M_{200}, defined as the mass enclosed by radius R_{200} within which the average halo density is 200 times that of the mean background density at the cluster redshift $\bar{\rho}_m$, i.e. $R_{200} = (3M_{200}/4\pi\bar{\rho}_m)^{\frac{1}{3}}$. The bias is parameterized in terms of the peak height in the linear density field $\nu = \delta_c/\sigma(m)$, where δ_c is the critical collapse density and $\sigma(m)$ is the r.m.s. matter variance on the scale of the halo radius R_{200}. The fitting formula for halo bias is given by:

$$b(\nu) = 1 - \frac{A\nu^a}{\nu^a + \delta_c^a} + B\nu^b + C\nu^c \tag{3.11}$$

where the fitted parameters corresponding to the definition of halo virial mass used here are as follows: $A = 1.00$, $B = 0.183$, $C = 0.265$, $a = 0.133$, $b = 1.50$, $c = 2.40$ and the value of the critical collapse density used is $\delta_c = 1.6577$. This expression for halo bias, which was developed from the model by Sheth & Tormen (1999), has been shown to be adequately insensitive to changes in both redshift and the chosen cosmology to use for the purposes here.

The fitting formula given in equation 3.11 allows the bias to be accurately determined for a halo of given virial mass at a specified redshift, which can then be inserted into equation 3.10 to give the mean approach velocity along the line of separation for two halos of different masses m_1 and m_2, as a function of scale r. Comparison with halo streaming velocities measured from N-body simulations shows a good agreement on linear scales, however the model begins to under-predict halo approach velocities seen in the simulations at radii of order tens of Mpch^{-1}, with more massive halos showing a divergence from the linear prediction at larger scales. This is unsurprising given that the model described above assumes a linear evolution of halo bias, and also that this bias is scale-independent.

These assumptions are known to be incorrect on small scales, and therefore a different approach must be considered in order to accurately model the streaming motions of halos in this regime.

In the following section a model for the mean approach velocities of halos on nonlinear scales will be examined and compared to the linear predictions described above, and a method presented with which to combine these two models. The goal of this is to provide a complete description of the mass and scale dependence of halo streaming motions, which is accurate across both the linear and nonlinear regimes.

3.2 Extension to nonlinear scales

3.2.1 Spherical evolution model

The spherical top hat evolution model presented by Gunn & Gott (1972) describes the evolution of the average density in a perturbation within given radius r, and also the speed at which this boundary subsequently evolves v_{pec} (Schechter (1980)). This depends on the density of the perturbation compared to that of the background universe, characterised by the parameter Δ_m as follows:

$$1 + \Delta_m(r) \equiv \frac{M_{enc}(r)}{4\pi r^3 \bar{\rho}_m/3} \tag{3.12}$$

where M_{enc} is the enclosed mass of the perturbation at radius r, which in this model remains constant as its boundary and average density evolve. An overdense perturbation will initially expand at a rate slightly slower than that of the Hubble flow, then will begin to contract, eventually turning around and collapsing. The perturbation turns around when this contraction exactly cancels out the expansion of the background universe, and subsequently collapses. In the spherical evolution model, the average perturbation density is parameterised as follows:

$$1 + \Delta_m(r) = \frac{f(\theta)}{f(U)} \tag{3.13}$$

where the function $f(\theta)$ is given by:

$$f(\theta) = \begin{cases} (\theta - \sin\theta)^2/(1-\cos\theta)^3 & \text{overdense} \\ (\sinh\theta - \theta)^2/(\cosh\theta - 1)^3 & \text{underdense} \end{cases} \tag{3.14}$$

The perturbation boundary evolution in this model is described by the following expression:

$$\frac{v_{pec}(r)}{H_0 r} = \frac{g(\theta)}{g(U)} - 1 \tag{3.15}$$

where the function $g(\theta)$ is given by:

$$g(\theta) = \begin{cases} \sin\theta(\theta - \sin\theta)/(1-\cos\theta)^2 & \text{overdense} \\ \sinh\theta(\sinh\theta - \theta)/(\cosh\theta - 1)^2 & \text{underdense} \end{cases} \tag{3.16}$$

and the parameter U is defined for either an open or closed universe as follows:

$$U = \begin{cases} \arccos(2/\Omega_m - 1) & \text{closed} \\ \ln(2/\Omega_m - 1 + \sqrt{(2/\Omega_m - 1)^2 - 1}) & \text{open} \end{cases} \tag{3.17}$$

These parametric expressions provided by the spherical top hat model describe the nonlinear growth of a density perturbation, and the velocity at which its boundary evolves. An overdense perturbation turns around when it is contracting at a rate which is equal to the Hubble flow, and therefore $-v_{pec}(r) = H_0 r$. This corresponds to a value of $\theta = \pi$ for the above parameterisation, and in the case of complete collapse it can be seen that $\theta \to 2\pi$. The spherical evolution model therefore gives the following expression for v_{pec} when expanding around the limit of complete collapse:

$$-\frac{v_{pec}}{H_0 r} \to \sqrt{\Omega_m(1+\Delta_m)} = \frac{\sqrt{2GM_{enc}/r}}{H_0 r} \tag{3.18}$$

where $\Omega_m = 8\pi G\bar{\rho}_m/3H_0^2$ is the matter density parameter at the present time. The above result arises from the limiting case where $\Delta_m \gg 1$, and is therefore only accurate on suitably small scales. It is interesting to note that the form of v_{pec} in this limit is exactly the same as that of the escape velocity at distance r from a body of mass M_{enc}.

The above approximation provides a description of the mass and scale dependence of

v_{pec}, valid on nonlinear scales. In order to apply this to the streaming of dark matter halos, the radial dependence of M_{enc} for a halo of given mass must be considered. As the spherical evolution model in this limit only applies on small scales, the two-halo term can be neglected and it will be assumed that all the mass contributing to M_{enc} originates from a single halo. This can therefore be modelled as the mass enclosed by an NFW profile corresponding to the halo mass of interest, obtaining the concentration parameter from relations provided by Mandelbaum et al. (2008). The process of evaluating M_{enc} for an NFW density profile is described in greater detail in the following chapter, where the expression for halo mass dependence of the concentration parameter is also shown. This is then used to calculate $\Delta_m(r)$ for a halo of given mass, and therefore predict v_{pec} in the nonlinear regime. As the mean approach velocities between halos of different masses are of interest here, the average halo virial mass $M_{\rm av}$ is taken in each case and the corresponding NFW profile used to calculate $\Delta_m(r)$.

The above model shows good agreement with the N-body simulations, out to several times the virial radii of the halos for which results were compared. As would be expected, the mean streaming predictions are inaccurate at larger scales where the assumption $\Delta_m \gg 1$ is no longer valid, with the model describing the simulations well out to greater radii for more massive halos. This compliments the linear halo streaming model discussed in the previous section, however does not give us a full description for the scale dependence of halo approach velocities, as in the quasi-linear regime neither model provides adequate predictions and some combination of the two is required. In the next subsection a method will be examined with which to transition smoothly between these models, and thus provide a complete description of halo streaming motions on both linear and nonlinear scales.

3.2.2 Transition model

Firstly, the linear halo streaming velocities described by equation 3.10 will be defined as $v_r^{\rm lin}(r)$, and the spherical evolution model in the limit of complete collapse described by equation 3.18 as $v_r^{\rm nl}(r)$. The resultant mean approach velocity for halos as a function of scale, $v_r^{\rm h}(r)$, will be obtained with a combination of these two models. A transition radius r_t is defined, where nonlinear behaviour begins to significantly effect the halo streaming motions, and above which the velocities are well described by the linear model. The

following fitting formula is introduced for $v_r^{\rm h}$ at $r \leqslant r_t$:

$$v_r^{\rm h}(r) = v_r^{\rm nl}(r) - \alpha v_r^{\rm nl}(r_t) + v_r^{\rm lin}(r) \tag{3.19}$$

where

$$\alpha = 1 - \exp\left(\frac{-k_t r}{r_t - r}\right) \tag{3.20}$$

and the fitted parameters r_t and k_t are both a function of halo mass. The above fitting formula corresponds to adding a scale-dependent fraction of $v_r^{\rm nl}(r)$ to the linear model, which exponentially transitions from 1 to 0 between $r = 0$ and $r = r_t$. The parameter k_t indicates the sharpness of the transition, with higher values corresponding to a more rapid drop off in the influence of the nonlinear model, and therefore a higher degree of linearity in the quasi-linear regime. At scales above r_t the halo velocities are assumed to be completely linear, i.e. are described by $v_r^{\rm lin}(r)$.

Figure 3.1 shows the prediction for halo mean streaming velocities using the linear, spherical evolution and transition models, for various different halo mass bins. These predictions are compared to the halo velocities $v_r^{\rm sh}$ seen in the N-body simulations, which are described in the previous chapter. The transition model shown is the best fit to the simulation data for each halo mass bin, with the fitted parameters r_t and k_t stated in each case. It can be seen from figure 3.1 that, for the halo masses shown, the transition model provides a significant improvement on using either the linear or spherical evolution model to predict halo streaming velocities in the quasi-linear regime. It also provides quantitive information about the scale at which nonlinearities begin to take effect, and how this depends on halo mass.

In order to generalise this approach to predict $v_r^{\rm sh}(r)$ for a pair of halos with any given masses, we need to investigate in more detail the halo mass dependence of the fitted parameters r_t and k_t. To achieve this, best fit transition models were obtained from the simulation data for a single primary halo mass bin with a range of secondary halo masses, and this was then repeated for four different primary halo mass bins. This allows the dependence of the transition model parameters on secondary halo mass to be examined for each individual case, and these measurements can also be combined to obtain a relation to the average halo mass $M_{\rm av}$. Figure 3.2 shows the fitted parameters r_t and k_t as a function of both secondary and average halo mass, using results from all four primary

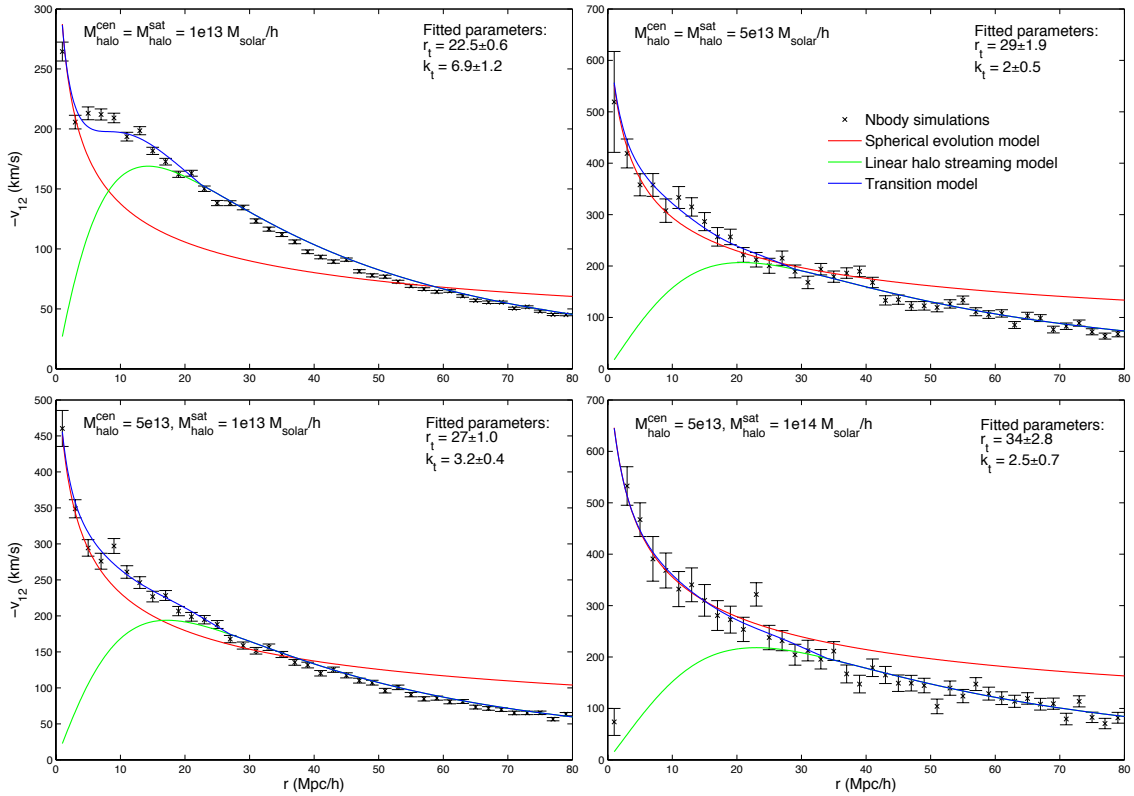

Figure 3.1. Mean approach velocity of dark matter halos as a function of scale for different models, compared to measurements from the simulations. Predictions are shown for the linear (green line), spherical evolution (red line) and transition (blue line) models. Black crosses show the mean halo velocities measured in the simulations. Results are shown for streaming motions between halos of both equal (top) and different (bottom) masses, for two different mass bins in each category. Best fit parameters for the transition model are stated in each case. Note that the axis label v_{12} represents the mean halo streaming velocity $v_r^{\rm sh}(r)$, and the figure labels $M_{\rm halo}^{\rm cen} = M_{\rm ph}$ and $M_{\rm halo}^{\rm sat} = M_{\rm sh}$.

halo mass bins. A clear trend can be seen between $\log M_{\rm av}$ and both parameters, with a positive correlation seen for the transition radius r_t, and a negative correlation for k_t. The same trends can be seen with secondary halo mass for individual primary halo mass bins, although this is less clear for the larger halos, where the results are more noisy due to the lower number of halos in these mass bins. The results when combined however are self-consistent, and allow the dependence on $M_{\rm av}$ to be calculated for both parameters in the transition model.

Assuming a power law relation to average halo mass for both parameters, the following

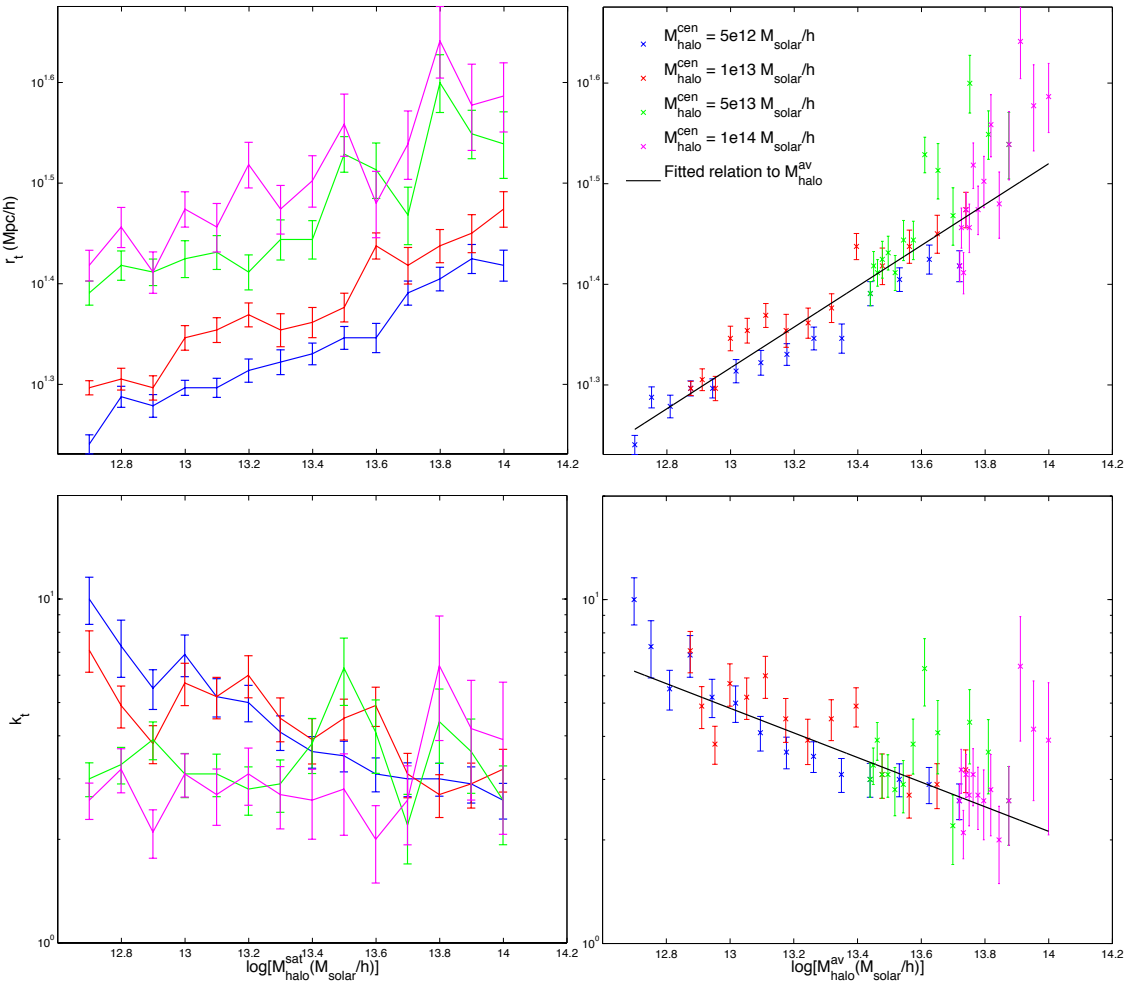

Figure 3.2. Transition model parameters fitted from N-body simulations, as a function of halo mass. Top panels show the dependence of the transition radius r_t on both secondary (left) and average (right) halo mass, bottom panels show the equivalent dependence for k_t. Results are shown for four different primary halo mass bins centred on 5×10^{12} (blue), 1×10^{13} (red), 5×10^{13} (green) and 1×10^{14} (pink) $\mathrm{M}_{solar} h^{-1}$. Black lines show the best fit relation to average halo mass for both parameters. Note that the figure labels $M^{\rm cen}_{\rm halo} = M_{\rm ph}$, $M^{\rm sat}_{\rm halo} = M_{\rm sh}$ and $M^{\rm av}_{\rm halo} = M_{\rm av}$.

best fit relation for the dependence of r_t and k_t on $M_{\rm av}$ is obtained:

$$r_t = 0.0509 {M_{\rm av}}^{0.20} \tag{3.21}$$

$$k_t = 169000 {M_{\rm av}}^{-0.35} \tag{3.22}$$

The above expressions can be used to calculate the transition model parameters for any given combination of halo masses, and therefore predict their mean approach velocity as a function of scale. In the following section this model will be used, together with halo occupation statistics, as a basis with which to predict the effective galaxy infall profile around a cluster of given mass.

3.3 Galaxy infall onto clusters

3.3.1 Galaxy number density

In the previous sections the mean streaming velocities of both dark matter particles and their parent halos have been examined, however as these cannot be directly observed we need to consider how our predictions relate to the mean streaming motions of galaxies. The focus of this work will be to describe the infall of galaxies onto massive clusters, and in particular how this depends on the cluster mass. Galaxies can be seen as tracer particles of the underlying dark matter distribution, where the galaxy bias provides a large-scale statistical description of how galaxies trace the density field, by relating the galaxy correlation function to that of the dark matter. A more localised approach is to use a halo occupation distribution (HOD), which predicts the number of galaxies expected to populate a dark matter halo, as a function of its mass. This statistic provides a useful way of relating the galaxy distribution to that of the dark matter halos, and this approach will be used to extend the model for halo streaming velocities and describe the dynamics of galaxies around massive clusters.

In order to predict the effective galaxy infall profile around a primary halo of mass $M_{\rm ph}$, we first need to model the contributions to the galaxy density profile from secondary halos of different masses. The number density of halos of mass $M_{\rm sh}$ at distance r from the primary halo can be obtained from the halo-halo correlation function (defined in equation

3.6) as follows:

$$\rho_h(r, M_{\rm sh}) = \bar{\rho}_h(M_{\rm sh})[1 + \xi_{hh}(r, M_{\rm ph}, M_{\rm sh})] \tag{3.23}$$

where $\bar{\rho}_h(m)$ is the mean background density of halos of mass m, which is calculated using the universal halo mass function provided by Sheth & Tormen (1999). The contribution to the total galaxy number density from halos of mass $M_{\rm sh}$ is therefore given by

$$\rho_{gal}(r, M_{\rm sh}) = \langle N_{\rm gal}(M_{\rm sh})\rangle \rho_h(r, M_{\rm sh}) \tag{3.24}$$

where $\langle N_{\rm gal}(m)\rangle$ is the mean number of galaxies which populate a halo of mass m. This can then be summed over all secondary halo masses to obtain the galaxy density profile around a primary halo of given mass.

To test the accuracy of these predictions they can be compared to results from the simulations, which were populated with galaxies using the following HOD taken from Zehavi et al. (2011):

$$\begin{aligned}&\langle N_{\rm gal}(M_h)\rangle = \\ &\quad \tfrac{1}{2}\left[1 + {\rm erf}\left(\tfrac{\log M_h - \log M_{min}}{\sigma_{\log M}}\right)\right]\left[1 + \left(\tfrac{M_h - M_0}{M_1'}\right)^{\alpha}\right]\end{aligned} \tag{3.25}$$

where M_h is the halo virial mass defined with respect to the mean background density, as discussed in section 2.2. A full description of the method used to populate the dark matter simulations with galaxies, including a summary of the HOD parameter values, is given in the previous chapter. In order to measure the effective density and infall velocity profiles around halos of a given mass, clusters from the simulations which fall in the specified mass bin are stacked, taking the galaxy positions and velocities relative to the primary halo. The average galaxy number density and infall velocity can then be calculated at distance r from the primary halo, and compared with the predictions provided by the model. The errors on both the density and velocity observations are obtained using a resampling method similar to the jackknife technique, with the stacked clusters for a given primary halo mass bin divided into ten randomly distributed subsets and the galaxy density and infall profiles measured in each case. The mean is then evaluated for individual radial bins, and the standard deviation of results from the different groups of clusters used to estimate the errors on the mean density and infall velocity observed for datasets from the

simulations.

Given that the HOD used to populate the simulations is known, the expression for $\langle N_{\rm gal}(M_h)\rangle$ can be inserted into equation 3.24 and then integrated over secondary halo mass to obtain a prediction of the total galaxy density profile $\rho_{gal}^{tot}(r)$ around a set of stacked clusters in the simulations, for a given primary halo mass. Figure 3.3 shows the average galaxy number density measured from the populated simulations for four different primary halo mass bins, compared to the predictions using both a linear and nonlinear approximation of the halo-halo correlation function $\xi_{hh}(r)$. The different versions of $\xi_{hh}(r)$ are obtained by using either the linear or nonlinear dark matter power spectrum to calculate $\xi_{dm}(r)$ in equation 3.6. It can be seen that the predictions are in relatively good agreement with the results from the simulations, with the calculation using a nonlinear approximation of $\xi_{hh}(r)$ providing an improvement on small scales ($r < 5$ Mpch^{-1}), as would be expected. The nonlinear definition of $\xi_{hh}(r)$ will therefore be used to calculate the galaxy density profile, which will then be combined with the halo streaming model in order to predict the effective galaxy infall profile for stacked clusters in the simulations.

3.3.2 Galaxy infall model

In section 3.2 a transition halo streaming model was introduced, which describes the mean approach velocities of halos with different masses as a function of scale, and was shown to be accurate in the quasi-linear regime. Expressions were also obtained for the parameters which characterise the transition to nonlinear behaviour, showing their dependence on the average halo mass. These relations allow the mean relative velocity to be calculated between two halos of any given masses, as a function of their separation. In order to infer the effective galaxy infall profile around a primary halo of mass $M_{\rm ph}$, we need to consider the mean infall velocity which results from the streaming motions of secondary halos with different masses, weighting these by the number of galaxies each one contributes to the statistic. The number density of galaxies $\rho_{gal}(r)$ which are in parent halos of mass $M_{\rm sh}$, given as a function of distance from the primary halo, has been previously defined in equation 3.24. The mean infall velocity of galaxies $v_r^{\rm gal}(r)$ relative to a primary halo of mass $M_{\rm ph}$ can therefore be expressed in terms of the halo streaming velocity $v_r^{\rm sh}(r)$ as

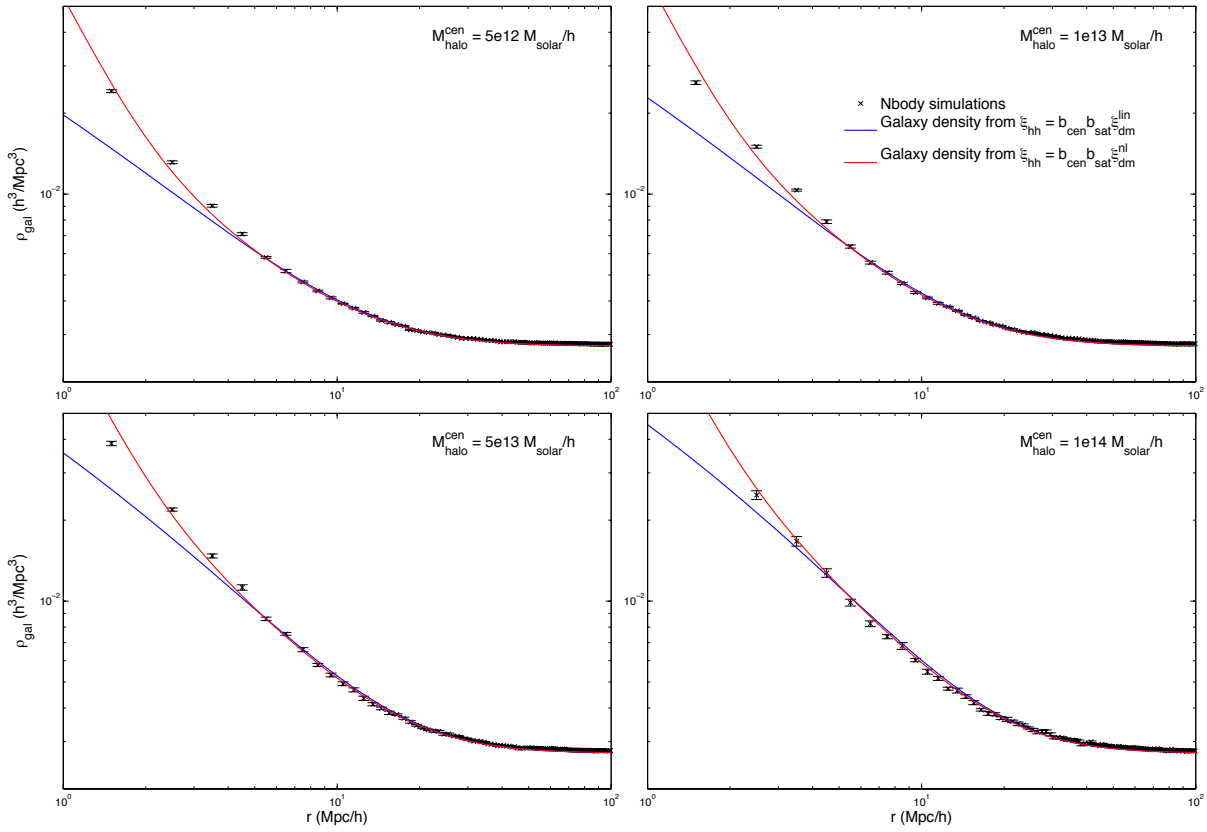

Figure 3.3. Average galaxy number density profiles as measured from the simulations (black crosses), compared to predictions calculated from the linear (blue line) and nonlinear (red line) halo-halo correlation function. Results are shown for four different primary halo mass bins, centred on (from top left to bottom right) 5×10^{12}, 1×10^{13}, 5×10^{13} and 1×10^{14} $\mathrm{M}_{solar}h^{-1}$. Note that the figure labels $b_{\rm cen}$ and $b_{\rm sat}$ represent the bias values corresponding to the primary and secondary halos respectively, and $M^{\rm cen}_{\rm halo} = M_{\rm ph}$.

follows:

$$v_r^{\rm gal}(r) = \frac{1}{\rho^{tot}_{gal}(r)} \int_0^\infty \rho_{gal}(r, M_{\rm sh}) v_r^{\rm sh}(r, M_{\rm sh}) dM_{\rm sh} \tag{3.26}$$

where for a given $M_{\rm sh}$ the corresponding transition model parameters r_t and k_t are calculated from equations 3.21 and 3.22 respectively, and used to obtain the mean approach velocity of the halo $v_r^{\rm sh}(r)$. In practice the above integral is evaluated over the mass range $10^{11} \leqslant M_{\rm sh} \leqslant 10^{16}$ $\mathrm{M}_{solar}h^{-1}$, as realistically all halos containing galaxies should fall well within these limits. The total galaxy number density $\rho^{tot}_{gal}(r)$ which is described in the previous section is also calculated by summing over this mass range. The above method allows a prediction to be obtained for the effective galaxy infall profile around stacked

clusters in the simulations, for a given primary halo mass.

Figure 3.4 shows the mean galaxy infall velocity as measured from the populated simulations for the same four primary halo mass bins shown previously, compared to the predictions obtained using both the transition and linear halo streaming models to calculate $v_r^{\rm sh}(r, M_{\rm sh})$ in equation 3.26. It can be seen that, as for the halo streaming motions, the transition model provides a significant improvement on the linear model for galaxy infall velocity predictions in the quasi-linear regime. In the case of the transition model there is a tendency to over-predict the infall of galaxies on very small scales, however this is unsurprising given that a one-halo term has not been included in the galaxy velocity model, nor have the effects of exclusion been accounted for. Galaxies within the primary halo itself are highly virialised, and therefore do not show a net infall towards the centre of the cluster. Halos within the exclusion radius of the primary halo (approximately equal to the sum of their virial radii) are not counted as separate objects, and instead form a single, more massive halo. Both of these effects act to suppress the mean infall velocity of galaxies close to the cluster centre, and would need to be included in the model to more accurately describe the galaxy infall profile on these scales. However, as the only interest here is in galaxy infall velocities outside a few times the virial radius of the primary halo, these effects can be neglected and the measurements cut off below a certain scale. The effective galaxy infall profiles predicted by the model show a strong agreement with results seen in the simulations on the scales relevant to this work, suggesting that the transition model presented here provides an accurate description of halo streaming velocities in the quasi-linear regime.

It has been demonstrated that the model introduced in this work can reproduce both the average density and effective infall velocity profiles of galaxies around stacked clusters in the simulations, with a good degree of accuracy down to scales of a few Mpch^{-1}. However, as neither of these can be directly inferred from observations, we need to use the model predictions to produce results which can be compared to measurements from galaxy redshift surveys. In the next section it is examined how the infall which occurs around clusters creates distortions in the galaxy number density observed in redshift space, and the description of galaxy density and velocity profiles presented here is used to model these distortions for a cluster of given mass.

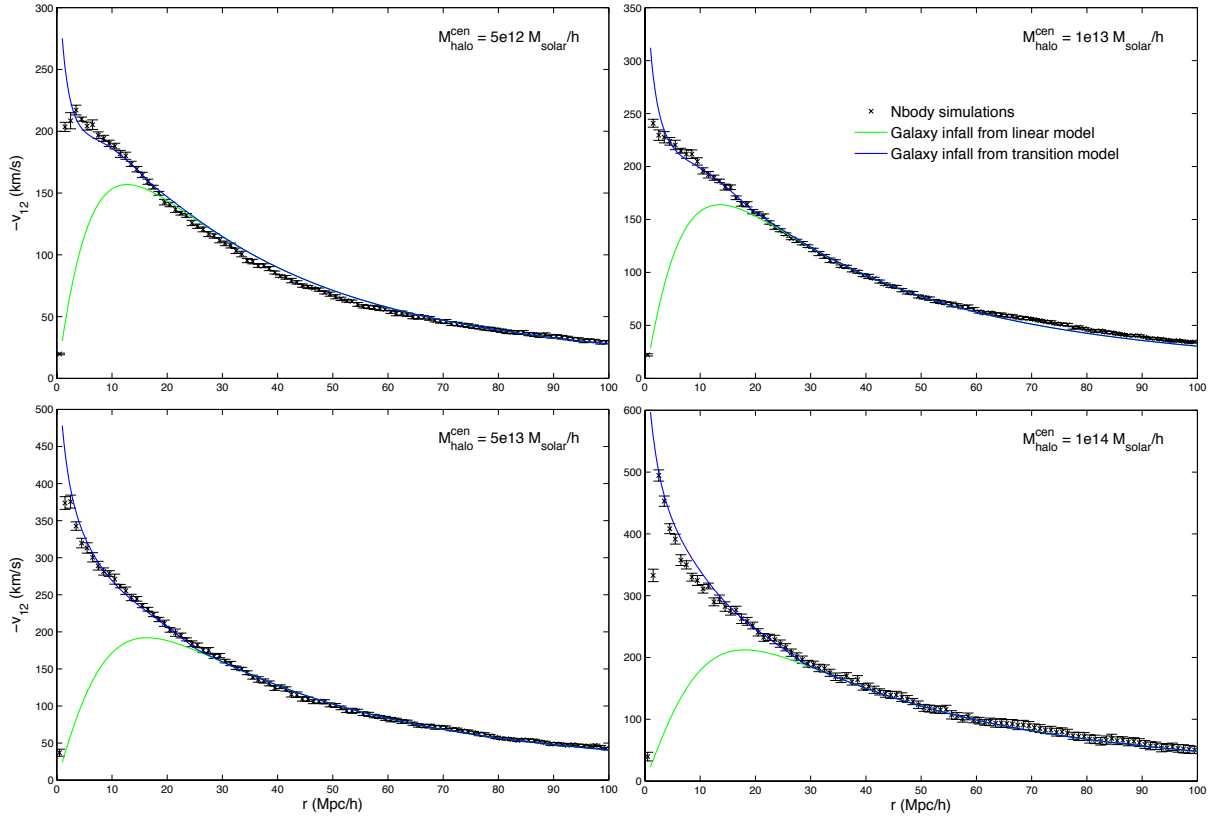

Figure 3.4. Effective galaxy infall velocity profiles as measured from the simulations (black crosses), compared to predictions calculated using the transition (blue line) and linear (green line) halo streaming models. Results are shown for the same primary halo mass bins defined in figure 3.3. Note that the axis label v_{12} represents the mean galaxy infall velocity $v_r^{\rm gal}(r)$, and the figure label $M_{\rm halo}^{\rm cen} = M_{\rm ph}$.

3.4 Modelling the cosmic onion

3.4.1 Redshift space distortions

The use of redshift as a measure of distance in galaxy surveys assumes that their observed motion is due only to the cosmological expansion (i.e. their comoving coordinates remain fixed), however in reality galaxies in an over or under-dense region will be influenced by the surrounding gravitational potential, resulting in an additional peculiar velocity relative to the Hubble flow. Galaxies in proximity to a massive cluster will therefore show a change in apparent distance due to their peculiar velocities, depending on their position relative to the centre of the cluster. This effect results in distortions to the galaxy density distribution when measured in redshift space, causing it to appear squashed along the line of sight on

scales where galaxies are infalling coherently towards the cluster centre. Inside the virial radius of the primary dark matter halo, the galaxies are no longer infalling and instead undergo virial motion within the primary halo which causes their distribution in redshift space to appear extremely stretched out along the line of sight, known as the Fingers of God effect. The combined result of these motions is to distort the two dimensional cluster-galaxy correlation function in redshift space, causing it to resemble a 'cosmic onion'. These redshift space distortions (RSD) depend on the mass of the primary halo in the cluster, and both the galaxy density in real space and the effective infall velocity profile need to be known in order to predict the galaxy number density in redshift space. In this section the model for galaxy infall onto clusters presented in this work, combined with the predictions for galaxy density profiles around halos, will be used to describe RSD near massive clusters in the simulations with the potential application of providing constraints on their primary halo mass.

A numerical model is employed in order to predict the RSD around a cluster due to galaxy infall, which predicts the galaxy number density in redshift space ρ^{z}_{gal} at position r_π, r_σ relative to the cluster centre, where r_π is the separation along the line of sight and r_σ is the projected distance on the sky. Firstly, the galaxy number density is calculated for the given primary halo mass in real space on a fine grid in r_π, r_σ coordinates, using the galaxy density profile $\rho^{tot}_{gal}(r)$ described in the previous section to evaluate the density at each point on the grid. The effective galaxy infall profile $v_r^{\rm gal}(r)$ prediction for the same cluster mass is then applied to the real space density grid, calculating a new position for each pixel in redshift space. It is important to note that only the LOS component of the infall velocity v_{los} affects the pixel position in redshift space, shifting it in the r_π direction by the following amount:

$$\Delta r_\pi = \frac{v_{los}(r_\pi, r_\sigma)}{H} \tag{3.27}$$

with no shift in the r_σ direction, as this is perpendicular to the LOS. These unevenly spaced points describing the galaxy density distribution are then binned onto a coarse grid in r_π, r_σ coordinates, providing a smooth description of the galaxy number density in redshift space. This allows the two dimensional cluster-galaxy redshift space correlation function, hereafter known as the cosmic onion, to be predicted for a given primary halo mass.

3.4.2 Line of sight velocity dispersion

The Fingers of God effect, which acts to stretch out the galaxy distribution along the line of sight in redshift space for the primary halo, has been previously described in this section. However the galaxies infalling toward the cluster centre are also undergoing virial motion within their parent halos, and this leads to a velocity dispersion which is related to parent halo mass. Provided enough clusters are stacked, these random motions should cancel each other out resulting in a coherent net infall velocity, however they will produce an additional velocity dispersion which has the effect of stretching out the cosmic onion along the line of sight. This counteracts to some degree the squashing which results from the net galaxy infall, and therefore it is important to include this in the cosmic onion model in order to accurately describe the RSD around a galaxy cluster.

Here, the velocity dispersion seen due to galaxy virial motions is accounted for by measuring the standard deviation of the LOS velocity component for galaxies in the simulations, as a function of position for a given primary halo mass. This standard deviation $\sigma_{\rm los}^{\rm gal}(r_\pi, r_\sigma)$ is evaluated at each pixel on a coarse grid in real space, for stacked clusters in the simulations of a specified mass. Figure 3.5 shows the measurements of $\sigma_{\rm los}^{\rm gal}(r_\pi, r_\sigma)$ obtained from the simulations, for four different primary halo mass bins. It can be seen that the average LOS velocity dispersion near a galaxy cluster increases as a function of its primary halo mass, which is to be expected given that more massive halos tend to reside near other large halos, which are known to exhibit a greater velocity dispersion in their galaxy virial motion. For each individual mass bin $\sigma_{\rm los}^{\rm gal}(r_\pi, r_\sigma)$ is seen to increase with distance from the primary halo, which is due to the fact that at greater separations the surrounding galaxies are moving less coherently with the cluster, therefore inducing an extra velocity dispersion in addition to that caused by their virial motion. It is worth noting also that on very small scales (around the primary halo virial radius) the LOS velocity dispersion is expected to increase again for more massive primary halos due to the virial motion of their galaxies, as can be seen for the largest halo mass bin shown in figure 3.5. It is interesting to note that these results from the simulations are seen to be spherically asymmetric, and this would have to be accounted for in any potential model for $\sigma_{\rm los}^{\rm gal}(r_\pi, r_\sigma)$ as will be discussed in the following chapter.

The LOS velocity dispersion is added to the RSD model after the pixels in the galaxy number density grid have been shifted to their positions in redshift space, by applying a

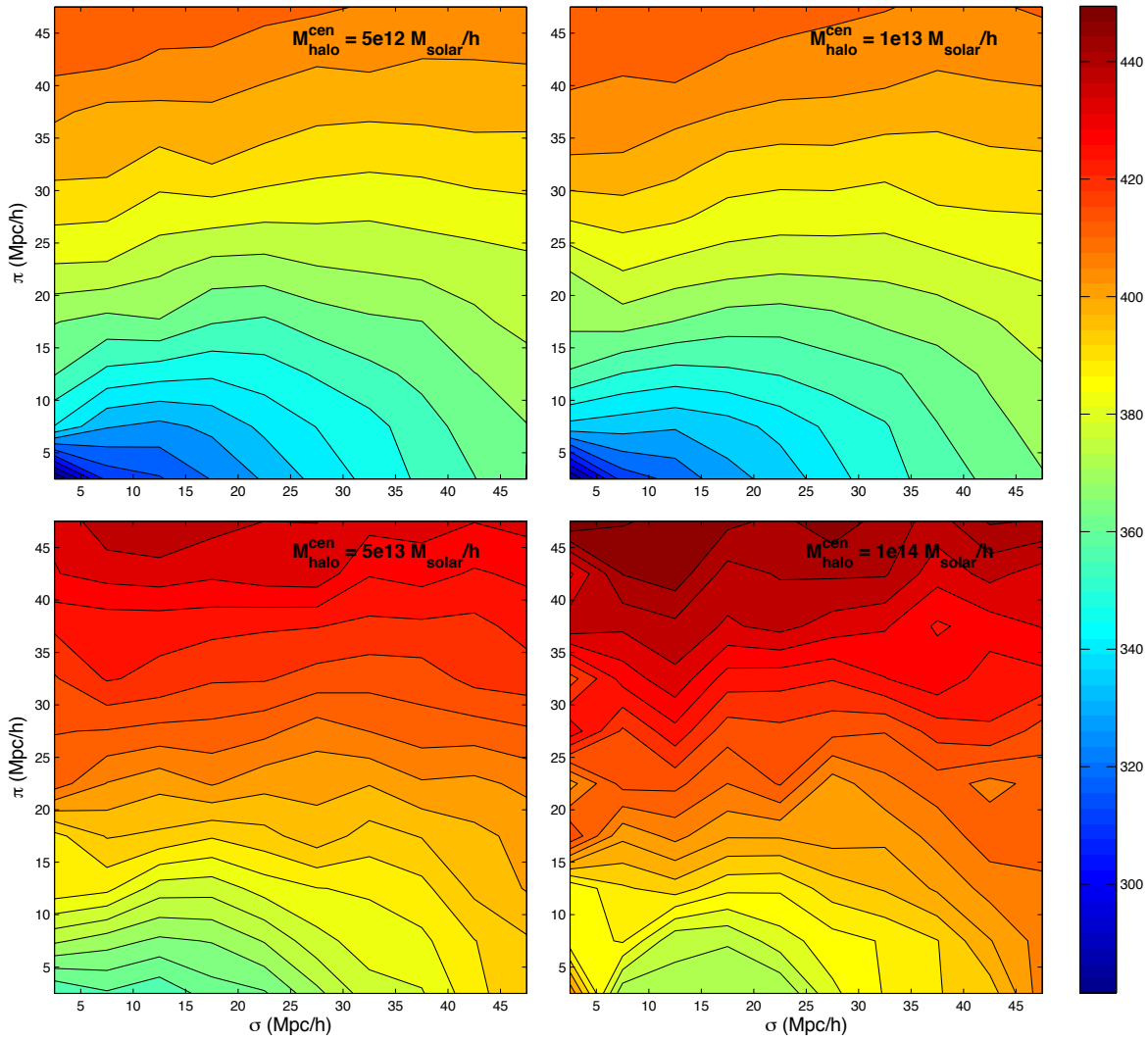

Figure 3.5. Line of sight velocity dispersion measured for galaxies in stacked clusters from the simulations, as a function of position relative to the cluster centre. Results are shown for the following primary halo mass bins (from top left to bottom right): 5×10^{12}, 1×10^{13}, 5×10^{13} and 1×10^{14} $\mathrm{M}_{solar} h^{-1}$. The colour bar represents the line of sight velocity dispersion in units of km/s, and the figure labels $\pi = r_\pi$, $\sigma = r_\sigma$ and $M^{\mathrm{cen}}_{\mathrm{halo}} = M_{\mathrm{ph}}$.

Gaussian convolution of width $\sigma_{\rm los}^{\rm gal}(r_\pi, r_\sigma)/H$ as measured at the pixel coordinates in real space. This method is found to provide reasonably accurate predictions of the velocity dispersion seen around stacked clusters from the simulations, in the absence of a full analytical description. Figure 3.6 shows the predictions of the average galaxy number density in redshift space using the numerical cosmic onion model, both with and without the inclusion of a velocity dispersion, compared to results from stacked clusters in the simulations for the three largest primary halo mass bins shown in figure 3.5. Here, the galaxy density in redshift space is obtained from the simulations by taking the LOS in the z direction, evaluating the shift in position for each individual galaxy by inserting the z component of its velocity into equation 3.27. Having calculated the galaxy positions in redshift space, their number density is then measured on a grid in r_π, r_σ coordinates. The assumption of a constant LOS is valid provided that the angular diameter of the cluster on the sky is sufficiently small, which is the case for scales relevant to this work. It can be seen from figure 3.6 that the predictions for galaxy number density in redshift space show good agreement with the results seen for stacked clusters in the simulations, when a Gaussian velocity dispersion is included in the cosmic onion model. It is also demonstrated that, if the velocity dispersion due to galaxy virial motions is not accounted for, the resulting predictions of the galaxy density distribution in redshift space appear squashed to a much greater degree along the LOS than those observed in the simulations, due to the absence of the stretching out effect that this dispersion has on the cosmic onion. This would result in a significant under-prediction of the primary halo mass, should an attempt be made to constrain this from RSD without considering the effects of LOS velocity dispersion.

3.5 Conclusions

In this chapter a model has been presented which describes the galaxy infall velocity profile around a cluster, and how this varies with primary halo mass. The approach taken here has been to combine the predictions from a linear halo streaming model, which are only valid at sufficiently large distances from the cluster centre, with those from the spherical evolution model in the limit of complete collapse which is only accurate on small scales. A method was introduced by which to transition smoothly between these models using a fitting function for galaxy infall velocity, and the halo mass dependence of the parameters for this model obtained by examining the infall for stacked clusters in the simulations with

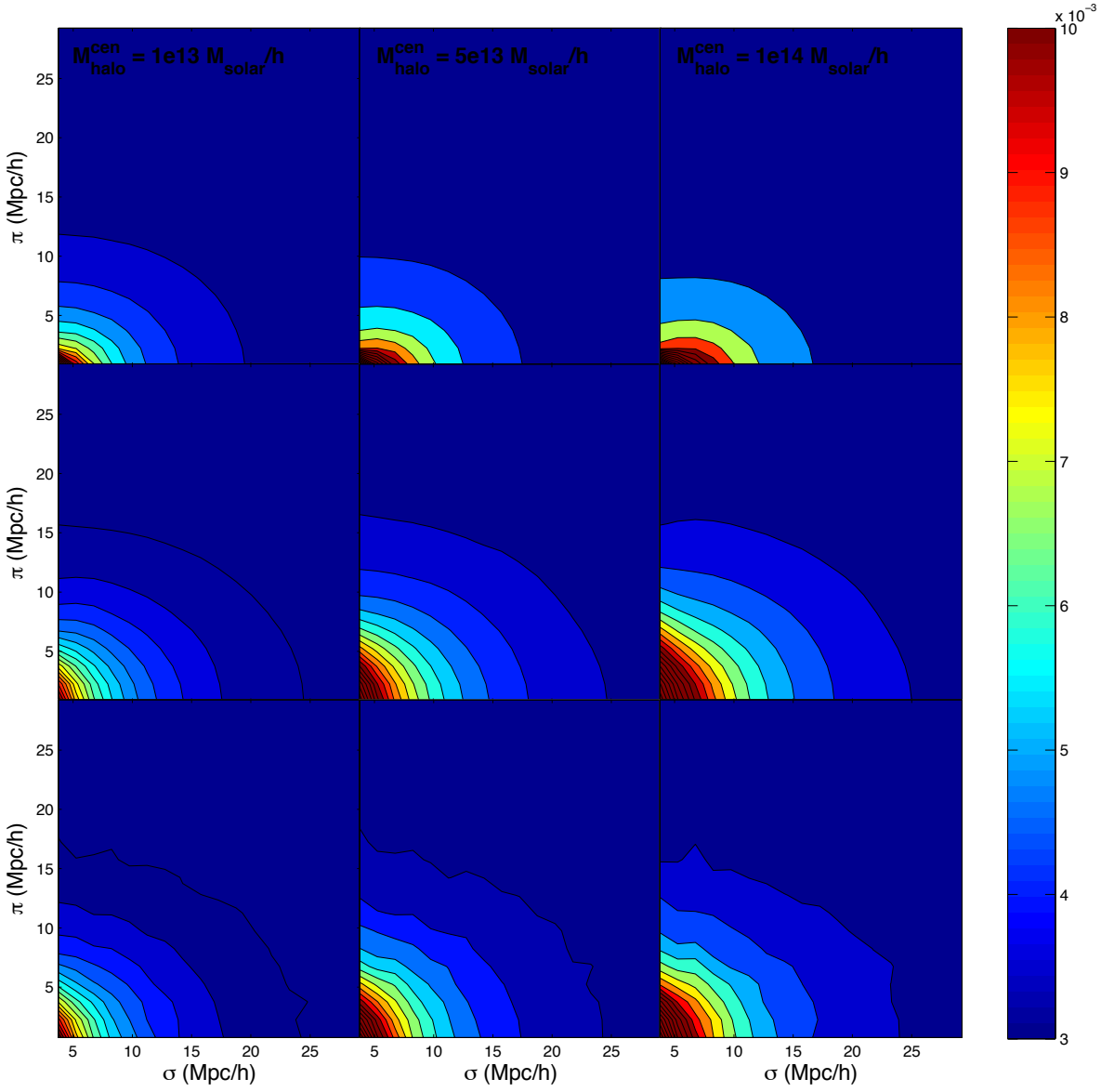

Figure 3.6. Average galaxy number density in redshift space for clusters with different primary halo masses, as a function of position relative to the cluster centre. Predictions are shown for the cosmic onion model using both infall only (top), and with a line of sight velocity dispersion added (middle), compared to measurements from stacked clusters in the simulations (bottom). Results are shown for the three largest primary halo mass bins defined in figure 3.5, with increasing cluster mass from left to right. The colour bar represents the galaxy number density in units of $\mathrm{Mpc}^{-3}h^3$, and the figure labels $\pi = r_\pi$, $\sigma = r_\sigma$ and $M^{\mathrm{cen}}_{\mathrm{halo}} = M_{\mathrm{ph}}$.

various different primary halo mass bins. The transition model was then used to predict the redshift space distortions which arise from infall around clusters, by combining this with a description for the galaxy density profile and measurements of the LOS velocity dispersion obtained directly from the simulations. A numerical method was employed to apply the resulting RSD, and calculate the galaxy distribution in redshift space for a cluster of given mass. Comparison with simulations demonstrated a good agreement between predictions from the transition model and the observed galaxy infall profile, with the model providing an accurate description of infall in the quasi-linear regime. The redshift space galaxy density calculated by the numerical cosmic onion model also showed a qualitative agreement with measurements from stacked clusters in the simulations, provided that the effects of LOS velocity dispersion were accounted for.

The transition model for galaxy infall which was discussed above could be potentially improved by investigating several factors in more detail, which is left as future work. Firstly, the halo mass dependence obtained for the transition model parameters could be examined more closely as this is seen to be less accurate for large clusters, and it would therefore be useful to try alternative forms to the power law variation assumed here. It would also be helpful to investigate the slight inaccuracies observed in the predicted galaxy density profiles shown in figure 3.3, especially for higher primary halo masses. This is of vital importance as a precise description of the original real space density is required when applying RSD using the numerical cosmic onion model, in order to calculate the resulting galaxy distribution in redshift space. In addition to this, as the predictions for both the galaxy density and infall velocity profiles have only been tested with simulations at a single redshift, it would be essential to compare these with observations at a range of different times so that any potential dependence on redshift can be examined, before the models could be applied more generally to galaxy redshift survey data. Finally, the LOS velocity dispersion used to calculate RSD in the cosmic onion model is currently obtained by measuring $\sigma_{\rm los}^{\rm gal}(r_\pi, r_\sigma)$ directly from the simulations for each set of stacked clusters, however in order to apply this model to real data we need a method for predicting the galaxy velocity dispersion around a given primary halo mass. The development of a model which describes the LOS velocity dispersion as a function of position relative to the cluster centre, and how this depends on halo mass, will be the subject of investigation in the following chapter.

This page was intentionally left blank

Chapter 4

Galaxy velocity dispersion in the infall region around clusters

It is of vital importance to include a velocity dispersion when attempting to model the galaxy distribution around clusters in redshift space, as was shown in the previous chapter. Galaxy velocity dispersion has the effect of elongating the density distribution along the line of sight, which counteracts the squashing due to infall, and so failure to account for this would result in an increased apparent infall when comparing the model to results from the simulations. This would therefore lead to a significant underestimation of the primary halo mass when obtaining constraints from the redshift space distortions. A simple approach to this problem was introduced in the previous chapter, where the galaxy LOS velocity dispersion was measured directly from stacked clusters in the simulations for a given halo mass, as a function of position in real space relative to the cluster centre. The observed velocity dispersion was then applied as a Gaussian convolution to the galaxy distribution in redshift space as predicted from infall alone, in order to obtain the modelled density around a cluster of specified mass in redshift space.

In practice however, we need a model which predicts the galaxy LOS velocity dispersion around a cluster of given primary halo mass in order to provide a full description of the galaxy distribution in redshift space. In current work this is often approximated as a scale-independent constant when modelling the redshift space distortions around clusters (see for example Weinberg et al. (2013)). However it can be seen in measurements from

the simulations shown in the previous chapter that the galaxy LOS velocity dispersion exhibits a significant variation with scale in the quasi-linear infall region around clusters, and importantly is also not spherically symmetric. In the following work, a model is presented which describes the full scale-dependent velocity dispersion of galaxies around a cluster of given mass, and the predictions compared with results observed from stacked clusters in the simulations. This model will then be combined with galaxy infall predictions in order to provide a complete description of redshift space distortions around clusters.

4.1 Velocity dispersion components

4.1.1 Secondary halos

The approach taken in this work is to individually model the different physical sources which contribute to the overall galaxy velocity dispersion, and combine these to provide a description of this effect along the line of sight. Firstly, the velocity dispersion of infalling secondary halos is examined, as this will translate to an equal velocity dispersion of the galaxy populations they contain. The main component of this velocity dispersion arises from the fact that as the distance from the primary halo increases, the secondary halos are less gravitationally bound and therefore undergoing decreasingly coherent motion relative to the cluster. For secondary halos of a single mass there will consequently be both a radial and tangential velocity dispersion which varies with distance from the cluster centre, and is dependent on the secondary and primary halo masses. A fitting function is presented which describes this velocity dispersion, and the predictions integrated over all secondary halo masses, weighting by galaxy population, in order to obtain a model for their contribution to the total galaxy velocity dispersion.

In addition to the above halo velocity dispersion, there is also an effect which results from the summing of different streaming motions over all secondary halo masses. This acts to increase the velocity dispersion in the radial direction, when compared to the prediction for secondary halos of a single mass. The additional velocity dispersion can be obtained analytically for a given radius by calculating the standard deviation of all halo infall velocity predictions weighted by galaxy population, when performing the integration over secondary halo mass. This extra velocity dispersion is then combined with the radial component of the contribution from halo motions to the overall galaxy velocity dispersion, as described above. The total radial and tangential velocity dispersion predictions are

then used to calculate the galaxy LOS velocity dispersion contributed by secondary halo motions, which is expected to be spherically asymmetric due to the LOS component of the velocity dispersion varying with position relative to the cluster centre.

4.1.2 Galaxy virial motion

In order to provide a full description of the galaxy velocity dispersion we need to examine not only the secondary halo motions, but also the velocity dispersion of galaxies due to their virial motion within these halos. The one dimensional velocity dispersion of galaxies within a parent halo of given mass can be predicted from the virial theorem, and then integrated over all secondary halo masses weighted by galaxy population in order to obtain a model for the LOS velocity dispersion contributed by galaxy virial motions. This will vary with distance from the cluster centre and be dependent on the primary halo mass, and is expected to be spherically symmetric provided that the one dimensional galaxy velocity dispersion in the secondary halos displays no directional dependence. The velocity dispersion which arises from galaxy virial motions can then be combined with the predicted contribution from secondary halo motions described above, in order to provide a complete model for the total galaxy LOS velocity dispersion around a cluster.

4.2 Halo velocity dispersion

4.2.1 Coherence model

The motion of infalling secondary halos relative to the cluster becomes less coherent as the distance from the primary halo increases, which results in a velocity dispersion along both the radial and tangential directions. The following generalised fitting formula is introduced which describes the velocity dispersion $\sigma_v^{\rm sh}$ for secondary halos of a given mass at separation r from the cluster centre:

$$\sigma_v^{\rm sh} = Ar^{\beta} + \frac{r}{r_{coh}} v^{\rm sh}(r) \tag{4.1}$$

where $v^{\rm sh}(r)$ is the mean halo streaming velocity, and the fitted parameters A, β and r_{coh} are all functions of halo mass. The mean streaming motions of secondary halos perpendicular to the line of separation from the cluster centre are negligible on the scales of interest here, and therefore $v_{\perp}^{\rm sh}(r) \approx 0$ to a good approximation which reduces the tangen-

tial velocity dispersion $\sigma_{\perp}^{\rm sh}$ to a simple power law. Measurements from the simulations are then used to fit the parameters A and β for a given primary and secondary halo mass, to obtain the scale dependence for the tangential component of the secondary halo velocity dispersion. This prediction can then be inserted into equation 4.1 to give the following expression for the radial velocity dispersion:

$$\sigma_{r}^{\rm sh} = \sigma_{\perp}^{\rm sh} + \frac{r}{r_{coh}} v_r(r) \tag{4.2}$$

where $v_r(r)$ is provided by the transition model for halo streaming described in the previous chapter. Measurements of the radial velocity dispersion for secondary halos in the simulations are then used to fit the remaining parameter r_{coh}, which represents the scale above which the second term in equation 4.2 exceeds the halo infall velocity. The coherence model can then be used to predict both the radial and tangential components of the secondary halo velocity dispersion as a function of distance from the cluster centre, for a given primary and secondary halo mass.

Figure 4.1 shows the radial and tangential halo velocity dispersion as predicted by the coherence model, compared to results observed from stacked clusters in the simulations. The best fit to the simulation data is shown for various different halo mass bins, with the fitted parameters A, β and r_{coh} stated in each case. The velocity dispersion of secondary halos in the simulations is obtained firstly in the radial direction, and then the θ and ϕ components perpendicular to this are measured and the average used to calculate the tangential velocity dispersion. The halo velocity distribution is assumed to be Gaussian, and therefore the error on the velocity dispersion is approximated as $\sigma_{v}^{\rm sh}\sqrt{1/2(n-1)}$ where n is the halo count in each radial bin. It can be seen from these results that the radial velocity dispersion is significantly higher than the tangential component for secondary halos in the simulations, and that the coherence model provides a good description of both velocity dispersion profiles for the halo mass bins shown. Note that the difference between radial and tangential velocity dispersion is unexpected, but is also seen in Zu & Weinberg (2013). This may be related to halo ellipticities not accounted for in these analyses.

In order to extend the coherence model so that the velocity dispersion can be predicted for any given combination of primary and secondary halo masses, the dependence of parameters A, β and r_{coh} on halo mass needs to be established. To obtain this the

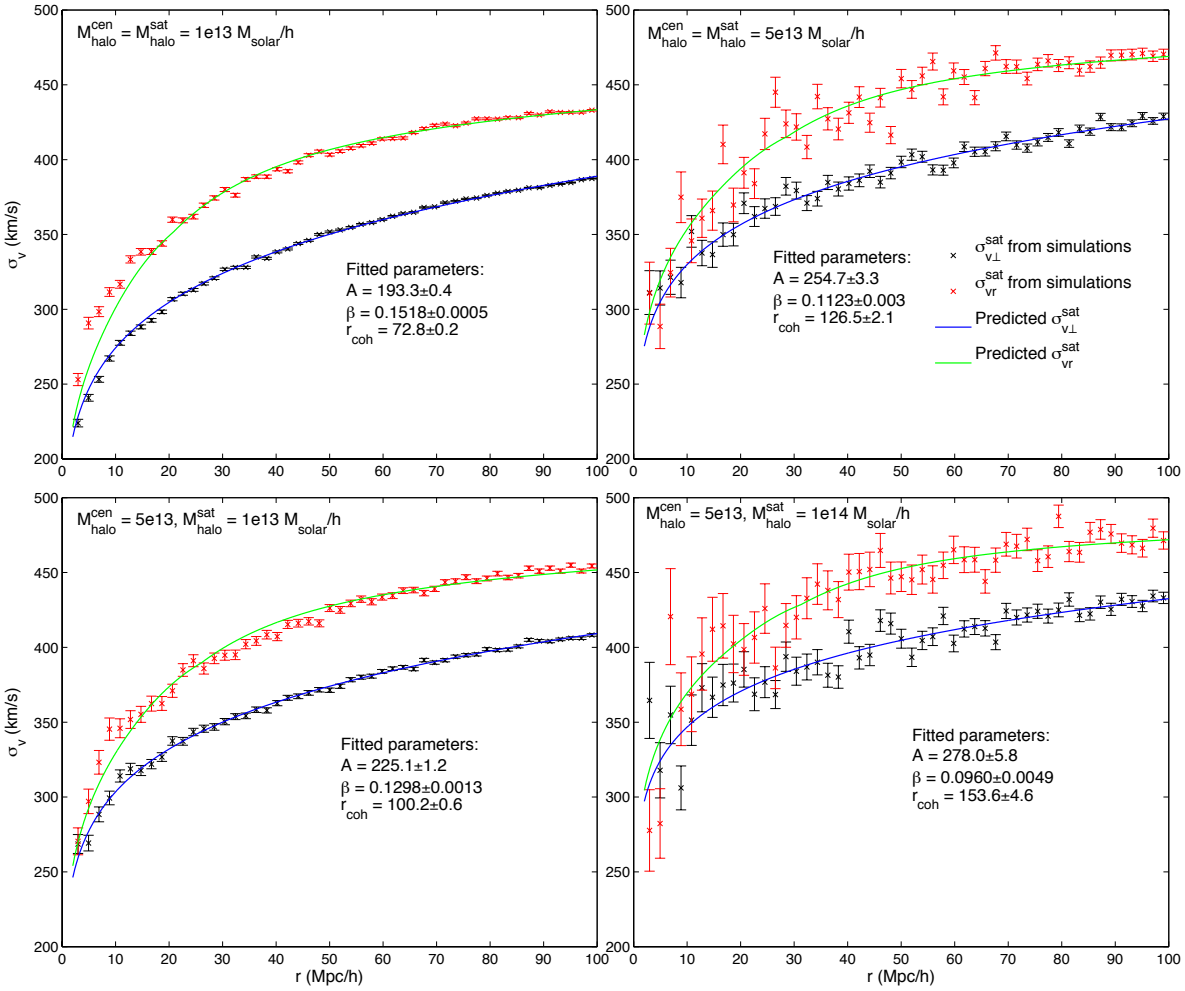

Figure 4.1. Velocity dispersion of secondary halos as a function of distance from the primary halo as predicted by the coherence model, compared to measurements from the simulations. The predicted radial (green line) and tangential (blue line) components of the halo velocity dispersion are shown, with the best fit parameters for the coherence model stated for each different halo mass bin. Red and black crosses show the velocity dispersion measured from the simulations in the radial and tangential directions, respectively. Results are shown for primary and secondary halos with both equal (top) and different (bottom) masses, for two different mass bins in each category. Note that the figure labels $\sigma_{vr}^{\rm sat} = \sigma_r^{\rm sh}$, $\sigma_{v\perp}^{\rm sat} = \sigma_\perp^{\rm sh}$, $M_{\rm halo}^{\rm cen} = M_{\rm ph}$ and $M_{\rm halo}^{\rm sat} = M_{\rm sh}$.

secondary halo velocity dispersion in both the radial and tangential directions was fitted from simulation data for four different primary halo mass bins, performing each fit for a range of individual secondary halo masses. These measurements were then combined to give relations between the coherence model parameters and the average of the primary and secondary halo masses $M_{\rm av}$. Figure 4.2 shows the halo mass dependence of fitted parameters A, β and r_{coh}, including the results for all four primary halo mass bins. There is a clear correlation between average halo mass and all three of the coherence model parameters which is positive for both A and r_{coh}, and negative for β. Assuming either a power law or linear variation with $\log M_{\rm av}$, the below best fit relations are obtained for the coherence model parameters:

$$\begin{aligned} A &= 3.41{M_{\rm av}}^{0.13} \\ \beta &= -0.05 \log M_{\rm av} + 0.78 \\ r_{coh} &= 0.01{M_{\rm av}}^{0.30} \end{aligned}$$

It can be seen from figure 4.2 that the halo mass dependence is reasonably well described by the above expressions, although the coherence model parameter predictions become less accurate with increasing average halo mass. These relations can be used to calculate the parameters A, β and r_{coh} for any given combination of primary and secondary halo masses, and therefore predict both the radial and tangential components of the secondary halo velocity dispersion as a function of distance from the cluster centre.

4.2.2 Additional infall velocity dispersion

Galaxies observed in the infall region around a cluster reside in secondary halos of various different masses, all of which are streaming at varying rates towards the cluster centre. This results in an additional velocity dispersion which acts in the radial direction, and is dependent on distance from the primary halo. The galaxy velocity dispersion $\sigma_r^{\rm infall}$ arising from this effect can be obtained for a given primary halo mass by calculating the standard deviation of all secondary halo velocity profiles from the mean galaxy infall $v_r^{\rm gal}(r)$, using the transition model to predict $v_r^{\rm sh}(r, M_{\rm sh})$ for each halo mass and weighting by their contribution to the galaxy number density $\rho_{gal}(r, M_{\rm sh})$ as follows:

$${\sigma_r^{\rm infall}}^2(r) = \frac{1}{\rho_{gal}^{tot}(r)} \int_0^\infty \rho_{gal}(r, M_{\rm sh}) \left[v_r^{\rm sh}(r, M_{\rm sh}) - v_r^{\rm gal}(r) \right]^2 dM_{\rm sh} \qquad (4.3)$$

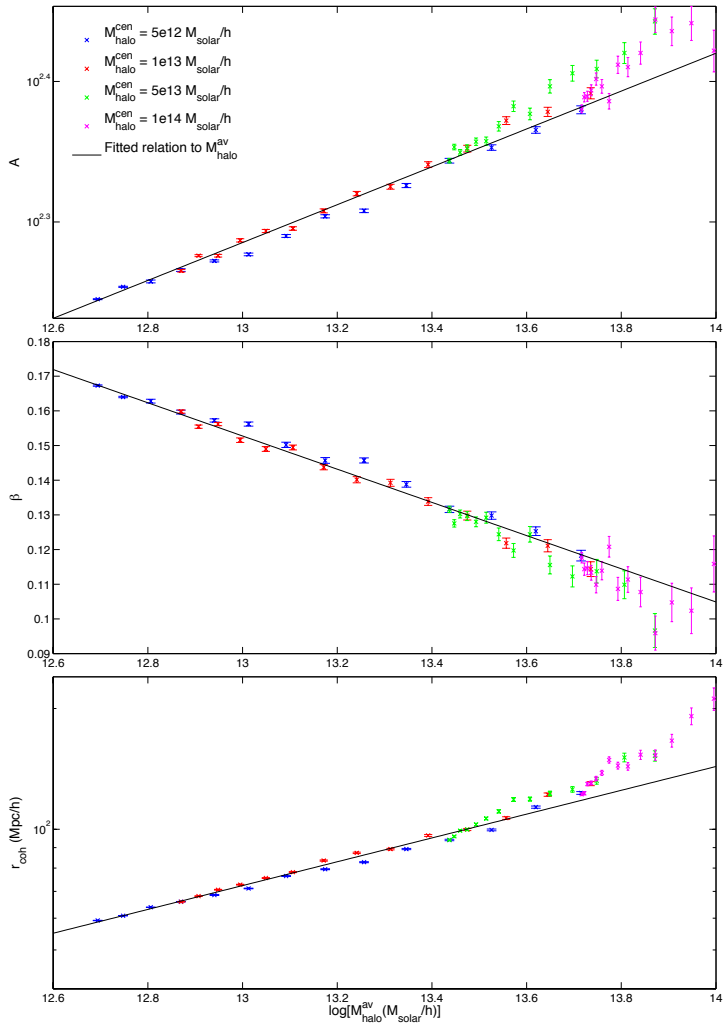

Figure 4.2. Coherence model parameters fitted from N-body simulations, as a function of average halo mass. The parameters A, β and r_{coh} fitted for a range of secondary halo masses are given in the top, middle and bottom panels respectively, with results shown for four different primary halo mass bins centred on 5×10^{12} (blue), 1×10^{13} (red), 5×10^{13} (green) and 1×10^{14} (pink) $\mathrm{M}_{solar} h^{-1}$. Black lines show the best fit dependence on average halo mass for each parameter. Note that the figure labels $M^{\rm cen}_{\rm halo} = M_{\rm ph}$ and $M^{\rm av}_{\rm halo} = M_{\rm av}$.

where $\rho_{gal}^{tot}(r)$ is the total galaxy density profile, as defined in the previous chapter. The integration is performed over the secondary halo mass range $10^{11} \leqslant M_{\rm sh} \leqslant 10^{16}$ M$_{solar}h^{-1}$, which effectively includes all halos with a galaxy population. This provides a description of the radial velocity dispersion for galaxies as a function of distance from the cluster centre, which occurs due to the variation in streaming motions between secondary halos of different masses.

Figure 4.3 shows the radial galaxy velocity dispersion $\sigma_r^{\rm infall}$ which results from integrating the infall velocity profiles over the full range of secondary halo masses, with predictions given for four different primary halo masses. It can be seen that close to the cluster centre there is a significant additional velocity dispersion along the radial direction due to this effect, which drops off with distance as the streaming motions become more uniform between halos of different masses. There is also an increased velocity dispersion near to primary halos with a lower mass when compared to more massive clusters, which are in proximity to higher mass secondary halos that contain a large number of galaxies moving coherently with their parent halo. It can be seen from figure 4.3 that $\sigma_r^{\rm infall}$ decreases rapidly with distance from the cluster centre, in contrast to the velocity dispersion measured for secondary halos of a given mass which is shown in figure 4.1. The mean infall profile for a specified $M_{\rm sh}$ is described by the transition model, and the halo velocity dispersion increases with r as their streaming motions become less coherent. The additional velocity dispersion $\sigma_r^{\rm infall}$ arises due to the variation of infall profiles across different secondary halo masses, which is greater at distances close to the cluster centre. This produces a slight increase in the predicted galaxy velocity dispersion which is significant on small scales, as a result of integrating the streaming motions over all secondary halo masses. This model for $\sigma_r^{\rm infall}$ can be combined with the radial component of secondary halo velocity dispersion predicted by the coherence model, in order to obtain a complete description of the contribution from halo motions to the overall galaxy velocity dispersion around a cluster.

4.2.3 Contribution from halo motions

In this section the coherence model has been introduced, which describes the radial and tangential velocity dispersion for secondary halos of a given mass as a function of distance from the cluster centre. However in order to obtain the galaxy velocity dispersion which results from these halo motions the predictions need to be integrated over all secondary

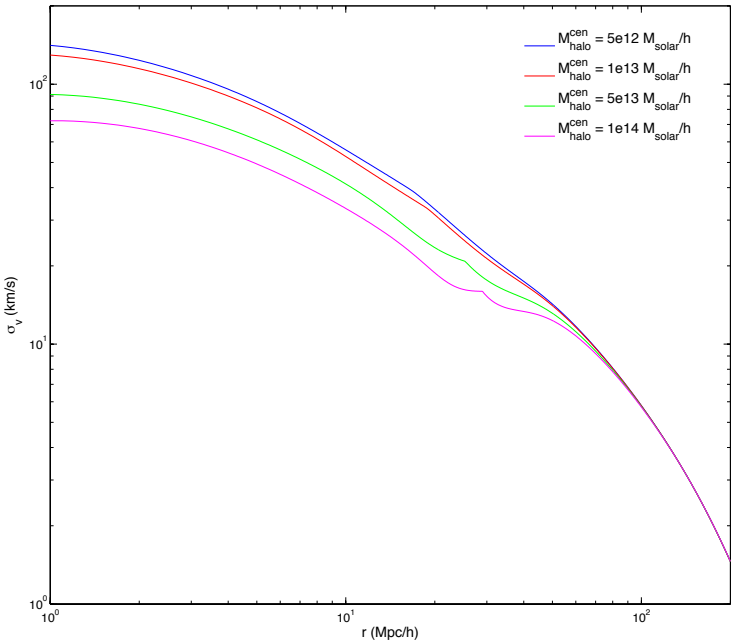

Figure 4.3. Predicted radial galaxy velocity dispersion resulting from the integration of streaming motions over all secondary halo masses, as a function of distance from the primary halo. Predictions are shown for four different primary halo masses: 5×10^{12} (blue), 1×10^{13} (red), 5×10^{13} (green) and 1×10^{14} (pink) $\mathrm{M}_{solar} h^{-1}$. Note that the axis label σ_v represents the radial galaxy velocity dispersion $\sigma_r^{\mathrm{infall}}$, and the figure label $M_{\mathrm{halo}}^{\mathrm{cen}} = M_{\mathrm{ph}}$.

halo masses, weighting by the galaxy number density $\rho_{gal}(r, M_{\mathrm{sh}})$ that each one contributes to the total density profile $\rho_{gal}^{tot}(r)$. The halo velocity distribution is assumed to be Gaussian, and therefore the secondary halo velocity dispersions are combined in quadrature to produce the following expressions for both radial and tangential components of the galaxy velocity dispersion arising from halo motions around a cluster with given primary halo mass:

$$\sigma_{\perp}^{\mathrm{hm}\,2} = \frac{1}{\rho_{gal}^{tot}(r)} \int_0^{\infty} \rho_{gal}(r, M_{\mathrm{sh}}) \sigma_{\perp}^{\mathrm{sh}\,2}(r, M_{\mathrm{sh}}) dM_{\mathrm{sh}} \tag{4.4}$$

$$\sigma_{r}^{\mathrm{hm}\,2} = \sigma_{r}^{\mathrm{infall}\,2}(r) + \frac{1}{\rho_{gal}^{tot}(r)} \int_0^{\infty} \rho_{gal}(r, M_{\mathrm{sh}}) \sigma_{r}^{\mathrm{sh}\,2}(r, M_{\mathrm{sh}}) dM_{\mathrm{sh}} \tag{4.5}$$

where the coherence model parameters are calculated for each secondary halo mass M_{sh} from the best fit relations derived above, and used to obtain the corresponding velocity dispersion profiles $\sigma_{\perp}^{\mathrm{sh}}$ and σ_r^{sh}. In the case of the radial component this is then combined with the additional galaxy velocity dispersion $\sigma_r^{\mathrm{infall}}$, in order to account for the variation

in mean infall velocity across secondary halos of different masses. The integrals in these expressions are evaluated by summing over the same mass range of $10^{11} \leqslant M_{\rm sh} \leqslant 10^{16}$ $\mathrm{M}_{solar}h^{-1}$ that was used earlier, and the galaxy density profiles are calculated as described in the previous chapter. This provides a complete model for the contribution from halo motions to the overall galaxy velocity dispersion, and how its components along both the radial and tangential directions vary with distance from the cluster centre.

Figure 4.4 shows the halo velocity dispersion predicted by equations 4.4 and 4.5 for four different primary halo masses, with the radial component given both with and without the inclusion of the additional infall velocity dispersion term $\sigma_r^{\rm infall^2}(r)$. This is compared to measurements from stacked clusters in the simulations, where the velocity of each secondary halo is weighted by the number of galaxies it contains. It can be seen that the tangential velocity dispersion is reasonably well described by the coherence model, although for the larger primary halo masses $\sigma_\perp^{\rm hm}$ is under-predicted on small scales. This is most likely due to the assumption of $v_\perp^{\rm sh}(r) \approx 0$ being invalid near to the centre of massive clusters, which has the potential to increase the expected velocity dispersion. In the radial direction the predicted velocity dispersion is also in relatively good agreement with results from the simulations on large scales, but is seen to drop off further from the cluster centre for low mass primary halos when using the coherence model alone. The addition of the infall velocity dispersion $\sigma_r^{\rm infall}$ improves this to a certain extent, however the combined prediction for $\sigma_r^{\rm hm}$ is still lower than that observed in the simulations at distances close to the cluster centre. There is an increased deviation for lower mass primary halos which have a higher proportion of their radial velocity dispersion contributed from $\sigma_r^{\rm infall}$ compared to more massive clusters, which implies that this quantity is being underestimated, possibly due to a non-Gaussian distribution of the mean streaming motions for secondary halos with different masses.

The effects described above, which result in a lower predicted radial and tangential velocity dispersion around clusters with small and large primary halo masses respectively, act on scales below ~ 15 Mpch^{-1} and also produce only a relatively slight decrease in the total secondary halo velocity dispersion when compared to results from the simulations. The coherence model presented here, combined with the description provided for the additional infall velocity dispersion, can therefore be used to predict with reasonably good accuracy the contribution from halo motions to the overall galaxy velocity dispersion around a primary halo of given mass, as a function of distance from the cluster centre.

The resultant velocity dispersion along the line of sight can be calculated from the radial and tangential components as follows:

$$\sigma_{\rm los}^{\rm hm\,2} = \sigma_r^{\rm hm\,2} \cos^2\phi + \sigma_\perp^{\rm hm\,2} \sin^2\phi \tag{4.6}$$

where ϕ is the angle between the LOS and position vector from the primary halo. The above expression can be used to obtain the two dimensional LOS velocity dispersion for secondary halos $\sigma_{\rm los}^{\rm hm}$, as a function of projected distance on the sky r_σ and LOS separation r_π relative to the cluster centre.

Figure 4.5 shows the predicted contribution from secondary halo motions to the total galaxy LOS velocity dispersion around clusters with four different primary halo masses, calculated using the coherence model combined with the expected additional infall velocity dispersion. The predictions are given as a function of two dimensional position r_π, r_σ relative to the cluster centre, with the LOS velocity dispersion obtained from the radial and tangential components using equation 4.6. It can be seen that this velocity dispersion resulting from halo motions is spherically asymmetric, with $\sigma_{\rm los}^{\rm hm}$ increasing more rapidly with distance along the LOS compared to the r_σ direction. This is due to the radial velocity dispersion being greater than the tangential component for secondary halos, and is similar to the asymmetry observed in measurements of the galaxy LOS velocity dispersion around stacked clusters from the simulations shown in the previous chapter. The model introduced in this section provides a description of halo velocity dispersion in the infall region around clusters, and can be combined with a model for galaxy virial motions within these halos in order to predict the overall galaxy velocity dispersion around a cluster of given primary halo mass.

4.3 Velocity dispersion within halos

4.3.1 Virial model

In the previous section a model for secondary halo velocity dispersion was presented, however in order to provide a complete description of this effect for galaxies around a cluster we need to examine their virial motion within these halos. The one dimensional velocity dispersion $\sigma_{\rm 1d}$ in a halo varies with distance r from the centre according to the

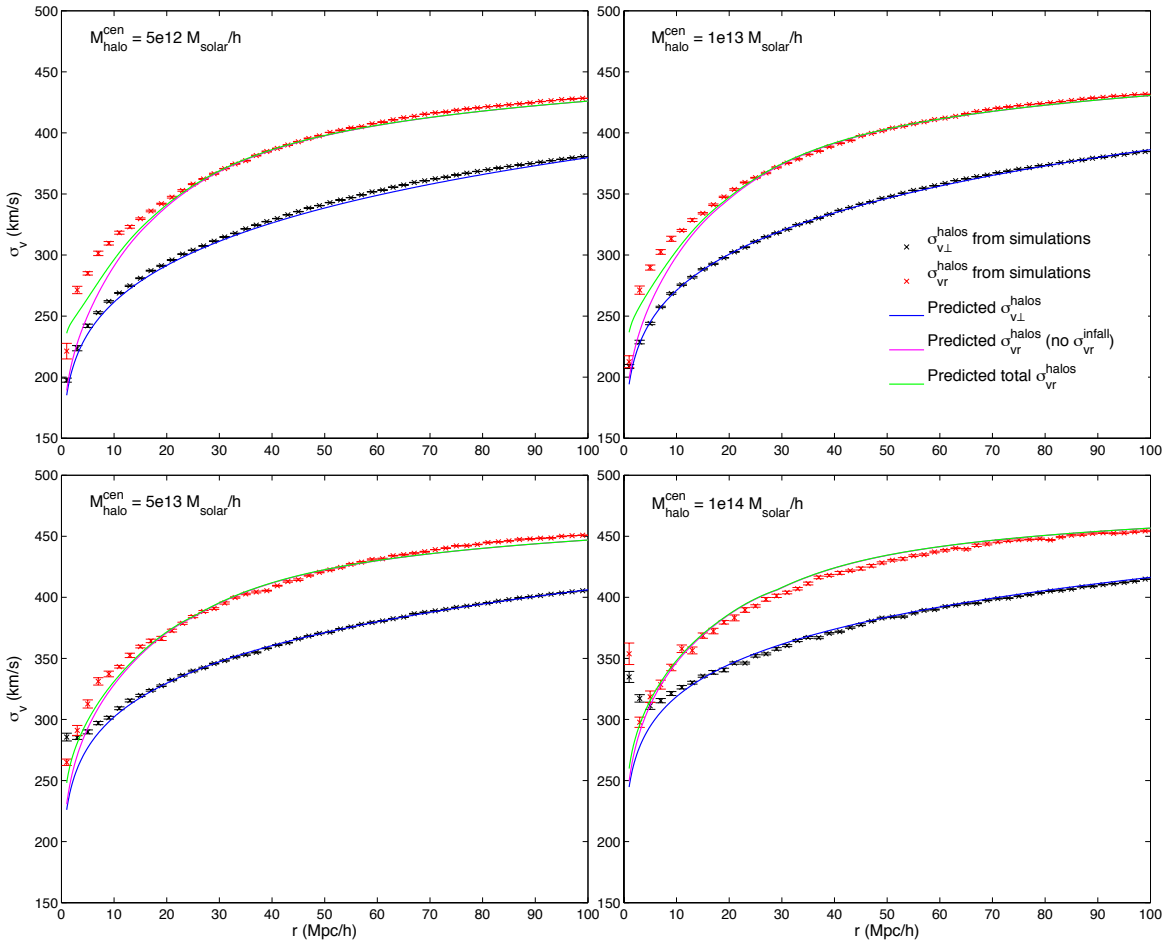

Figure 4.4. Halo velocity dispersion integrated over all secondary halo masses weighted by galaxy population, as a function of distance from the primary halo. Measurements from the simulations of halo velocity dispersion in the radial and tangential directions, shown by red and black crosses respectively, are compared to predictions calculated using the coherence model. The predicted tangential component of the halo velocity dispersion is shown by the blue line, and the radial component predictions both with and without the inclusion of the additional infall velocity dispersion which results from integrating over all secondary halo masses (shown in figure 4.3) are shown by the green and pink lines, respectively. Results are shown for four different primary halo mass bins, centred on (from top left to bottom right) 5×10^{12}, 1×10^{13}, 5×10^{13} and 1×10^{14} M$_{solar}h^{-1}$. Note that the figure labels $\sigma_{vr}^{\rm halos} = \sigma_r^{\rm hm}$, $\sigma_{v\perp}^{\rm halos} = \sigma_\perp^{\rm hm}$, $\sigma_{vr}^{\rm infall} = \sigma_r^{\rm infall}$ and $M_{\rm halo}^{\rm cen} = M_{\rm ph}$.

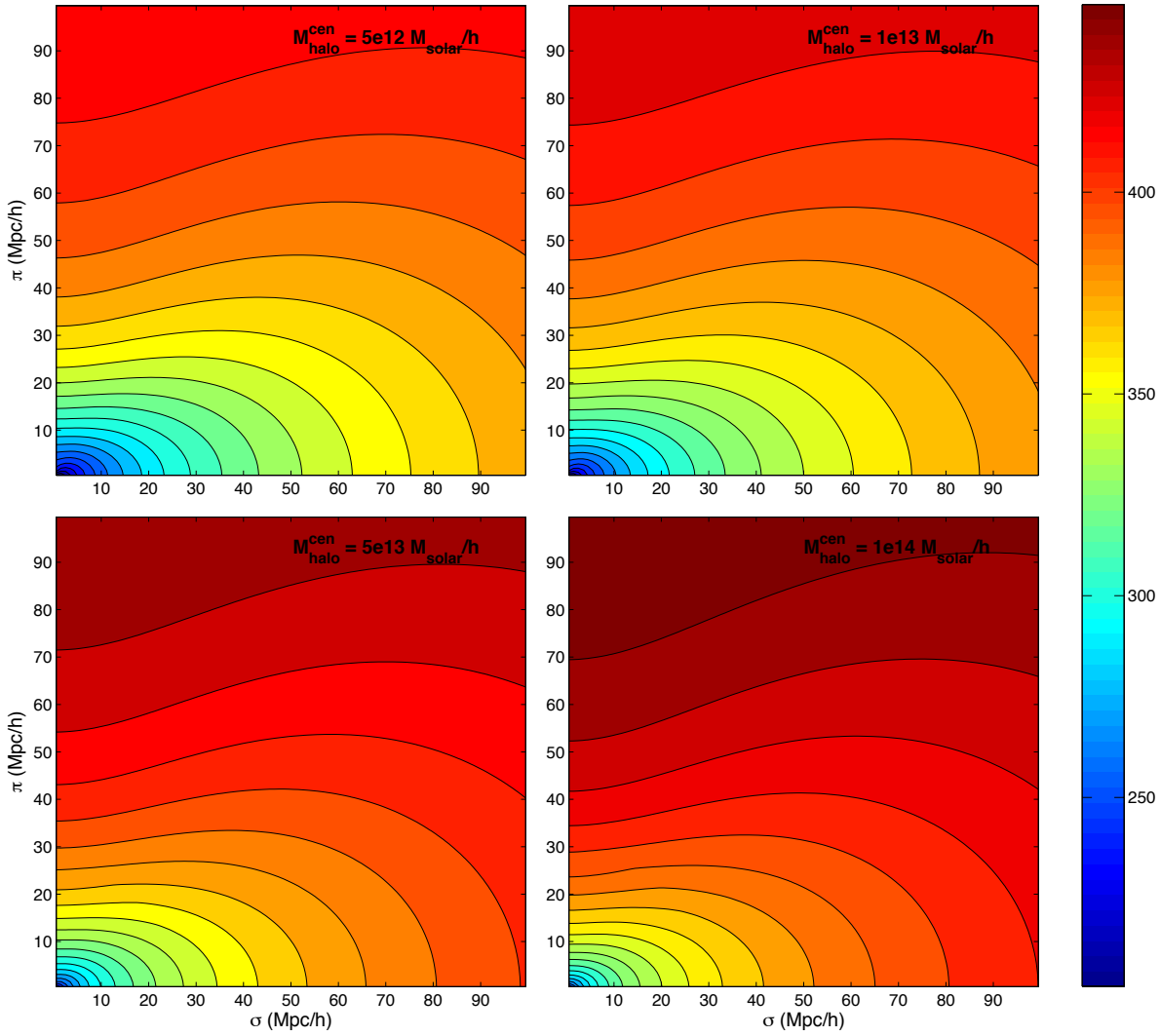

Figure 4.5. Predicted halo velocity dispersion along the line of sight, integrated over all secondary halo masses weighted by galaxy population, as a function of position relative to the cluster centre. Predictions calculated using the coherence model are shown for four different primary halo masses (from top left to bottom right): 5×10^{12}, 1×10^{13}, 5×10^{13} and 1×10^{14} $\mathrm{M}_{solar} h^{-1}$. The colour bar represents the line of sight velocity dispersion in units of km/s, and the figure labels $\pi = r_\pi$, $\sigma = r_\sigma$ and $M^{\mathrm{cen}}_{\mathrm{halo}} = M_{\mathrm{ph}}$.

virial theorem as follows:

$$\sigma_{\rm 1d} \approx \sqrt{\frac{GM_{enc}(r)}{3r}} \tag{4.7}$$

where M_{enc} is the mass enclosed within radius r, and the factor of 3 is included to give the velocity dispersion along a single direction. The above expression is evaluated using M_{enc} for an NFW profile which describes the dark matter density ρ_{dm} as a function of r (Navarro et al. (1996)):

$$\rho_{dm} = \frac{\rho_0}{\left(\frac{r}{R_s}\right)\left(1+\frac{r}{R_s}\right)^2} \tag{4.8}$$

where ρ_0 and the scale radius R_s are related to the mean background density and the halo virial mass M_{200} via the concentration parameter c_h, which is obtained from the below equation from Mandelbaum et al. (2008):

$$c_h = \frac{c_0}{1+z}\left(\frac{M_{200}}{M_0}\right)^{-\beta} \tag{4.9}$$

with the normalisation parameters taken as $c_0 = 5.5$, $M_0 = 1\times10^{14}\ \mathrm{M}_{solar}h^{-1}$ and $\beta = 0.1$ for this cosmological model. Using this definition for M_{enc}, the radial dependence of velocity dispersion due to virial motion can be calculated for a halo of any given mass. The total velocity dispersion $\sigma^{\rm h}_{\rm 1d}$ observed for galaxies populating a single halo can therefore be obtained by integrating over r out to the virial radius R_{200}, combining the different velocity dispersions in quadrature and weighting by the halo mass fraction in each individual shell as follows:

$${\sigma^{\rm h}_{\rm 1d}}^2 = \frac{4\pi}{M_{200}}\int_0^{R_{200}} r^2\rho_{dm}\sigma^2_{\rm 1d}dr \tag{4.10}$$

where the density profile ρ_{dm} is given in equation 4.8.

The above method allows the total galaxy velocity dispersion to be calculated within a halo of given mass, assuming that the galaxy distribution exactly traces that of the dark matter. In practice however, the most gravitationally bound DM particle is always selected as the central galaxy when populating the halos, and therefore in the case of low mass halos containing only one centrally located galaxy there will effectively be zero observed velocity dispersion. This can be accounted for by multiplying equation 4.10 by the fraction

of halos f_{sat} expected to contain satellite galaxies (i.e. have a population greater than one), in order to obtain a statistical approximation of the galaxy velocity dispersion averaged over several halos of a given mass. Since the number of galaxies populating an individual halo is assumed to follow a Poisson distribution about the expected value $\langle N_{\rm gal}(M_{200})\rangle$, the halo fraction containing satellite galaxies is given by:

$$f_{sat}(M_{200}) = 1 - \frac{\langle N_{\rm gal}\rangle e^{-\langle N_{\rm gal}\rangle}}{1 - e^{-\langle N_{\rm gal}\rangle}} \tag{4.11}$$

For very massive halos $f_{sat} \approx 1$, however for small and medium size halos this factor acts to significantly lower the predicted galaxy velocity dispersion. It is therefore important to include f_{sat} in order to accurately describe the total velocity dispersion for galaxies within a halo of given mass which occurs due to their virial motion.

4.3.2 One dimensional velocity dispersion

The virial model described above provides a method of predicting the mean galaxy velocity dispersion for parent halos of a single mass, and can therefore be used to calculate the contribution from secondary halos of different masses to the LOS velocity dispersion around a cluster arising from galaxy virial motion. This quantity is scale independent for halos of a given mass, however when the velocity dispersions are combined for all secondary halos this leads to a dependence on distance from the cluster centre due to the varying distribution of halo masses. In order to obtain the contribution from galaxy virial motion to the overall velocity dispersion around a cluster with given primary halo mass, the predictions from the virial model need to be integrated over the full range of secondary halo masses weighting by the galaxy density profile $\rho_{gal}(r, M_{\rm sh})$ as described in the previous section. This produces the following expression for the one dimensional galaxy velocity dispersion $\sigma_{\rm 1d}^{\rm vir}$ as a function of distance from the primary halo:

$$\sigma_{\rm 1d}^{\rm vir\,2} = \frac{1}{\rho_{gal}^{tot}(r)} \int_0^\infty \rho_{gal}(r, M_{\rm sh}) \left[f_{sat}(M_{\rm sh}) \sigma_{\rm 1d}^{\rm h}(M_{\rm sh}) \right]^2 dM_{\rm sh} \tag{4.12}$$

where the total galaxy density $\rho_{gal}^{tot}(r)$ was defined earlier, and the integral is evaluated over the same halo mass range as was used previously to calculate the coherence model predictions. The above expression describes the velocity dispersion observed in any single direction, and therefore provides a complete model for the LOS velocity dispersion

resulting from galaxy virial motion within secondary halos around a cluster.

The left panel in figure 4.6 shows the one dimensional velocity dispersion $f_{sat}\sigma^{\rm h}_{\rm 1d}$ for galaxies contained in a parent halo of mass $M_{\rm par}$, as predicted by the virial model. This is compared with results from the simulations, which are obtained by stacking individual halos for a given mass and measuring the standard deviation of galaxy velocities taken relative to the parent halo. It can be seen that the virial model provides a reasonably good description of the velocity dispersion observed in halos from the simulations, although slightly underestimates this effect for lower masses and also over-predicts the velocity dispersion in more massive halos. However when these predictions are translated into the full galaxy velocity dispersion by integrating over all secondary halo masses around a cluster, and compared to the outcome obtained using the relation for $\sigma^{\rm h}_{\rm 1d}(M_{\rm par})$ measured directly from the simulations, the difference between the resulting velocity dispersion profiles is at most ~ 2 kms^{-1}. The inaccuracies in the virial model can therefore be considered negligible for the purposes required here, although this could potentially be improved with a more detailed examination of halo density within the virial radius including possible variation in the concentration parameter.

The right panel shows the galaxy velocity dispersion profile predicted by equation 4.12, for clusters with four different primary halo masses. It can be seen that $\sigma^{\rm vir}_{\rm 1d}$ is higher for more massive primary halos on small scales, as they are more likely to be in proximity to other large mass halos. The velocity dispersion in each case drops off with distance from the cluster centre, eventually all converging at $r \sim 100$ Mpch^{-1} where there is no longer any significant difference in the distribution of secondary halo masses. The virial model provides the one dimensional velocity dispersion along any given direction, and therefore the results shown in figure 4.6 equate to a prediction of the LOS effect observed around a cluster. The method described in this section allows the contribution from galaxy virial motion to the total LOS velocity dispersion around a cluster to be calculated for a given primary halo mass, as a function of distance from the cluster centre. Assuming that $\sigma^{\rm h}_{\rm 1d}$ shows no directional dependence in secondary halos around a cluster, the galaxy LOS velocity dispersion at position r_π, r_σ is then obtained directly from the radial profile by applying spherical symmetry. The predicted $\sigma^{\rm vir}_{\rm 1d}(r_\pi, r_\sigma)$ which arises from galaxy virial motion can be combined with the model for secondary halo velocity dispersion introduced in the previous section, in order to provide a complete description for the overall LOS velocity dispersion of galaxies in the infall region around a cluster.

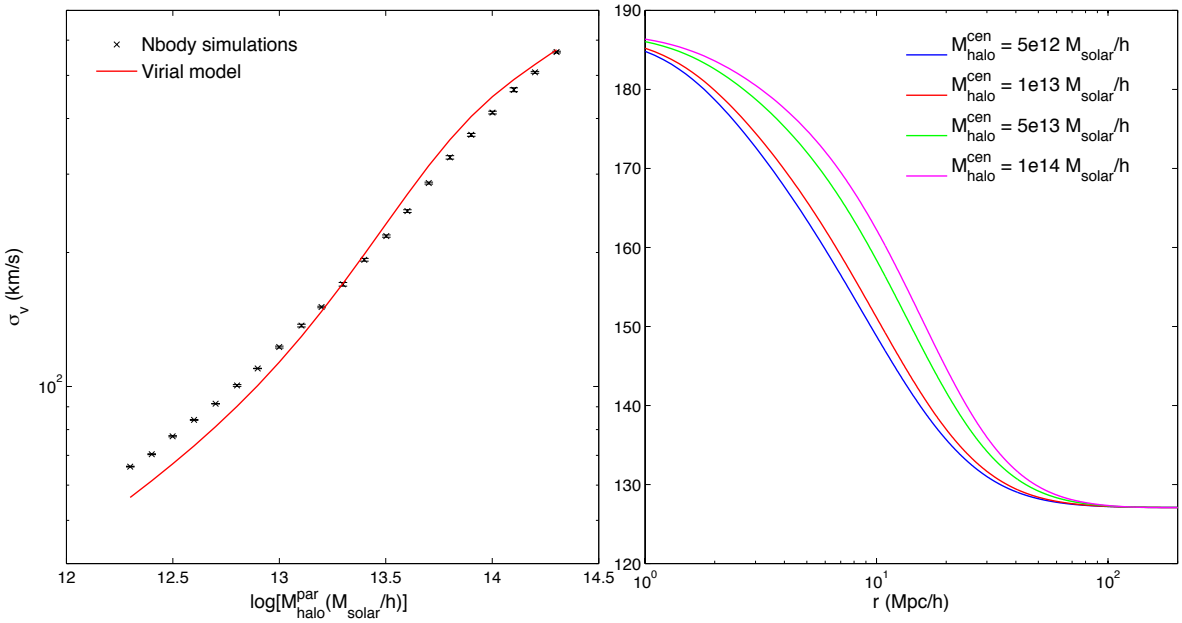

Figure 4.6. Left panel shows the one dimensional velocity dispersion of galaxies populating a single halo which results from their virial motion, as a function of parent halo mass. Measurements from the simulations of galaxy velocity dispersion taken relative to the parent halo are shown for a range of different halo masses (black crosses), and compared to predictions from the virial model (red line). Right panel shows the predicted one dimensional velocity dispersion of galaxies resulting from the virial motion within their parent halos, integrated over all secondary halo masses weighted by galaxy population, as a function of distance from the cluster centre. Predictions calculated using the virial model are shown for four different primary halo masses: 5×10^{12} (blue), 1×10^{13} (red), 5×10^{13} (green) and 1×10^{14} (pink) $\mathrm{M}_{solar}h^{-1}$. Note that the figure labels $M^{\rm cen}_{\rm halo} = M_{\rm ph}$ and $M^{\rm par}_{\rm halo} = M_{\rm par}$.

4.4 Combined velocity dispersion

4.4.1 Component velocity distributions

In this work a model for the velocity dispersion around a cluster which occurs due to secondary halo motions has been presented, and the effect of galaxy virial motion within these halos has also been described. In order to obtain a full model for the resulting galaxy velocity dispersion we need to combine the contributions from these different physical sources, both of which have a significant effect on galaxy dynamics in the infall region around a primary halo. In previous instances where the summing of velocity dispersions was required they have been combined in quadrature, therefore assuming a Gaussian velocity distribution in each case. Here the validity of this assumption will be tested by

examining both halo and galaxy velocity distributions measured from stacked clusters in the simulations, to determine the method by which their contributions to the total galaxy velocity dispersion should be combined.

Figure 4.7 shows the distribution of halo velocities observed in the radial and both tangential directions, at a distance of 20 Mpch^{-1} from the centre of stacked clusters in the simulations for four different primary halo mass bins. The r, θ and ϕ velocity components are measured for secondary halos (inclusive of all masses) in the specified radial bin of width 1 Mpch^{-1}, and the obtained velocity distribution expressed in terms of halo fraction out of the total bin count. It can be seen that the distributions appear Gaussian for the tangential velocity components, with the width increasing for larger primary halo masses which are expected to have a higher secondary halo velocity dispersion at a given radius. The radial velocity distributions appear slightly skewed towards the direction of infall, which is possibly due to the proximity of the cluster centre. A non-skewed distribution is expected for the θ and ϕ velocity components by symmetry, however these could potentially have kurtosis. The velocity distributions in both tangential directions peak at zero for all primary halo masses at this distance from the cluster centre, which is in agreement with the assumption that $v_{\perp}^{\rm sh}(r) \approx 0$ as stated in section 4.2. The radial velocity distributions have a greater width when compared to those measured for the tangential components, which is consistent with the coherence model predictions described previously. The peaks of these distributions are located at increasing values of $v_r^{\rm sh}$ for higher mass primary halos, as the mean infall velocity is larger at a given scale for more massive clusters. In this work the distributions of all halo velocity components are approximated as Gaussian which may bias the constraints on cluster masses, and would not provide a sufficiently detailed model if higher order correlations of the velocity field were being considered beyond the cross-correlation studied here.

Figure 4.8 shows the distribution of galaxy velocities taken relative to their parent halo in the x, y and z directions, as measured from stacked individual halos in the simulations for four different mass bins. The observed velocity distributions are expressed in terms of galaxy fraction out of the total count, which is equal to the sum of galaxy populations from parent halos in the given mass bin. It can be seen that in all cases the galaxy velocity distributions appear approximately Gaussian although have an additional spike in the velocity bin centred on zero; this occurs due to the preferential selection of a central galaxy when populating the simulations, which will have roughly the same velocity as

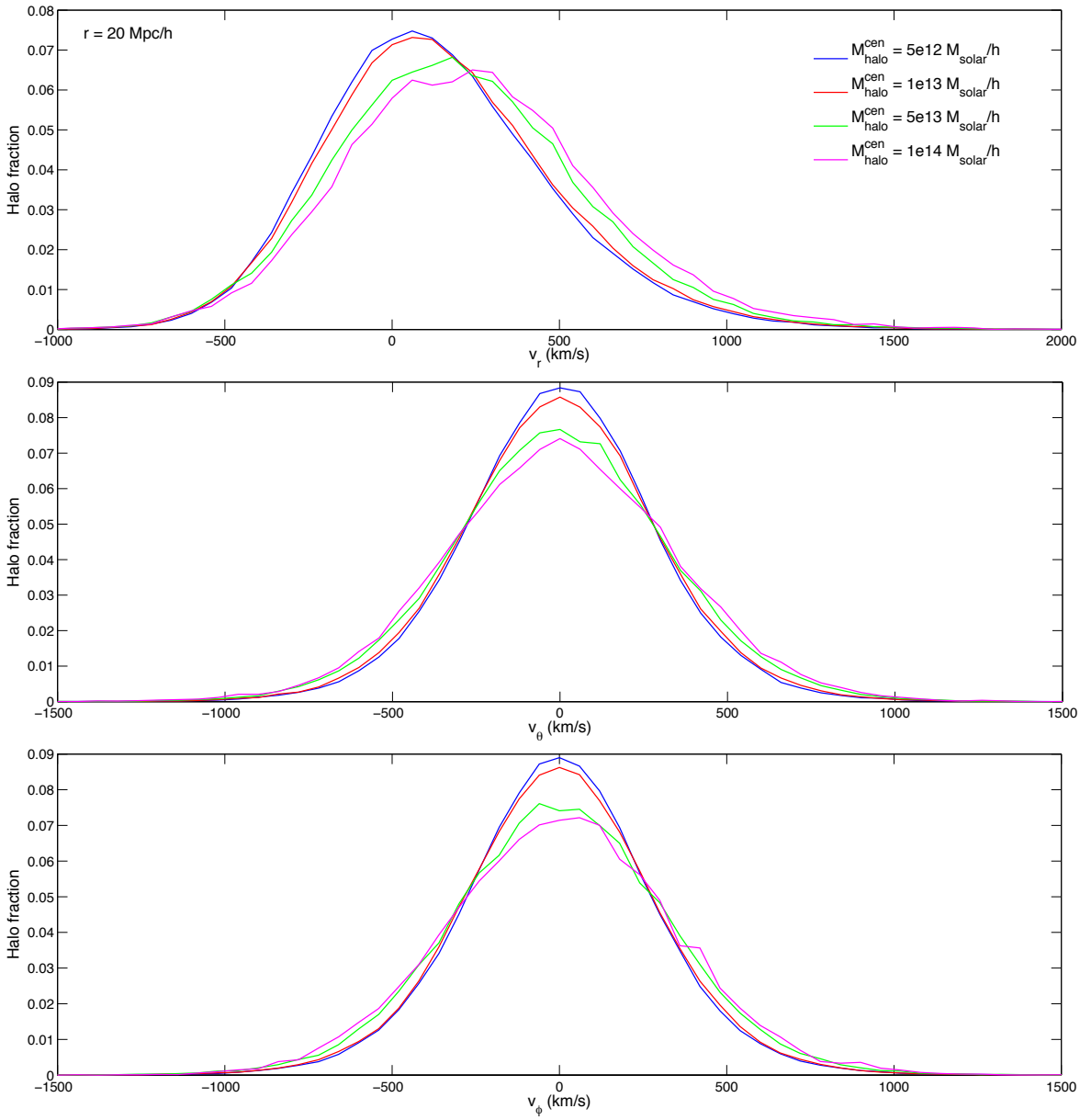

Figure 4.7. Histogram of halo velocities in stacked clusters from the simulations, for all secondary halos contained in a radial bin of width 1 Mpch^{-1} at a distance of 20 Mpch^{-1} from the cluster centre. The distribution of halo velocities in the radial (top) and both tangential (middle and bottom) directions is shown for clusters of different masses, with the fraction of halos given as a function of velocity in each case. Results are shown for four different primary halo mass bins centred on 5×10^{12} (blue), 1×10^{13} (red), 5×10^{13} (green) and 1×10^{14} (pink) M$_{solar}h^{-1}$. Note that the figure label $M^{\rm cen}_{\rm halo} = M_{\rm ph}$.

that of its parent halo. This spike becomes more prominent for lower halo masses, where the central galaxy makes up a higher proportion of the total population. The width of the velocity distributions increases with parent halo mass, which is consistent with model predictions for the velocity dispersion arising from galaxy virial motion within a halo. The distributions of all three velocity components are extremely similar for each parent halo mass, which supports the assumption made earlier that the one dimensional velocity dispersion of galaxies in a halo does not vary significantly with direction.

4.4.2 Total galaxy velocity dispersion

It has been shown above that the velocity distributions for both secondary halos and galaxies within those halos can be described as Gaussian to a good approximation, and that therefore the contributions from their motion should be combined in quadrature to give the overall galaxy velocity dispersion around a cluster. A description for the LOS component of the contribution from secondary halo motions $\sigma_{\rm los}^{\rm hm}$ has been provided by the coherence model, and is combined with the predicted one dimensional effect resulting from galaxy virial motion $\sigma_{\rm 1d}^{\rm vir}$ to give the following expression for the total galaxy LOS velocity dispersion $\sigma_{\rm los}^{\rm gal}$ as a function of position relative to the cluster centre:

$$\sigma_{\rm los}^{\rm gal\,2}(r_\pi, r_\sigma) = \sigma_{\rm los}^{\rm hm\,2}(r_\pi, r_\sigma) + \sigma_{\rm 1d}^{\rm vir\,2}(r_\pi, r_\sigma) \tag{4.13}$$

This provides a complete model for galaxy velocity dispersion in the infall region around a cluster, allowing the LOS effect to be calculated at position r_π, r_σ for any given primary halo mass.

Figure 4.9 shows the galaxy velocity dispersion predicted along the LOS by equation 4.13, for clusters with four different primary halo masses. This is compared to observations from stacked clusters in the simulations, obtained by measuring the LOS velocity component for each galaxy and then evaluating their standard deviation as a function of two dimensional position r_π, r_σ relative to the primary halo. In order to reduce noise in the simulations this calculation was repeated taking the LOS along each of the x, y and z directions, and the average of these measurements obtained to give the resultant galaxy velocity dispersion. It can be seen that the model presented here provides a good description of the observed velocity dispersion, reproducing both the scale dependence and spherical asymmetry seen in stacked clusters from the simulations. It has been demonstrated that

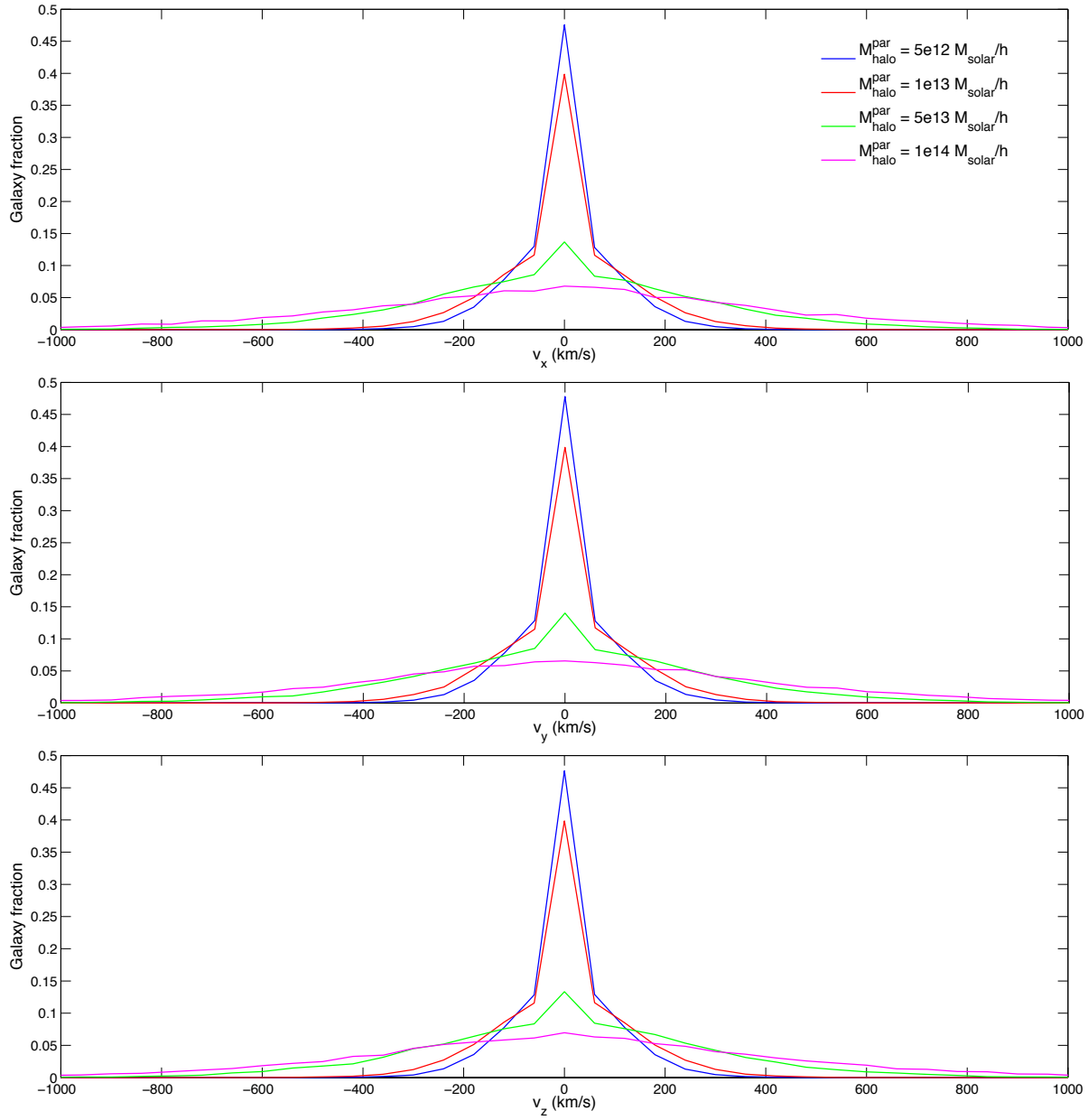

Figure 4.8. Histogram of galaxy velocities in stacked single halo populations from the simulations, with the velocities taken relative to the parent halo. The distribution of galaxy velocities in the x, y and z (from top to bottom) directions is shown for parent halos of different masses, with the fraction of galaxies given as a function of velocity in each case. Results are shown for four different parent halo mass bins centred on 5×10^{12} (blue), 1×10^{13} (red), 5×10^{13} (green) and 1×10^{14} (pink) $\mathrm{M}_{solar} h^{-1}$. Note that the figure label $M^{\mathrm{par}}_{\mathrm{halo}} = M_{\mathrm{par}}$.

the galaxy velocity distribution is expected to be Gaussian, and therefore the application of this as a convolution should give an accurate method for modelling the effect of LOS velocity dispersion on the galaxy distribution in redshift space around a cluster.

4.5 Conclusions

In this chapter a model has been presented which describes galaxy velocity dispersion in the infall region around clusters, and how this effect varies with position relative to the primary halo. The approach taken has been to develop methods for individually modelling the contributions from both secondary halo dynamics and the galaxy virial motion within these halos, and then combine the predictions to provide a complete description of the total galaxy velocity dispersion. This model could then be used to calculate the line of sight component of this effect around a cluster with given primary halo mass, as a function of two dimensional position r_π, r_σ relative to the cluster centre. Comparison with simulations demonstrated a good agreement between these predictions and the observed galaxy LOS velocity dispersion, with the model providing an accurate description of the spherically asymmetric variation of this effect with scale. It was shown that the predicted velocity dispersion could be applied to the galaxy distribution in redshift space in the form of a Gaussian convolution, and therefore when combined with the transition model for galaxy infall will provide a full description of the redshift space distortions around a cluster.

The model discussed above could be potentially improved by examining a number of factors in more detail, which are left as future work. Firstly, the inclusion in the coherence model of a description for the mean halo tangential velocity $v_\perp^{\rm sh}(r)$, which may not be negligible in the most massive clusters on small scales. The halo mass dependence of the coherence model parameters is also less accurate for large masses, and it would therefore be useful to investigate alternative forms to the power law or linear variation with $\log M_{\rm av}$ which is assumed here. In addition to this, comparison with simulations suggested that the contribution from the halo infall velocity dispersion $\sigma_r^{\rm infall}$ was being underestimated, possibly due to a non-Gaussian distribution of secondary halo velocities close to the cluster centre. It would be helpful to examine the halo velocity distributions for both the radial and tangential components at a range of distances from the primary halo, to expand on the results for a single radial bin at 20 Mpch^{-1} shown in figure 4.7.

For the galaxy virial model, predictions of the one dimensional velocity dispersion

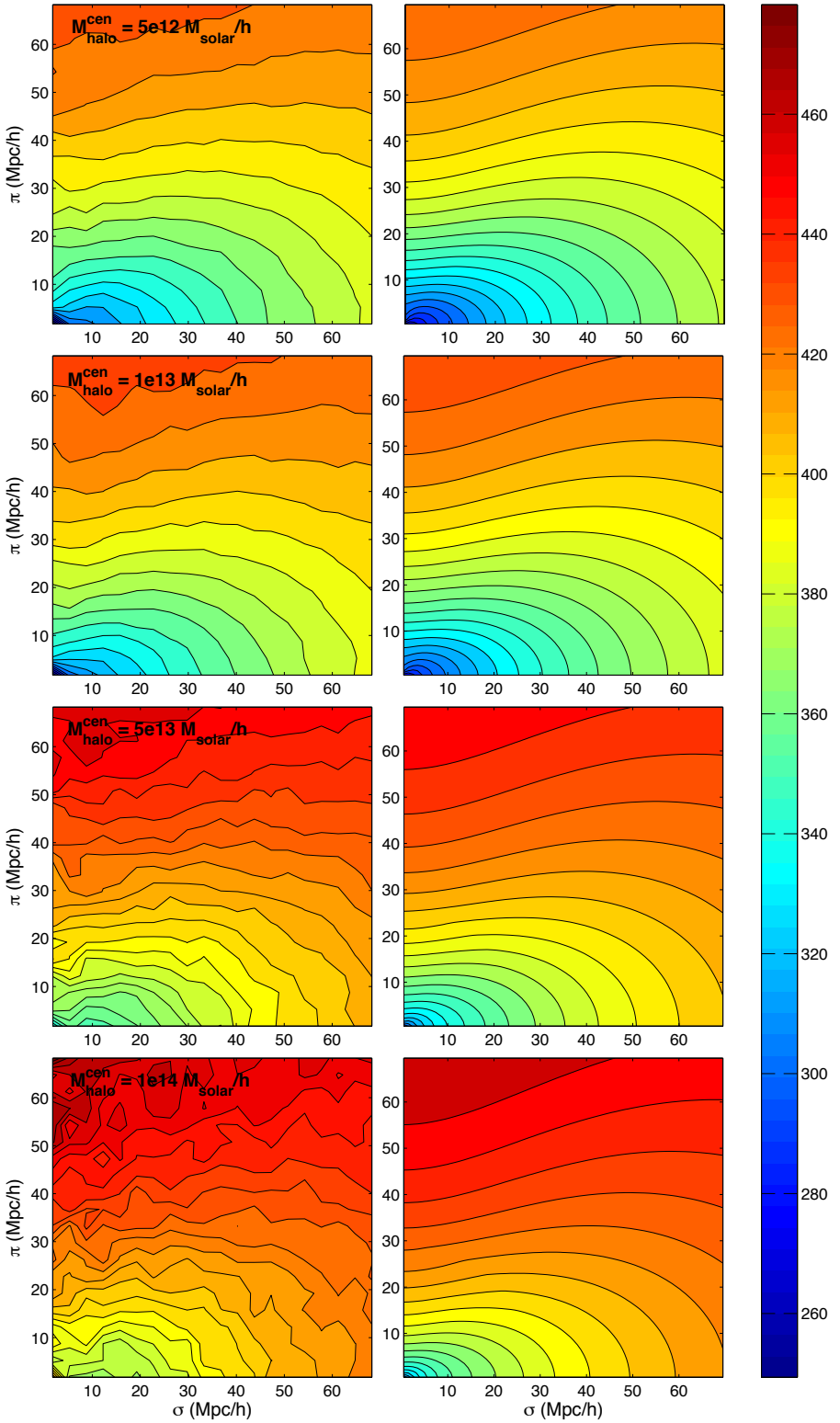

Figure 4.9. Galaxy velocity dispersion along the line of sight, as a function of position relative to the cluster centre. Measurements from stacked clusters in the simulations (left panels) are compared to predictions calculated by combining the halo and galaxy velocity dispersion models to give the resulting line of sight velocity dispersion for galaxies around the cluster (right panels). Results are shown for four different primary halo mass bins, centred on (from top to bottom) 5×10^{12}, 1×10^{13}, 5×10^{13} and 1×10^{14} $\mathrm{M}_{solar} h^{-1}$. The colour bar represents the line of sight velocity dispersion in units of km/s, and the figure labels $\pi = r_\pi$, $\sigma = r_\sigma$ and $M^{\mathrm{cen}}_{\mathrm{halo}} = M_{\mathrm{ph}}$.

within a parent halo of given mass are slightly inaccurate at both very low and high masses when compared to the simulations, and this could potentially be improved by including a more detailed description of halo density inside the virial radius with possible variation in the concentration parameter. It would also be useful to explore further the assumption that this galaxy velocity dispersion displays no directional dependence for secondary halos around a cluster, by examining both the radial and tangential galaxy velocity distributions within halos at a given distance from the cluster centre. The observed velocity distribution deviates from a Gaussian for lower parent halo masses due to the additional spike at zero which arises from the preferential selection of a central galaxy when populating the simulations, and it would therefore be helpful to establish a method for including this feature when combining the galaxy velocity dispersion with the effect contributed by secondary halo motions. Finally, as the predictions for all of the components which contribute to the overall galaxy LOS velocity dispersion around a cluster have only been compared with simulations at a single redshift, it would be essential to investigate the potential dependence of the model on this factor in order to apply it generally to galaxy redshift survey data.

Chapter 5

Constraining Cluster Mass from the Cosmic Onion

The infall and velocity dispersion of galaxies around a cluster both provide a useful probe of the primary halo mass, although neither of these can be measured directly from galaxy survey data. In practice, the observable quantity is redshift which translates to a galaxy position, and in the absence of any peculiar velocity allows the full three dimensional distribution of galaxies to be calculated. In reality however galaxies near to a cluster will be undergoing infall towards the primary halo, and there will also be a significant dispersion in their mean streaming velocity. These additional motions cause distortions of the distribution of galaxies in redshift space, which can be analysed to obtain a statistical measure of the galaxy motions around a cluster. In order to predict the two dimensional cluster-galaxy redshift space correlation function or 'cosmic onion' we need an accurate model for both the mean infall and velocity dispersion of galaxies, and how there vary with primary halo mass and distance from the cluster centre. A description of the galaxy density distribution in real space is also required, to which the redshift space distortions will be applied to provide a prediction of the cosmic onion for a cluster with given primary halo mass.

Using the transition model presented in chapter 3 to obtain the infall velocity and density profiles for galaxies around a cluster, combined with the description for their line of sight velocity dispersion introduced in the previous chapter, a full model of the cosmic

onion will be developed which can be compared to observations. This will be applied to mock data generated from stacked clusters in the simulations, in an attempt to provide constraints on the primary halo mass. There will also be an investigation into the effect of changing different elements of the model, in order to ascertain the scales on which deviations from linearity need to be considered and also to isolate the model components that may require improvement. The feasibility of using this method to obtain halo mass constraints from galaxy redshift survey data will be discussed, in addition to the potential applications with regard to testing General Relativity.

5.1 Measuring halo mass from infall

In the first instance, predictions for galaxy infall provided by the transition model will be used to constrain the primary halo mass, by fitting to the infall velocity profile observed in stacked clusters from the simulations. In practice this would not be possible for real data as the infall velocity cannot be measured for individual galaxies, however using this method on the simulations where this information is available gives an indication of the constraining power for the infall model alone. It also allows the scales on which this model provides an accurate measure for halo mass to be determined, in comparison to constraints obtained using the linear model described in Sheth et al. (2001). The fitted primary halo mass $M_{\rm ph}^{\rm fit}$ is calculated via a maximum likelihood method, and divided by the true value $M_{\rm ph}^{\rm true}$ which is defined as the halo mass bin average for the given set of stacked clusters from the simulations. This quantity provides a measure for the ability of the relevant model to accurately constrain halo mass from the galaxy infall profile, and should be consistent with unity to indicate a correct reconstruction of the primary halo mass $M_{\rm ph}$.

Figure 5.1 shows halo mass constraints for stacked clusters with four different primary halo mass bins, fitted from the observed galaxy infall velocity profile measured from $r_{min} = 3$ Mpch^{-1} to a varying maximum radius r_{max} in the range of 20 to 100 Mpch^{-1}. The reconstructed halo mass fitted for different scales with the transition model is given, and compared with that obtained using the linear model. The halo mass bin width is varied for different datasets in order to include an adequate number of clusters, and the locations of upper and lower boundaries for the mass bins are indicated in each case. It can be seen that, for the three largest primary halo masses, the transition model constraints fall in the

most part within the mass bin limits, with the exception of the results for $M_{\rm ph} = 1 \times 10^{13}$ $\mathrm{M}_{solar}h^{-1}$ where the reconstructed halo mass is higher than expected when fitting out to large radii. The constraints for the most massive primary halo fall just inside the lower boundary of its mass bin, which is probably due to an uneven distribution of halo masses across the bin arising from the very low number of extremely high mass halos. This will result in a significantly larger proportion of halos with masses smaller than the bin centre, which could bias the reconstructed mass accordingly.

The linear model constraints shown in figure 5.1 are consistently higher than those obtained using the transition model, with the gap between the reconstructed primary halo masses widening as the galaxy infall velocity profile is fitted down to smaller scales. This difference also becomes more prominent with increasing cluster mass, with the constraints using the linear model above a factor of two greater than results from the transition model for the most massive primary halo at low r_{max}. For the two largest cluster masses it can be seen that the reconstructed halo mass, although much higher than the true value on all scales, does become more accurate with increasing r_{max}. The constraints for $M_{\rm ph} = 1 \times 10^{13}$ $\mathrm{M}_{solar}h^{-1}$ show the same trend out to a radius of approximately 70 $\mathrm{Mpc}h^{-1}$, however then begin to rise away from the true value again beyond this point. This implies that the linear model predictions for this primary halo mass are not in agreement with the simulations even on large scales, and provides an explanation for the inaccuracy in the transition model results as both of these descriptions for the galaxy infall velocity profile become identical above a certain radius. Constraints for the smallest cluster mass are poor when obtained using either model, and also converge quite rapidly as their predictions are almost equivalent for low halo masses except for galaxies close to the cluster centre.

It can be concluded from the results shown here that the transition model provides a significant improvement over the linear model when constraining primary halo mass from the galaxy infall velocity profile, and can be used to reliably reconstruct the halo mass for medium to large sized clusters even when fitting at relatively small scales. This model is however less accurate when applied to low mass clusters, and also should be used with caution when fitting out to large radii for intermediate halo masses. In both of these instances the transition model predictions display a greater similarity to the linear model, which may indicate an issue with the halo streaming model from which this is derived. Alternatively, these deviations in the halo mass constraints could arise from an inaccurate description of the density profiles in the above cases, as these are used for both

the transition and linear models when calculating the mean galaxy infall velocity from the sum of different halo streaming motions. In the following section, the galaxy infall models discussed here will be combined with predictions for the density profile and LOS velocity dispersion to obtain a complete description of the cosmic onion, which can be compared to those observed in stacked clusters from the simulations in order to provide constraints for the primary halo mass.

5.2 Cosmic onion model

5.2.1 Applying redshift space distortions

In order to fully model the cosmic onion for a cluster with given primary halo mass, we first need to obtain the galaxy number density in real space as a function of position relative to the cluster centre. This is calculated from the total density profile $\rho_{gal}^{tot}(r)$ predicted for the specified halo mass by applying spherical symmetry, which provides the galaxy density ρ_{gal}^{real} at two dimensional position r_π, r_σ on a grid in real space. The galaxy count $n_{gal}^{real}(r_\pi, r_\sigma)$ at each point on this grid is then evaluated by multiplying the density by the pixel volume, where the region of space represented by a single pixel takes the form of a cylindrical shell which gets larger with increasing r_σ. A description of the galaxy infall velocity at position r_π, r_σ is obtained, again by assuming spherical symmetry, from the infall profile $v_r^{\rm gal}(r)$ predicted by the transition model for the given primary halo mass. The line of sight component of this infall velocity, given by $v_{\rm los}^{\rm gal}(r_\pi, r_\sigma) = -v_r^{\rm gal}(r_\pi, r_\sigma)\cos(\phi)$ where ϕ is the angle between the LOS and position vector from the cluster centre, is then calculated for each location on the grid. The corresponding shift in the r_π direction $\Delta r_\pi = v_{\rm los}^{\rm gal}(r_\pi, r_\sigma)/H$ is then evaluated for individual pixels, and their apparent positions in redshift space obtained. This results in an unevenly spaced grid which describes the galaxy count in redshift space around a cluster, due to the effect of infall towards the primary halo.

The LOS velocity dispersion $\sigma_{\rm los}^{\rm gal}(r_\pi, r_\sigma)$ of galaxies in each pixel is then calculated for the specified halo mass using the model presented in the previous chapter, and applied as a Gaussian convolution along the r_π direction of width $\sigma_{\rm los}^{\rm gal}(r_\pi, r_\sigma)/H$. It is important to note that the velocity dispersion obtained for every individual pixel corresponds to its original position in real space, as apposed to the redshift space location calculated from galaxy infall. The effect of this velocity dispersion is to spread out the positions of galaxies

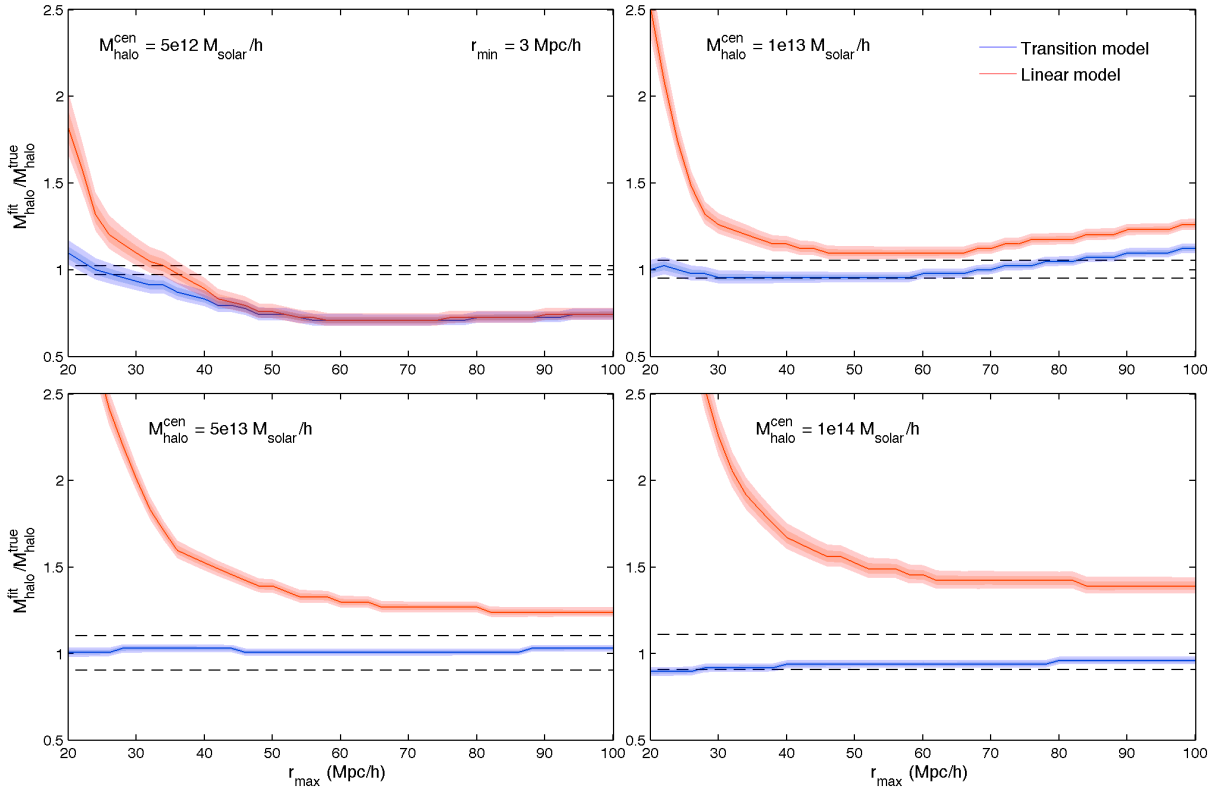

Figure 5.1. Primary halo mass constraints for stacked clusters from the simulations as a function of maximum scale, fitted from the observed effective galaxy infall velocity profile. The ratio of the fitted halo mass to the true value, defined as the mass bin average, is shown for both the transition (blue line) and linear (red line) galaxy infall models. Constraints corresponding to 68% and 95% confidence are indicated by shaded regions around the fitted values for each infall model. Results are given for four different primary halo mass bins centred on (from top left to bottom right) 5×10^{12}, 1×10^{13}, 5×10^{13} and 1×10^{14} M$_{solar}h^{-1}$, with dashed lines showing the upper and lower boundaries of each mass bin. Note that the figure labels $M^{\rm fit}_{\rm halo} = M^{\rm fit}_{\rm ph}$, $M^{\rm true}_{\rm halo} = M^{\rm true}_{\rm ph}$ and $M^{\rm cen}_{\rm halo} = M_{\rm ph}$.

in redshift space along the LOS, and the resulting distribution is evaluated as a function of r_π for each pixel. These galaxy counts are subsequently binned onto a regularly spaced grid in r_π, r_σ coordinates, summing the contributions from all pixels to obtain the total galaxy count in redshift space $n^z_{gal}(r_\pi, r_\sigma)$. This can then be divided by the pixel volume at each point in order to calculate the galaxy number density in redshift space $\rho^z_{gal}(r_\pi, r_\sigma)$, therefore providing a complete description of the cosmic onion for the given primary halo mass. The above process is summarised in the flow chart shown in figure 5.2.

The numerical cosmic onion model discussed in this section can be used to predict the distribution of galaxies in redshift space around a cluster of given mass, and compared with results from stacked clusters in the simulations in order to provide constraints for the primary halo mass. Mock data is generated for eight different halo mass bins the lowest of which is centred on 2.00×10^{12} $\mathrm{M}_{solar}h^{-1}$, with subsequent bins increasing by a factor of two each time up to a maximum of 2.56×10^{14} $\mathrm{M}_{solar}h^{-1}$. The properties of these primary halo mass bins are given in table 5.1 which shows both the bin width and average halo mass in each case, and also the number of clusters stacked N_{clus} and total galaxy count N^{tot}_{gal} within radius $r_{max} = 100$ Mpch^{-1} of the primary halo. The observed cosmic onion for these stacked clusters is obtained by measuring the LOS velocity component for each individual galaxy and calculating its corresponding position in redshift space, and then binning these galaxies onto a regularly spaced grid in r_π, r_σ coordinates to give the count at different locations. This process is then repeated taking the LOS along each of the x, y and z directions, and the galaxy counts summed to obtain the total observed redshift space count $n^z_{obs}(r_\pi, r_\sigma)$ as a function of position relative to the cluster centre.

The cosmic onion model described above can then be used to predict the equivalent galaxy count $n^z_{mod}(r_\pi, r_\sigma)$ around stacked clusters for a given primary halo mass, which is calculated from the distribution for a single cluster as $n^z_{mod}(r_\pi, r_\sigma) = 3N_{clus}n^z_{gal}(r_\pi, r_\sigma)$. It is assumed that the predominant source of uncertainty in each pixel is Poisson noise, and therefore the error on the predicted galaxy count at position r_π, r_σ is given by $\sqrt{n^z_{mod}}$. The primary halo mass can be fitted from $n^z_{obs}(r_\pi, r_\sigma)$ for stacked clusters in the simulations using this model, employing a maximum likelihood method to provide halo mass constraints for the datasets summarised in table 5.1. These reconstructed halo masses will then be compared to the true values in order to determine the accuracy of this numerical cosmic onion model, and give an indication of its ability to constrain primary halo mass from the redshift space distortions around a cluster.

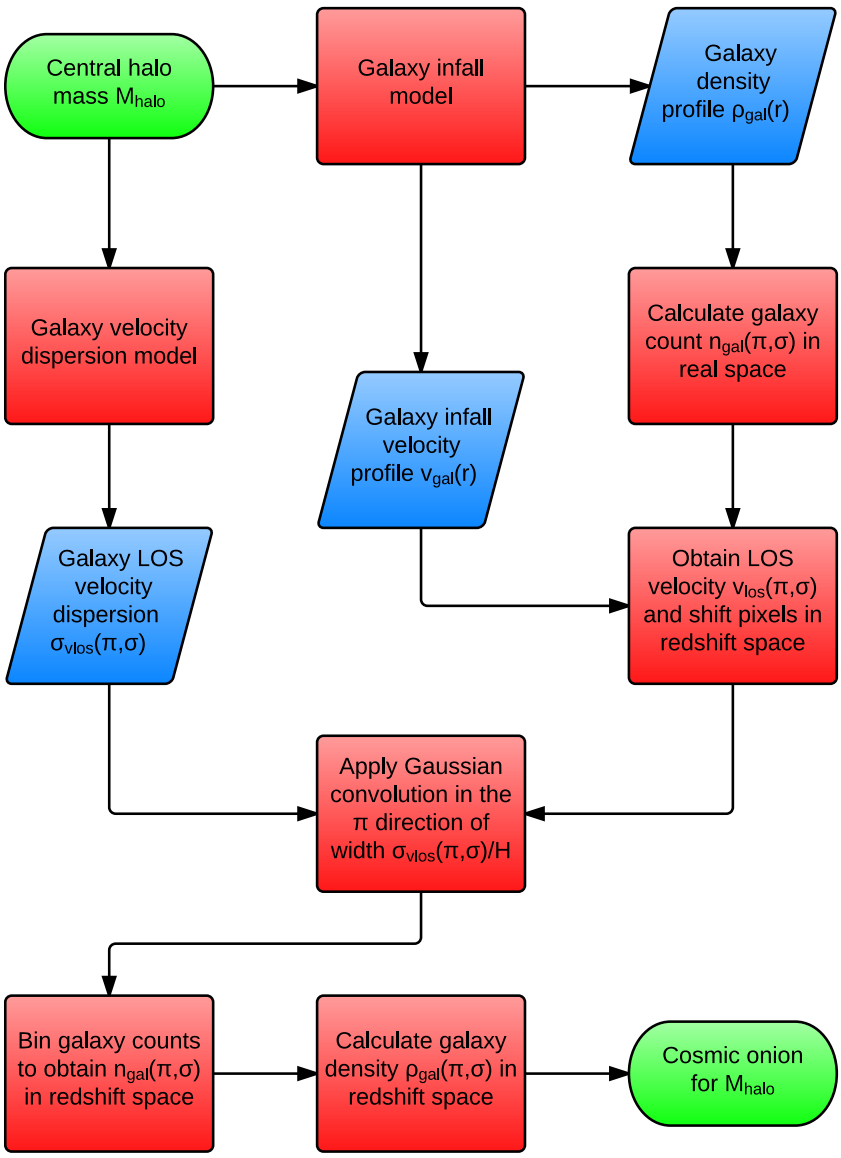

Figure 5.2. Flow chart illustrating the method used to model the cosmic onion for a cluster with given primary halo mass. The main input and output are indicated in green, and red boxes describe each stage of the process with intermediate inputs and outputs for the model shown in blue. Note that the input term $M_{\rm halo}$ represents the primary halo mass $M_{\rm ph}$, and the coordinates $\pi = r_\pi$ and $\sigma = r_\sigma$.

$M_{\rm ph}$	Bin width	Average $M_{\rm ph}$	N_{clus}	$N_{gal}^{tot}(r_{max})$
2.00×10^{12}	4.00×10^{10}	2.00×10^{12}	10855	1.27×10^{8}
4.00×10^{12}	2.40×10^{11}	4.00×10^{12}	10165	1.19×10^{8}
8.00×10^{12}	7.20×10^{11}	7.98×10^{12}	10851	1.27×10^{8}
1.60×10^{13}	2.88×10^{12}	1.59×10^{13}	10218	1.20×10^{8}
3.20×10^{13}	6.40×10^{12}	3.18×10^{13}	5527	6.48×10^{7}
6.40×10^{13}	1.92×10^{13}	6.26×10^{13}	3345	3.96×10^{7}
1.28×10^{14}	5.12×10^{13}	1.23×10^{14}	1347	1.60×10^{7}
2.56×10^{14}	1.28×10^{14}	2.38×10^{14}	408	4.85×10^{6}

Table 5.1. Properties of stacked clusters from the simulations with eight different primary halo mass bins, used to generate mock observations of the cosmic onion. The halo mass bin centres, widths and average values are stated in each case, all given in units of $\mathrm{M}_{solar}h^{-1}$. The number of halos stacked is also shown, and the total count of galaxies which reside within a distance of 100 Mpch^{-1} from the cluster centre.

5.2.2 Infall velocity constraints

Initially, constraints for the galaxy infall velocity profile will be obtained for the stacked clusters described above, before attempting to fully reconstruct the primary halo mass. This allows the accuracy of both the models for galaxy density in real space and velocity dispersion to be determined, and gives an indication of the effect these will have on halo mass constraints provided by the cosmic onion model. In order to achieve this we first need to introduce a suitable parameterisation for the infall velocity profile, which can then be fitted from the observed galaxy count in redshift space around stacked clusters in the simulations. For a given primary halo mass bin, the fitted galaxy infall velocity is defined as $v_r^{\rm fit}(r) = F_{vr} v_r^{\rm true}(r)$ where $v_r^{\rm true}(r)$ is the true infall profile measured directly from the simulations for the relevant dataset. The parameter F_{vr} can be varied to produce different inputs for $v_r^{\rm gal}(r)$ to the cosmic onion model (as shown in blue on the flow chart in figure 5.2), keeping the other two inputs for $\rho_{gal}(r)$ and $\sigma_{\rm los}^{\rm gal}(r_\pi, r_\sigma)$ fixed. A maximum likelihood method is then used to fit F_{vr} from the observed $n_{obs}^z(r_\pi, r_\sigma)$ for stacked clusters in the specified halo mass bin, where the constraints obtained should be consistent with unity if the galaxy infall profile is being correctly reconstructed.

This approach provides a way to effectively exclude the effects which result from inaccuracies in the predicted infall velocity, and therefore examine how other components of the numerical cosmic onion model will potentially bias the halo mass constraints. The reconstructed galaxy infall profile can be fitted with either $\rho_{gal}(r)$ or $\sigma_{\rm los}^{\rm gal}(r_\pi, r_\sigma)$ measured

directly from the simulations as a fixed input to the cosmic onion model, and compared to the results obtained using predictions of these quantities for the given primary halo mass bin as inputs. The deviation from unity of the fitted parameter F_{vr} will show the effect of using each model for the galaxy density and velocity dispersion on the infall velocity constraints, and indicate how any differences between the predicted and observed $\rho_{gal}(r)$ or $\sigma^{\rm gal}_{\rm los}(r_\pi, r_\sigma)$ may bias the reconstructed halo mass provided by the full cosmic onion model. It is also useful to examine the constraints for F_{vr} which result from both of these fixed inputs being measured directly from the simulations, as this allows the accuracy of the numerical method used to calculate the cosmic onion to be tested for the available primary halo mass bins.

Figure 5.3 shows the infall velocity constraints obtained using different inputs for the galaxy density and velocity dispersion to the cosmic onion model, fitted from the observed galaxy distribution in redshift space around stacked clusters from the simulations. Results are given for all eight primary halo mass bins fitting from $n^z_{obs}(r_\pi, r_\sigma)$ out to a distance of 100 Mpch^{-1} from the cluster centre, with constraints for the parameter F_{vr} shown for each dataset. It can be seen that, when the fixed inputs for both $\rho_{gal}(r)$ and $\sigma^{\rm gal}_{\rm los}(r_\pi, r_\sigma)$ are measured from the simulations, the infall velocity constraints are consistent with unity for halo masses above $M_{\rm ph} \sim 4 \times 10^{13}$ M$_{solar}h^{-1}$, however drop slightly below this for smaller cluster masses. This demonstrates that the numerical method used to model redshift space distortions around a cluster provides a mostly accurate description of the cosmic onion, although needs to be improved for low primary halo masses. The variation in galaxy infall velocity is less prominent in these clusters resulting in smaller corresponding shifts of position in redshift space, and therefore this issue could most likely be resolved by increasing the resolution of the r_π, r_σ grid on which galaxy density ρ^{real}_{gal} is calculated before the redshift space distortions are applied. In addition to the effects caused by a finite pixel resolution, the assumption that $\sigma^{\rm gal}_{\rm los}(r_\pi, r_\sigma)$ is Gaussian may also produce a bias in the reconstructed infall velocity profile. This could potentially be improved by using a more accurate model for the galaxy velocity dispersion, instead of the Gaussian convolution applied when generating the cosmic onion.

The infall velocity constraints shown in figure 5.3 which are obtained using the observed $\rho_{gal}(r)$ as above, but predicting the input for $\sigma^{\rm gal}_{\rm los}(r_\pi, r_\sigma)$ from the galaxy velocity dispersion model, display a strong similarity to the results for which both inputs to the cosmic onion model are measured directly from the simulations. There is a slight variation

between the reconstructed galaxy infall profiles for higher primary halo mass bins, which implies that the velocity dispersion model is less accurate for more massive clusters. However for the majority of halo mass bins the constraints for infall velocity are consistent with one another when using either the predicted or observed $\sigma_{\rm los}^{\rm gal}(r_\pi, r_\sigma)$ as an input to the cosmic onion model, and therefore the model for galaxy velocity dispersion can be described as reasonably accurate for the purposes required here. In contrast to this, when using the observed $\sigma_{\rm los}^{\rm gal}(r_\pi, r_\sigma)$ and predicting the input for $\rho_{gal}(r)$ from the galaxy infall model, the infall velocity constraints obtained deviate significantly from unity compared to the case where both inputs to the cosmic onion model are measured from the simulations. The reconstructed galaxy infall profiles show a wide variation across different primary halo mass bins with the fitted parameter F_{vr} ranging from approximately 1.15 for low halo mass bins, down to around 0.8 for the most massive cluster. This indicates that the constraints for infall velocity are extremely sensitive to inaccuracies in the galaxy density $\rho_{gal}(r)$ input to the numerical cosmic onion model, when fitting from the redshift space galaxy distribution out to large scales around a cluster.

It has been shown that the accuracy of the numerical method used to calculate the cosmic onion, and both the galaxy density and velocity dispersion inputs to this model, all effect the obtained infall velocity constraints to varying different degrees. The galaxy infall profiles reconstructed for the given primary halo mass bins are seen to exhibit a strong dependence on the density input, and to a lesser extent the velocity dispersion input to the cosmic onion model. The finite density grid resolution used when applying redshift space distortions in the numerical cosmic onion model is also shown to have an effect on the infall velocity constraints for low halo mass bins, which results in a slight underestimation of the galaxy infall profiles reconstructed in these cases. The velocity dispersion model used is seen to bias the infall velocity constraints in the same way, except that the fitted parameter F_{vr} only drops below that obtained using the observed $\sigma_{\rm los}^{\rm gal}(r_\pi, r_\sigma)$ for higher halo mass bins. It is demonstrated however that the component of the cosmic onion model which most significantly effects the reconstructed galaxy infall velocity profile is the input for $\rho_{gal}(r)$, where the predicted galaxy density used is shown to result in a strong overestimation of the infall velocity for small cluster masses and underestimates the constraints for more massive primary halos to an even greater extent.

The effect of these different elements of the model on reconstructed infall profiles described here are expected to produce a similar bias in the halo mass constraints provided

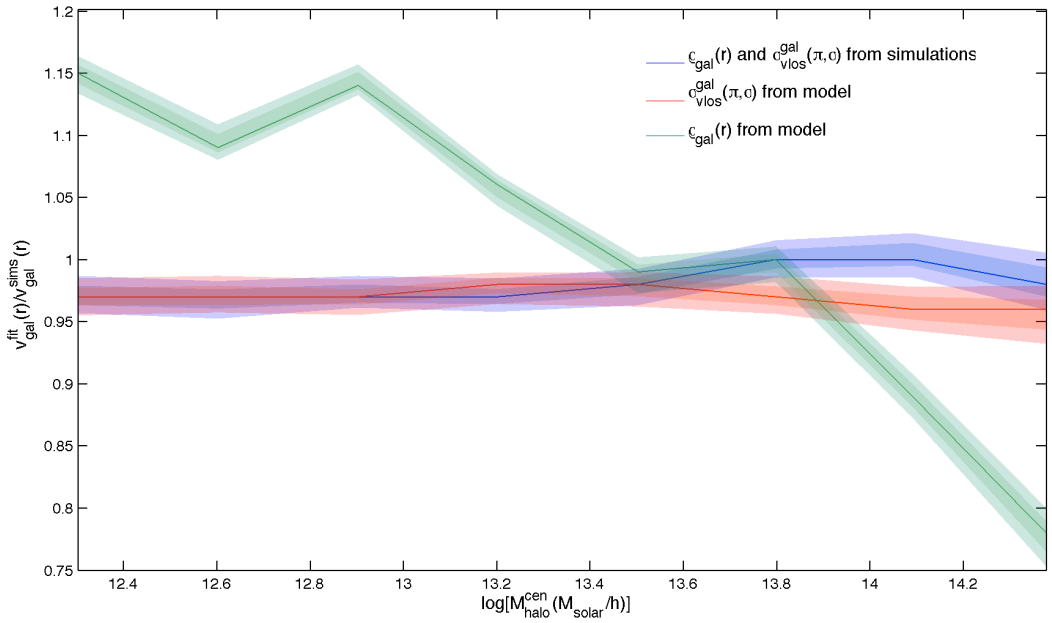

Figure 5.3. Galaxy infall velocity profile constraints for stacked clusters from the simulations as a function of primary halo mass, fitted from the full observed galaxy count in redshift space. The fitted galaxy infall velocity profiles, expressed as a multiple of the true profile measured in the simulations, are given for different density and velocity dispersion inputs to the numerical cosmic onion model. Results obtained using these quantities as measured directly from the simulations (blue line) and the model predictions for galaxy density (green line) and LOS velocity dispersion (red line) are shown, with constraints corresponding to 68% and 95% confidence indicated by shaded regions around the fitted values for each case. Note that the figure labels $v_{\rm gal}^{\rm fit} = v_r^{\rm fit}$, $v_{\rm gal}^{\rm sims} = v_r^{\rm true}$, $M_{\rm halo}^{\rm cen} = M_{\rm ph}$ and $\sigma_{\rm vlos}^{\rm gal}(\pi,\sigma) = \sigma_{\rm los}^{\rm gal}(r_\pi, r_\sigma)$.

by the full cosmic onion model, as an increase in the galaxy infall velocity translates to a higher estimate of the primary halo mass in a cluster. It can therefore be concluded that both the numerical method used to calculate the cosmic onion and the predicted velocity dispersion input to this model should have a relatively small effect on the halo mass constraints obtained from the redshift space galaxy distribution observed around a cluster, however there will potentially be a substantial bias resulting from inaccuracies in the real space density model when fitting out to large scales. The galaxy density profile predicted for a given halo mass may consequently need some improvement, in order to use the numerical cosmic onion model to correctly reconstruct the primary halo mass in a cluster.

5.2.3 Comparison of models

In the previous section, predictions of the galaxy infall velocity profile around a cluster were used to obtain constraints for the primary halo mass, and a comparison made between results from both the transition and linear models fitted over a variety of scales for different halo mass bins. It was found that the halo mass could be reliably reconstructed for medium to large sized clusters using the transition model, and that this provided a significant improvement over the linear model especially when fitting out to smaller radii. The difference observed between these models when constraining the primary halo mass solely from galaxy infall velocity may not however be equivalent to that seen in the reconstructed halo mass fitted from the cosmic onion on the same scale, as the density at a given position in redshift space will depend on the infall of galaxies which reside at a distance further from the cluster centre. In order to establish the scales at which the galaxy distribution in redshift space is significantly effected by the choice of infall model, the predicted galaxy count $n^z_{gal}(r_\pi, r_\sigma)$ is calculated for several different primary halo masses using both the linear and transition models to provide the infall velocity input to the cosmic onion model. The galaxy count obtained using the infall profile from the transition model is then divided by the prediction calculated with the linear model input in each case, to give the ratio of $n^z_{gal}(r_\pi, r_\sigma)$ as a function of position relative to the cluster centre and indicate how this varies with primary halo mass.

Figure 5.4 shows the ratio of redshift space galaxy counts obtained using the transition and linear models to calculate the infall velocity input to the cosmic onion model, for eight different primary halo masses. It can be seen that, as would be expected from comparing the infall profiles provided by each model, the differences between the predicted galaxy counts in redshift space are more prominent close to the cluster centre and also extend out to larger scales with increasing halo mass. The variation in this ratio of $n^z_{gal}(r_\pi, r_\sigma)$ demonstrates that the galaxy count obtained using the transition model is higher for very small r_π but then drops lower immediately outside this region, when compared to that calculated from the linear model. This is due to the greater degree of infall predicted by the transition model near to the primary halo, which shifts the galaxy positions in redshift space further towards the cluster centre in the r_π direction than for the case described by the linear model. The magnitude of these shifts depends on the LOS component of the galaxy infall velocity which varies with position relative to the

primary halo, and consequently the resulting effect on the ratio of $n^z_{gal}(r_\pi, r_\sigma)$ is seen to be spherically asymmetric. It is interesting to note that the difference between the redshift space galaxy counts predicted using both the linear and transition models diminishes more rapidly with scale than may be expected from examining the corresponding variation in their infall profiles, particularly when measured along the r_σ direction. However there is still a significant effect on $n^z_{gal}(r_\pi, r_\sigma)$ which arises from the choice of galaxy infall model, especially for large primary halo masses, and it can therefore be concluded that using the transition model as apposed to the linear prediction for galaxy infall velocity when modelling the cosmic onion should provide an improvement on halo mass constraints obtained from the redshift space galaxy distribution on quasi-linear scales around a cluster.

It has been shown that the choice of infall model has a significant effect on the redshift space galaxy distribution predicted by the numerical cosmic onion model, and the variation of this effect with position relative to the cluster centre has been demonstrated for several different primary halo masses. The same approach can be taken in order to determine if there is a similar difference in $n^z_{gal}(r_\pi, r_\sigma)$ obtained using the galaxy velocity dispersion model to provide the input for $\sigma^{\rm gal}_{\rm los}(r_\pi, r_\sigma)$, compared to that calculated from a constant LOS velocity dispersion input to the cosmic onion model. The predicted galaxy count in redshift space is evaluated for various different cluster masses using the velocity dispersion obtained from the coherence model, and then the average of $\sigma^{\rm gal}_{\rm los}(r_\pi, r_\sigma)$ taken over all positions and the resulting value used as a scale independent constant velocity dispersion input to calculate $n^z_{gal}(r_\pi, r_\sigma)$. In both cases the infall velocity input is provided by predictions from the transition model, so that only the velocity dispersion input to the cosmic onion model is being varied. The galaxy count obtained using the velocity dispersion from the coherence model is then divided by that calculated with a constant LOS velocity dispersion input for each primary halo mass, to give the ratio of $n^z_{gal}(r_\pi, r_\sigma)$ as a function of position relative to the cluster centre.

Figure 5.5 shows the ratio of redshift space galaxy counts obtained using the coherence model to calculate the velocity dispersion and a scale independent constant velocity dispersion input to the cosmic onion model, for eight different primary halo masses. It can be seen that, as for the case where the galaxy infall model was varied, the differences between the predicted galaxy counts are more prominent near to the primary halo and extend out to larger scales with increasing cluster mass, although exhibit a much weaker halo mass dependence than in the previous instance. The ratio of $n^z_{gal}(r_\pi, r_\sigma)$ also varies

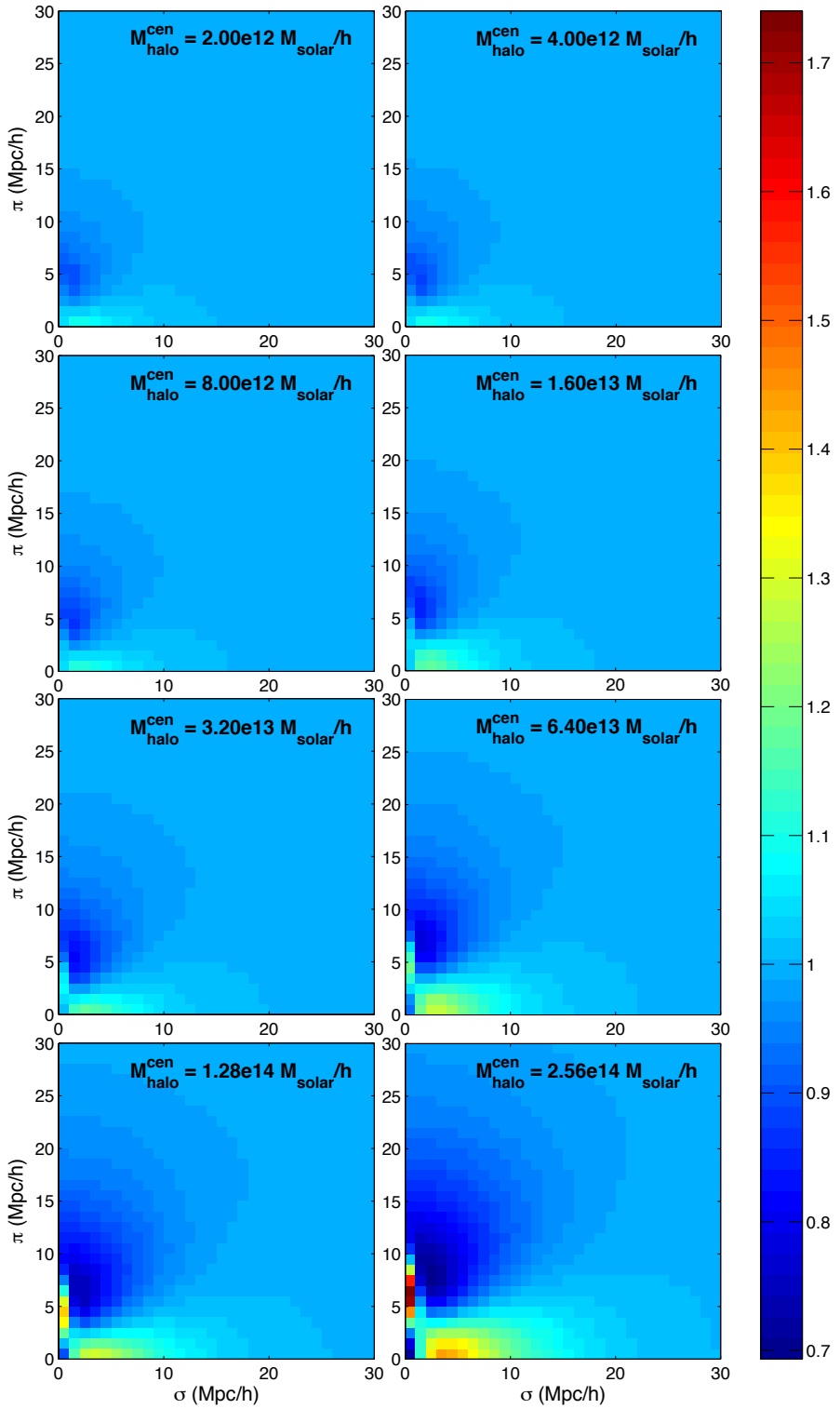

Figure 5.4. Ratio of galaxy counts in redshift space predicted using different models for the infall velocity profile, as a function of position relative to the cluster centre. The galaxy count prediction for the transition model divided by that calculated using the linear infall model is shown for eight different primary halo masses. The colour bar represents the ratio between galaxy counts, and the figure labels $\pi = r_\pi$, $\sigma = r_\sigma$ and $M_{\rm halo}^{\rm cen} = M_{\rm ph}$.

in a similar way, demonstrating that the galaxy count obtained using $\sigma_{\rm los}^{\rm gal}(r_\pi, r_\sigma)$ from the coherence model is significantly higher at very small r_π and again drops lower just outside this region, when compared to that calculated for a constant LOS velocity dispersion. This difference in variation along the r_π and r_σ directions is to be expected for the ratio of galaxy counts in redshift space, due to spherical asymmetry displayed in the velocity dispersion provided by the coherence model. The predictions for $n_{gal}^z(r_\pi, r_\sigma)$ evaluated with both velocity dispersion inputs to the cosmic onion model converge relatively quickly with distance from the cluster centre, as the density falls to a small, near-constant value and the differences in velocity dispersion begin to have a negligible effect on the galaxy distribution in redshift space. However on smaller scales the choice of galaxy velocity dispersion model has a strong effect on $n_{gal}^z(r_\pi, r_\sigma)$ for all the primary halo masses shown here, and it can therefore be concluded that using the scale dependent $\sigma_{\rm los}^{\rm gal}(r_\pi, r_\sigma)$ predicted by the coherence model as apposed to a constant LOS velocity dispersion when modelling the cosmic onion will potentially improve the cluster mass constraints obtained from redshift space distortions in the quasi-linear regime.

5.3 Cluster mass constraints

5.3.1 Infall model dependence

In this section primary halo mass constraints will be obtained from the observed galaxy count in redshift space around stacked clusters in the simulations, using various infall profile and velocity dispersion inputs to the numerical cosmic onion model. Firstly, the halo mass is reconstructed from $n_{obs}^z(r_\pi, r_\sigma)$ for stacked clusters with eight different primary halo mass bins summarised in table 5.1, using both the transition and linear models to predict the galaxy infall velocity when calculating $n_{mod}^z(r_\pi, r_\sigma)$ from the cosmic onion model as described in the previous section. The halo mass is fitted for each dataset via a maximum likelihood method, and divided by the true value which is defined as the average primary halo mass for a given set of stacked clusters from the simulations. This quantity gives an indication of the accuracy of the cluster mass constraints obtained using each galaxy infall model, and should be consistent with unity if the halo mass has been correctly reconstructed. The cluster mass constraints are calculated for each primary halo mass bin by fitting to the observed redshift space galaxy count out to various maximum radii, measuring $n_{obs}^z(r_\pi, r_\sigma)$ within a distance of $r_{max} = 10$, 20, 30 and 40 Mpch^{-1} from

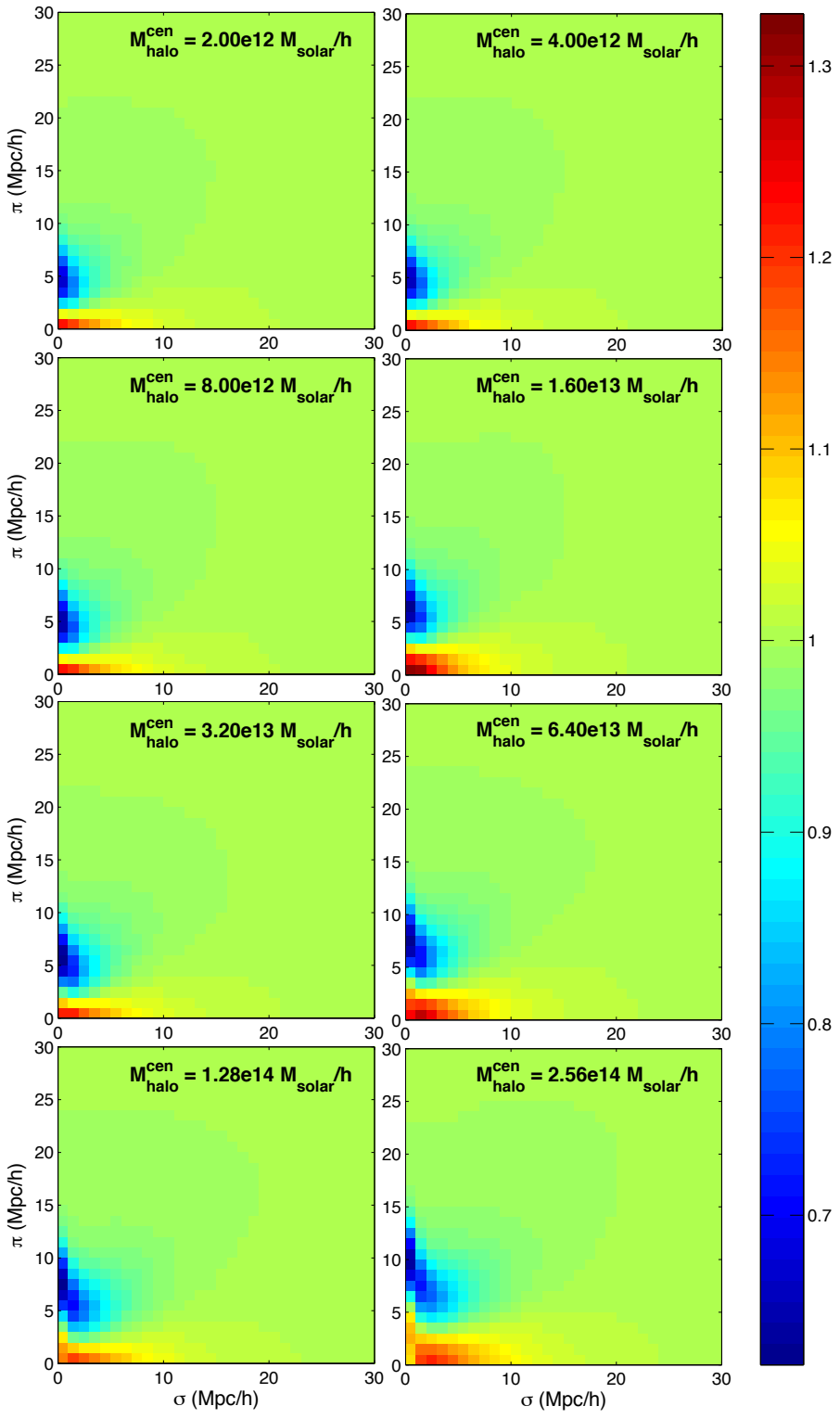

Figure 5.5. Ratio of galaxy counts in redshift space predicted using different models for the velocity dispersion, as a function of position relative to the cluster centre. The galaxy count prediction for the coherence model divided by that calculated using a constant LOS velocity dispersion is shown for eight different primary halo masses. The colour bar represents the ratio between galaxy counts, and the figure labels $\pi = r_\pi$, $\sigma = r_\sigma$ and $M_{\rm halo}^{\rm cen} = M_{\rm ph}$.

the cluster centre. In all cases the galaxy count is cut off below $r_\sigma = 3$ Mpch^{-1}, in order to exclude the Fingers of God effect which arises from the virial motion of galaxies in the primary halo.

Figure 5.6 shows halo mass constraints obtained using both the transition and linear models to provide the galaxy infall velocity input to the cosmic onion model, fitted from the galaxy distribution in redshift space observed around stacked clusters from the simulations. Results are given for all eight primary halo mass bins fitted from $n^z_{obs}(r_\pi, r_\sigma)$ out to a maximum radius of 10 and 20 Mpch^{-1}, with the reconstructed halo mass divided by the true value shown in each case. As discussed previously, the halo mass bin width used for different sets of stacked clusters is varied in order to ensure that a large enough number of halos are included, and the upper and lower mass bin limits are indicated for the given datasets. It can be seen that, for both values of r_{max}, the results obtained using the transition model fall mainly within the boundaries corresponding to each mass bin, although the reconstructed halo mass is overestimated for small clusters and also drops below the bin limit for the most massive primary halos. This is not unexpected given the bias on infall velocity constraints arising from inaccuracies in the real space density model used to calculate the cosmic onion, which was demonstrated earlier. The bias on halo mass constraints however appears to be less pronounced when fitting to $n^z_{obs}(r_\pi, r_\sigma)$ on small scales, compared to that seen in the reconstructed infall profiles where $r_{max} = 100$ 40 Mpch^{-1}. This is most likely due to the fact that the constraints for halo mass are more sensitive to the effects of galaxy infall close to the cluster centre, where there is a much greater degree of deviation between the mean infall velocity around halos of different masses. At sufficiently large scales however, these infall profiles converge and the predominant factor in determining cluster mass becomes the galaxy distribution in real space. It is therefore expected that the bias which occurs due to the predicted density input to the cosmic onion model will have a significantly stronger effect when fitting out to large radii, particularly for low mass primary halos, and this suggestion is supported by the results obtained for $r_{max} = 30$ and 40 Mpch^{-1} where the halo mass constraints lie well outside the bin limits for small to medium sized clusters.

The reconstructed halo masses obtained using the linear model are seen to be substantially higher than those calculated from the transition model, although the gap between these constraints is much wider when fitting out to a distance of 10 Mpch^{-1} than for $r_{max} = 20$ Mpch^{-1}. This is unsurprising given the variation between the predicted

$n^z_{gal}(r_\pi, r_\sigma)$ for the different galaxy infall models, shown in figure 5.4, is much more prominent close to the cluster centre. The halo mass constraints provided by the linear model for $r_{max} = 10$ Mpch^{-1} fall significantly above the bin limits for most of the given cluster masses, however appear more consistent with the true value for the highest primary halo mass bins. This is misleading though, as the bias which arises from inaccuracies in the galaxy density input to the cosmic onion model has been shown to lower the reconstructed halo mass for large clusters. Given that the constraints obtained by fitting directly from the infall velocity profile using the linear model (shown in figure 5.1) are seen to greatly overestimate the primary halo mass for clusters of this size, it can be assumed that using the linear model to provide the galaxy infall velocity input to the cosmic onion model produces a poor reconstruction of the halo mass, for all the available datasets, when fitting to the redshift space galaxy distribution on small scales. The difference between the results from the linear and transition models shown in figure 5.6 is less pronounced when fitting out to a radius of 20 Mpch^{-1}, although the halo mass constraints follow a similar trend to that seen for $r_{max} = 10$ Mpch^{-1} and the bias which occurs due to the real space density model predictions is expected to effect the reconstructed halo mass for both galaxy infall models in the same way. It is important to note that, for the higher primary halo mass bins, constraints which drop below unity may still indicate a correct reconstruction of the halo mass as there is an uneven distribution across these bins arising from the sparse number of very massive clusters, and this is therefore likely to add to the bias discussed previously for large primary halos.

It has been shown that, for both values of r_{max}, using the transition model introduced in this work provides a significant improvement over the linear model, when used to predict the galaxy infall velocity input to the cosmic onion model and constrain halo mass from the redshift space galaxy distribution around stacked clusters in the simulations. However it has also been demonstrated that in order to reliably reconstruct the primary halo mass using the numerical cosmic onion model we need to develop a more accurate description of the galaxy density in real space, especially outside the region where cluster mass is predominantly constrained by the effects of infall. The improved density predictions could then be combined with the transition model for galaxy infall to allow halo mass constraints to potentially be obtained from redshift space distortions on various scales throughout the quasi-linear regime, for clusters with a wide range of different primary halo masses.

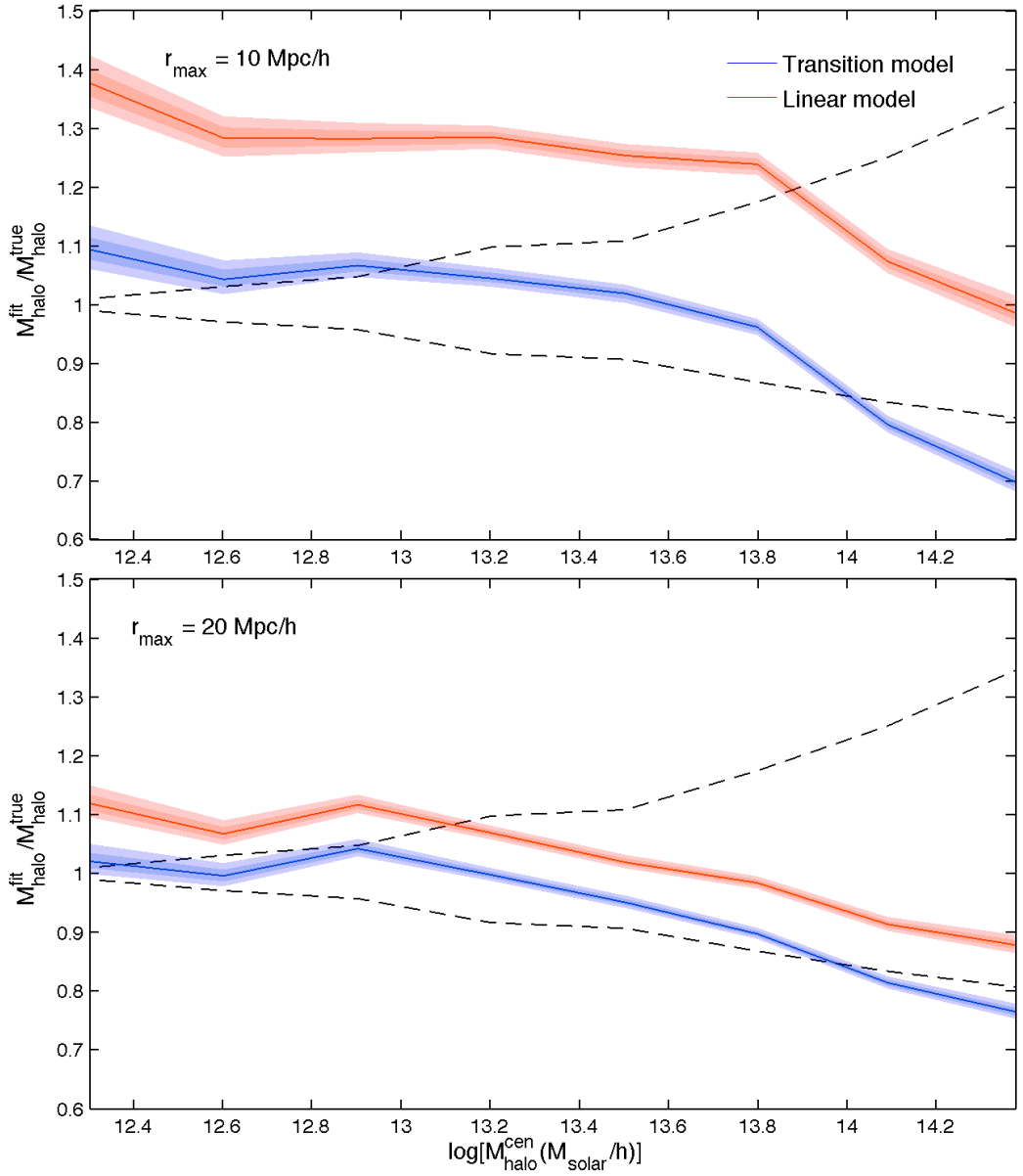

Figure 5.6. Primary halo mass constraints for stacked clusters from the simulations as a function of true halo mass, fitted from the observed galaxy count in redshift space. The ratio of the fitted halo mass to the true value is given for the numerical cosmic onion model, using both the transition (blue line) and linear (red line) models to predict the galaxy infall velocity profile. Constraints corresponding to 68% and 95% confidence are indicated by shaded regions around the fitted values for each infall model. Results obtained by fitting out to a maximum radius of 10 (top) and 20 (bottom) Mpch^{-1} are shown, with dashed lines marking the upper and lower boundaries of each halo mass bin. Note that the figure labels $M^{\rm fit}_{\rm halo} = M^{\rm fit}_{\rm ph}$, $M^{\rm true}_{\rm halo} = M^{\rm true}_{\rm ph}$ and $M^{\rm cen}_{\rm halo} = M_{\rm ph}$.

5.3.2 Velocity dispersion dependence

The effect on halo mass constraints of using either the transition or linear model to calculate the galaxy infall velocity input to the cosmic onion model has been examined here in detail, and for both of these cases the velocity dispersion input was provided by the coherence model. It was established that the primary halo mass was reconstructed with a greater degree of accuracy using the transition model compared to the linear prediction for galaxy infall, when fitted from the observed redshift space distribution of galaxies around stacked clusters in the simulations on quasi-linear scales. In order to investigate whether a similar improvement is seen in the halo mass constraints from the use of a position dependent galaxy velocity dispersion provided by the coherence model, as apposed to a constant LOS velocity dispersion input to the cosmic onion model, the halo mass is reconstructed from $n^z_{obs}(r_\pi, r_\sigma)$ for the same datasets as before using a constant velocity dispersion input calculated by averaging the coherence model prediction for $\sigma^{\rm gal}_{\rm los}(r_\pi, r_\sigma)$ over all positions. The galaxy infall profile is provided by the transition model in this case, and the halo mass constraints can therefore be compared to the previous results for this infall model to demonstrate the effect of using different descriptions for the velocity dispersion. The primary halo mass is again fitted for each set of stacked clusters via a maximum likelihood method, and divided by the true value to give a measure of accuracy for the cluster mass constraints obtained using a constant LOS velocity dispersion. The reconstructed halo mass is calculated by fitting to the observed galaxy count in redshift space out to the same r_{max} used earlier, excluding Fingers of God effects by cutting off the galaxy count at $r_\sigma = 3$ Mpch^{-1}.

Figure 5.7 shows halo mass constraints obtained using both the coherence model prediction for $\sigma^{\rm gal}_{\rm los}(r_\pi, r_\sigma)$ and a constant LOS velocity dispersion input to the cosmic onion model, fitted from the redshift space galaxy distribution observed around stacked clusters in the simulations. As for the previous case, results are given for all eight primary halo mass bins with $n^z_{obs}(r_\pi, r_\sigma)$ fitted out to a maximum radius of 10 and 20 Mpch^{-1}, and the reconstructed halo mass divided by the true value shown for individual datasets. The locations of the upper and lower mass bin limits are again indicated for each set of stacked clusters, to give the halo mass constraints in relation to the different bin widths. It can be seen that the variation between the results obtained using a constant LOS velocity dispersion and those calculated from the coherence model displays a similar trend to the

difference observed for cluster mass constraints in the case where galaxy infall is predicted by the linear model, with the reconstructed halo masses being significantly higher for a constant velocity dispersion input to the cosmic onion model. This variation is also more pronounced when fitting out to a distance of 10 Mpch^{-1} than for r_{max} = 20 Mpch^{-1}, although the gap between cluster mass constraints for the different galaxy velocity dispersion inputs is shown to narrow with increasing primary halo mass. In real terms however, as the results are expressed as a ratio of the reconstructed halo mass to the true value, the variation shown between the constraints represents a larger absolute difference in cluster mass, which for example at r_{max} = 10 Mpch^{-1} is approximately 9×10^{11} M$_{solar}h^{-1}$ for the lowest halo mass bin and 2×10^{13} M$_{solar}h^{-1}$ for the most massive clusters. This gap is expected to be less dependent on primary halo mass than for the comparison made between the linear and transition models for galaxy infall, where at the same maximum radius the difference in constraints for the lowest and highest halo mass bins are 6×10^{11} and 7×10^{13} M$_{solar}h^{-1}$ respectively, as the variation in $n^z_{gal}(r_\pi, r_\sigma)$ predicted by the cosmic onion model for the two velocity dispersion inputs (shown in figure 5.5) displays much less dependence on cluster mass.

The offset between the primary halo mass constraints obtained using the different descriptions for the galaxy velocity dispersion occurs due to the fact that the coherence model prediction for $\sigma^{\rm gal}_{\rm los}(r_\pi, r_\sigma)$ is significantly lower on small scales, when compared to the mean value which is applied as a constant LOS velocity dispersion input to the cosmic onion model. The result of the higher velocity dispersion in the latter case is to stretch out the galaxy distribution in redshift space along the LOS, which counteracts the effects from infall and therefore causes an overestimation of the cluster mass. This variation in the constraints provided using the two velocity dispersion inputs is less prominent when fitting out to a distance of 20 Mpch^{-1} than for r_{max} = 10 Mpch^{-1}, which is unsurprising given that the ratio between $n^z_{gal}(r_\pi, r_\sigma)$ predicted by the cosmic onion model for these different descriptions of $\sigma^{\rm gal}_{\rm los}(r_\pi, r_\sigma)$ is close to unity outside a radius of $\sim$ 10 Mpch^{-1} for most of the primary halo masses shown in figure 5.5. The bias on cluster mass constraints which arises from inaccuracies in the real space density model used to calculate $n^z_{mod}(r_\pi, r_\sigma)$ is expected to have the same effect on the reconstructed halo mass as was discussed previously, lowering the constraints obtained using a constant LOS velocity dispersion for large cluster masses and causing them to appear more consistent with the true value than may actually be the case. The additional bias which occurs due to the uneven distribution

of halo masses across the bins used when stacking clusters from the simulations will also potentially increase this effect, resulting in the reconstructed halo mass being unreliable for the most massive clusters.

It has been demonstrated that, for both values of r_{max} shown here, the coherence model predictions for $\sigma_{\rm los}^{\rm gal}(r_\pi, r_\sigma)$ provide a substantial improvement over using a constant LOS velocity dispersion input to the cosmic onion model, when constraining primary halo mass from the galaxy distribution in redshift space around stacked clusters from the simulations. It can be concluded that the use of the coherence model to provide a position dependent description of the galaxy velocity dispersion, combined with the transition model predictions for infall velocity, allow significantly more accurate halo mass constraints to be obtained when fitting from $n_{obs}^z(r_\pi, r_\sigma)$ with the numerical cosmic onion model compared to using either a linear infall profile or constant LOS velocity dispersion. This complete description of redshift space distortions has the potential to provide a reliable reconstruction of the primary halo mass from $n_{obs}^z(r_\pi, r_\sigma)$ observed for a given set of stacked clusters, and given an improved model for the predicted density in real space could be used to accurately constrain the dynamic halo mass from the redshift space galaxy distribution around a cluster in the quasi-linear regime.

In this work the uncertainty on cluster mass was estimated with all other halo parameters fixed, and was found to be approximately 2% at the 2σ confidence level for a halo mass of $\sim 10^{13}$ $\mathrm{M}_{solar}h^{-1}$ as shown in figure 5.7. However in practice the accuracy of these constraints depends on how many free parameters are considered in the halo occupation distribution, as some are degenerate with the cluster mass.

5.3.3 Comparison with simulations

In order to provide a direct visual comparison of predictions from the numerical cosmic onion model discussed previously, the redshift space number density is calculated using various inputs for both the galaxy infall profile and velocity dispersion for clusters with two different primary halo masses. The galaxy density $\rho_{gal}^z(r_\pi, r_\sigma)$ is obtained using the linear galaxy infall model with a scale dependent velocity dispersion from the coherence model, the infall velocity described by the transition model with a constant LOS velocity dispersion, and finally the combined predictions for $v_r^{\rm gal}(r)$ and $\sigma_{\rm los}^{\rm gal}(r_\pi, r_\sigma)$ from the transition and coherence models, respectively. These results are then compared with the average galaxy density in redshift space observed around stacked clusters from the simulations, for

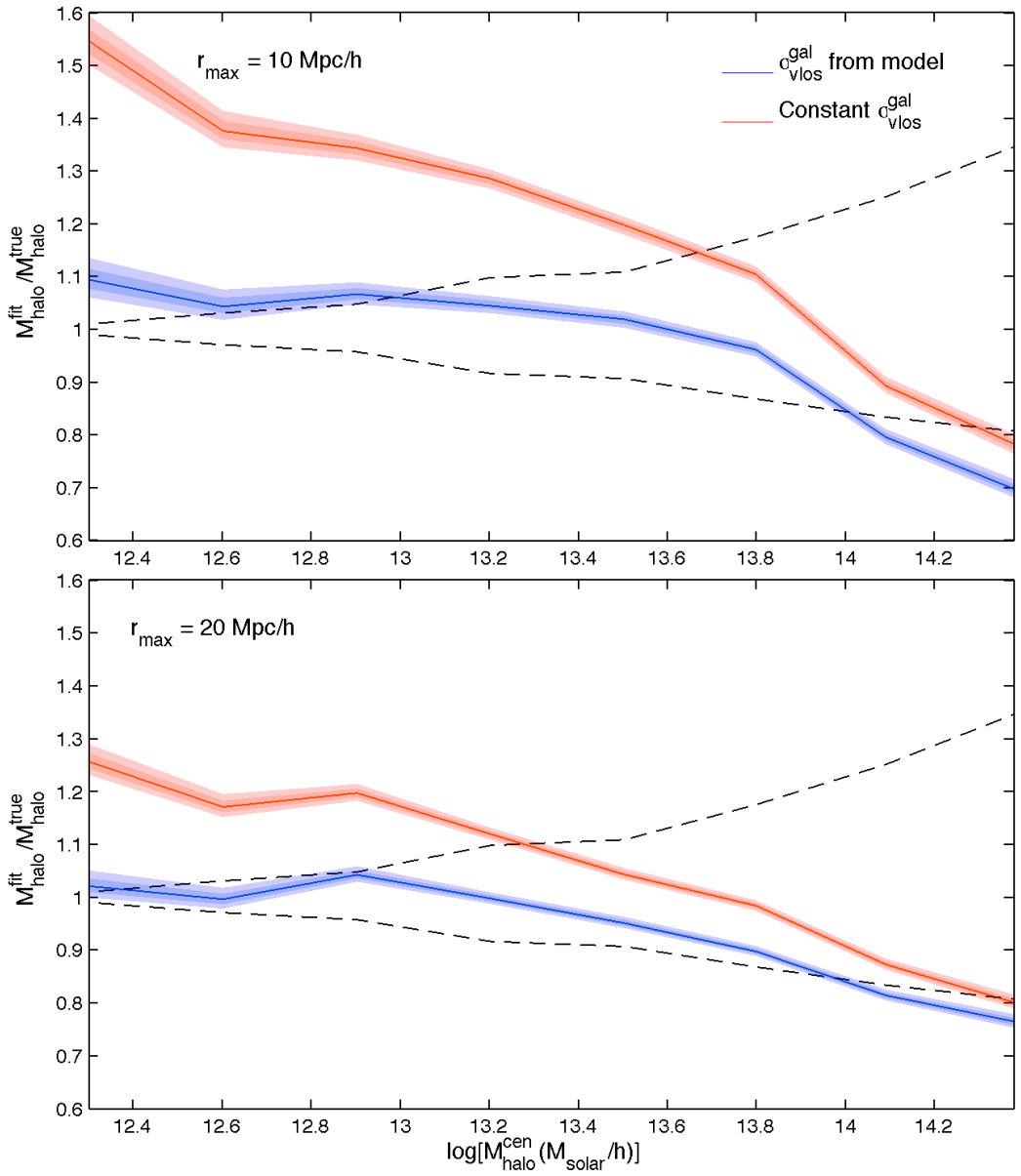

Figure 5.7. Primary halo mass constraints for stacked clusters from the simulations as a function of true halo mass, fitted from the observed galaxy count in redshift space. The ratio of the fitted halo mass to the true value is given for the numerical cosmic onion model, using both the coherence model prediction (blue line) and a constant (red line) galaxy LOS velocity dispersion. Constraints corresponding to 68% and 95% confidence are indicated by shaded regions around the fitted values for each velocity dispersion model. Results obtained by fitting out to a maximum radius of 10 (top) and 20 (bottom) Mpch^{-1} are shown, with dashed lines marking the upper and lower boundaries of each halo mass bin. Note that the figure labels $M^{\rm fit}_{\rm halo} = M^{\rm fit}_{\rm ph}$, $M^{\rm true}_{\rm halo} = M^{\rm true}_{\rm ph}$ and $M^{\rm cen}_{\rm halo} = M_{\rm ph}$.

the corresponding primary halo mass bins.

Figure 5.8 shows the redshift space galaxy density predicted for the various inputs to the cosmic onion model described above, compared to that measured from stacked clusters in the simulations. Results are given for two different primary halo mass bins, with the average $\rho^z_{gal}(r_\pi, r_\sigma)$ calculated for each dataset by dividing the observed galaxy density by the total number of clusters stacked. It can be seen that the most noticeable variation between the model predictions using different galaxy infall and velocity dispersion descriptions occurs close to the primary halo, which is unsurprising given that the ratios of $n^z_{gal}(r_\pi, r_\sigma)$ for both inputs shown in figures 5.4 and 5.5 become close to unity on larger scales. Comparison with the simulations indicates that, particularly for the higher primary halo mass bin, the predicted $\rho^z_{gal}(r_\pi, r_\sigma)$ from the cosmic onion model is considerably more accurate below a radius of ~ 10 Mpch^{-1} using the inputs from both the transition and coherence models than for either the linear description of galaxy infall or a constant LOS velocity dispersion, demonstrating that the models presented in this work provide a significant improvement over these alternatives when calculating the galaxy distribution in redshift space on quasi-linear scales around a cluster.

5.4 Varying the halo occupation distribution

5.4.1 Galaxy density and infall

Up to this point it has been assumed that the HOD parameters are known, and the values used to calculate the predictions for galaxy infall and velocity dispersion have been the same as those which were defined earlier when populating the dark matter simulations. However in the case of real data there will be a certain amount of uncertainty in these parameters, and therefore it is vital to determine the dependence of both the transition and coherence model predictions on the HOD used to describe the galaxy population within a halo of given mass. In order to ascertain which of the parameters have a significant effect on the galaxy density and infall velocity profiles, these were calculated from the transition model using the true values from the simulations and then each parameter varied in turn to observe the resulting changes in $\rho^{tot}_{gal}(r)$ and $v_r^{\rm gal}(r)$. The amount by which the individual parameters are varied is determined by the errors stated in Zehavi et al. (2011) for the given luminosity threshold, and the galaxy density and infall velocity is calculated using values corresponding to the 3σ upper and lower confidence limits of that used in the

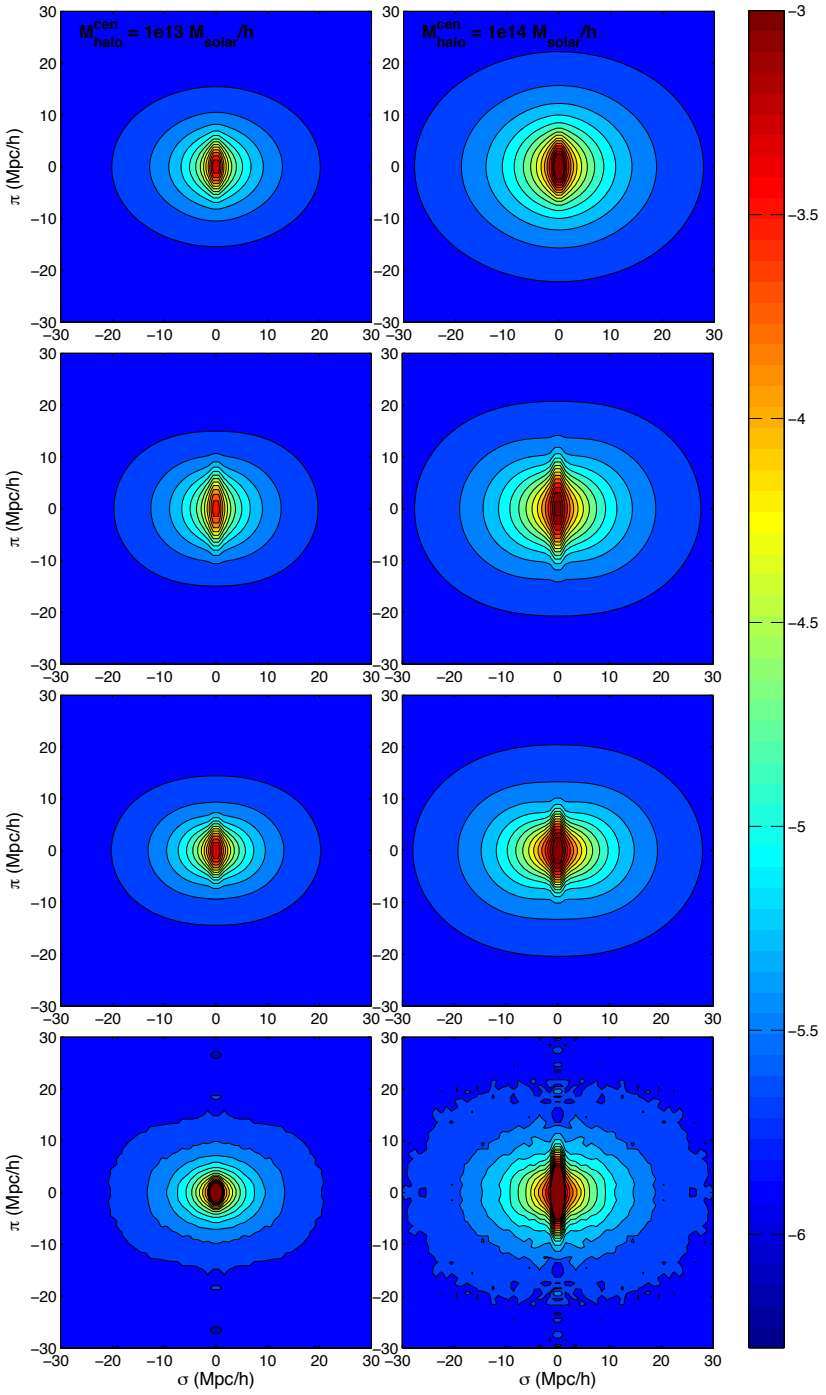

Figure 5.8. Galaxy number density in redshift space for clusters with different primary halo masses, as a function of position relative to the cluster centre. Predictions are shown for the numerical cosmic onion model using (from top to bottom) the linear galaxy infall model with velocity dispersion described by the coherence model, the transition galaxy infall model with a constant LOS velocity dispersion, and the transition and coherence models combined to provide a full description of galaxy infall and velocity dispersion on quasi-linear scales. Measurements of the average galaxy number density from stacked clusters in the simulations (bottom) are given for comparison. Results are shown for two different primary halo masses of 1×10^{13} (left panels) and 1×10^{14} (right panels) $\mathrm{M}_{solar}h^{-1}$. The colour bar represents a logarithmic scale of the galaxy number density in units of $\mathrm{Mpc}^{-3}h^3$, and the figure labels $\pi = r_\pi$, $\sigma = r_\sigma$ and $M_{\mathrm{halo}}^{\mathrm{cen}} = M_{\mathrm{ph}}$.

simulations. In the cases where these ranges represent an unphysical HOD, the minimum or maximum possible parameter value is used. The resulting predictions for $\rho_{gal}^{tot}(r)$ and $v_r^{\rm gal}(r)$ will then be compared, to indicate whether or not the transition model is sensitive to possible variations in the given parameter.

Figure 5.9 shows the dependence of galaxy density and infall velocity predicted by the transition model on each of the HOD parameters, with results given for two different primary halo masses. The relation between parent halo mass and galaxy population is also included here, to demonstrate the function that each individual parameter has in calculating the halo occupation statistics. It can be seen that in all cases that the variation within 3σ confidence limits has a relatively small effect on the galaxy density and infall profiles, however it has been shown previously in this chapter that halo mass constraints obtained using the cosmic onion model are extremely sensitive to changes in the real space density and therefore it is important to consider these effects arising from uncertainty in the HOD. There is an observed dependence for galaxy density and infall velocity predicted by the transition model on two out of the five parameters, where it can be seen that the variations in both M_{min} and M_1' produce distinct changes in the density profile, although this effect is less noticeable for the infall velocity. The uncertainty in these parameters would therefore need to be taken into account when applying the cosmic onion model to redshift survey data, in order to obtain accurate primary halo mass constraints from the galaxy distribution in redshift space around clusters.

5.4.2 Velocity dispersion components

The effects of varying the HOD on both galaxy density and infall profiles has been described above, however the velocity dispersion will also potentially show a dependence on these parameters. The expected galaxy population is used in the coherence model calculations to weight the different contributions to galaxy velocity dispersion when integrating over secondary halo mass, and therefore changes in the HOD could have a potential effect on all three components which contribute to the total predicted $\sigma_{\rm los}^{\rm gal}(r_\pi, r_\sigma)$. In order to determine the changes which result in the galaxy velocity dispersion which arises from halo motions along both the radial and tangential directions, and that which occurs due to virial motion within these halos, each of the HOD parameters are varied in turn across the same ranges that were used previously and the different components of the velocity dispersion calculated in each case. The results are then compared to ascertain the sensi-

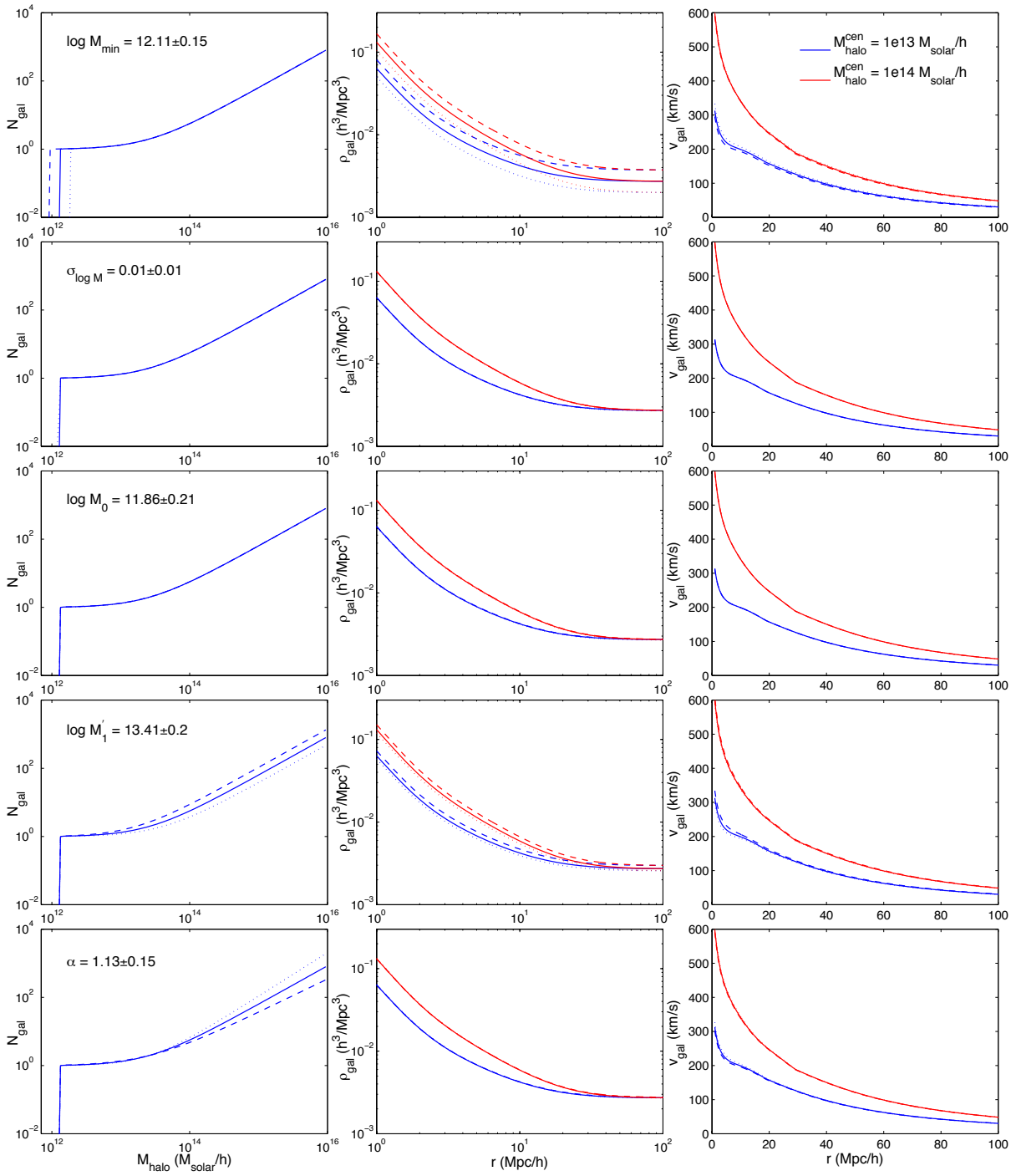

Figure 5.9. Galaxy population as a function of parent halo mass (left panels), galaxy density (middle panels) and infall velocity (right panels) profiles as predicted by the transition model for two different primary halo masses of 1×10^{13} (blue lines) and 1×10^{14} (red lines) $\mathrm{M}_{solar} h^{-1}$. Dashed and dotted lines show the effect of decreasing and increasing individual HOD parameters respectively, with results given for each of the five parameters (from top to bottom) in the HOD used to populate the simulations. Note that the figure labels $M_{\rm halo} = M_{\rm par}$ and $M_{\rm halo}^{\rm cen} = M_{\rm ph}$.

tivity of both the coherence and virial model predictions to changes in the HOD, and the effect which arises from varying individual parameters.

Figure 5.10 shows the dependence of all three components which contribute to the predicted overall galaxy velocity dispersion on each of the HOD parameters, with results given for two different primary halo masses. It can be seen that, in the case of both the radial and tangential velocity dispersion which arises from halo motions, there seems to be very little effect from varying any of the parameters on the coherence model predictions. The contribution from galaxy virial motion however displays a significant dependence on the HOD, with changes in M_{min}, M_1' and α all producing a substantial variation in the predicted velocity dispersion profile. The uncertainty in these parameters would therefore need to be included when calculating the redshift space galaxy distribution around clusters using the cosmic onion model in the case of real data, although the effects which occur due to changes in α are small in comparison to the other parameters and could therefore potentially be considered negligible. However, as it has been shown that the variation of M_{min} and M_1' has a noticeable effect on the predicted velocity dispersion component contributed by galaxy virial motion, in addition to producing changes in the density and infall velocity profiles, the uncertainty in both of these parameters would need to be accounted for in order to provide an accurate description of the redshift space galaxy distribution around a cluster using the numerical cosmic onion model.

5.4.3 Inclusion of parameter uncertainty

It has been shown that variations in two of the HOD parameters, M_{min} and M_1', have the potential to significantly effect the galaxy distribution in redshift space predicted by the cosmic onion model for a cluster of given primary halo mass. A simple method by which to include the uncertainty in the HOD when reconstructing halo mass for stacked clusters in the simulations would be to marginalise over these parameters during the fitting process, and obtain the cluster mass constraints using the maximum likelihood method as described previously. In the case of real data however, observations of clusters in a redshift survey would be stacked according to their galaxy population rather than primary halo mass, and therefore the predicted redshift space galaxy count would need to be calculated by summing the contributions from a range of cluster masses. The resulting galaxy count would be obtained by evaluating $n^z_{gal}(r_\pi, r_\sigma)$ for different halo masses and then combining these predictions, assuming that they follow a distribution that corresponds to the Poisson

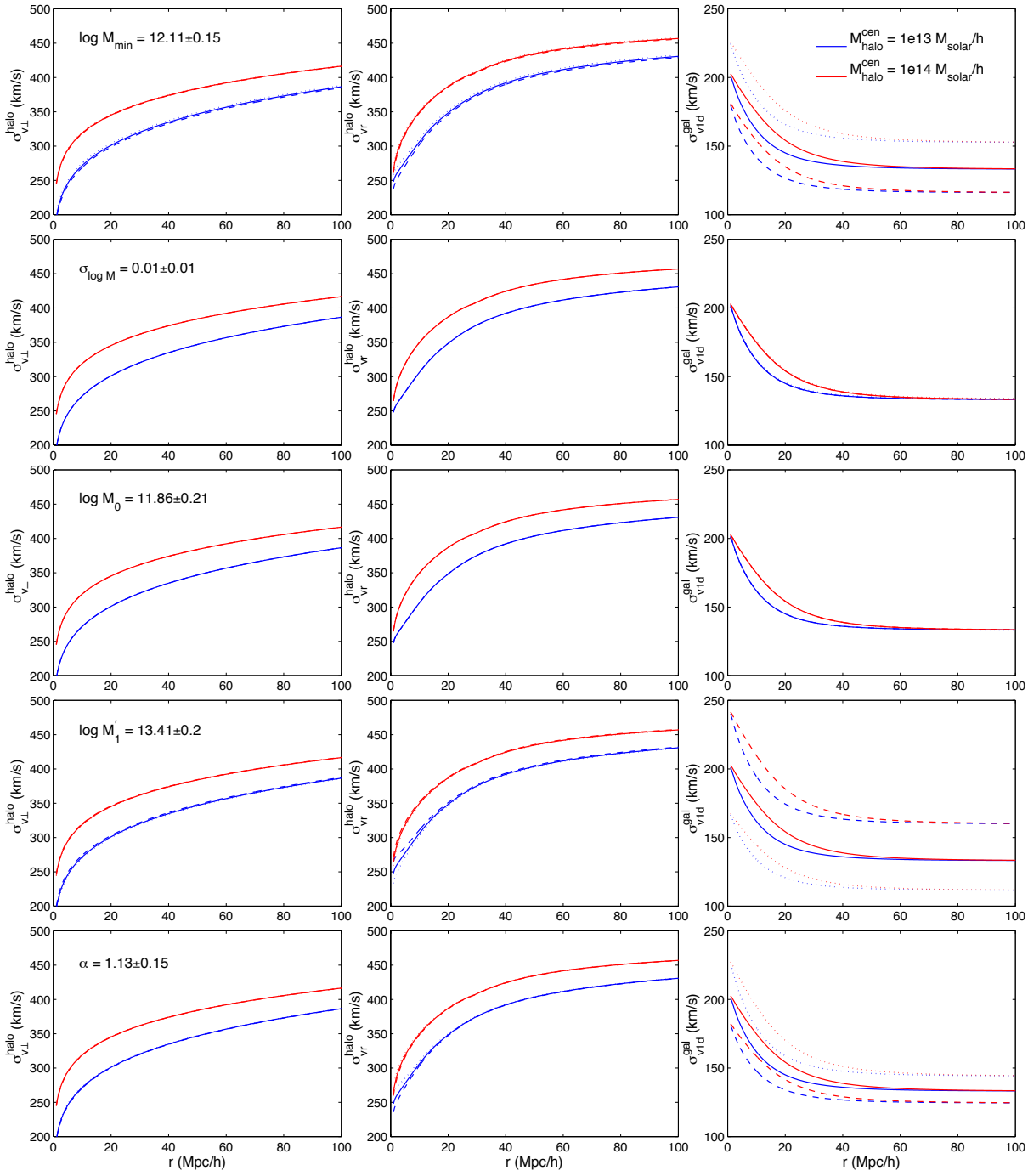

Figure 5.10. Velocity dispersion profiles for secondary halos as predicted by the coherence model in both the tangential (left panels) and radial (middle panels) directions, and the one dimensional galaxy velocity dispersion profile (right panels) as predicted by the virial model for two different primary halo masses of 1×10^{13} (blue lines) and 1×10^{14} (red lines) $\mathrm{M}_{solar}h^{-1}$. Dashed and dotted lines show the effect of decreasing and increasing individual HOD parameters respectively, with results given for each of the five parameters (from top to bottom) in the HOD used to populate the simulations. Note that the figure labels $\sigma_{vr}^{\mathrm{halo}} = \sigma_{r}^{\mathrm{hm}}$, $\sigma_{v\perp}^{\mathrm{halo}} = \sigma_{\perp}^{\mathrm{hm}}$, $\sigma_{\mathrm{v1d}}^{\mathrm{gal}} = \sigma_{\mathrm{1d}}^{\mathrm{vir}}$ and $M_{\mathrm{halo}}^{\mathrm{cen}} = M_{\mathrm{ph}}$.

statistics used to describe the number of galaxies in a parent halo of given mass. This would then be compared to the galaxy count in redshift space observed for a given dataset, and the parameters M_{min} and M_1' fitted using a maximum likelihood method to obtain constraints on the HOD as apposed to the cluster mass. This could then be used to infer the mean primary halo mass for the specified galaxy population bin, thus providing a reconstruction of the dynamic cluster mass from redshift space distortions measured in the survey data.

5.5 Application to redshift survey data

5.5.1 Testing General Relativity

The ability to obtain accurate primary halo mass constraints from the redshift space galaxy distribution around a cluster has important applications to performing tests of General Relativity, as the dynamic halo mass provides a probe of the gravitational potential Ψ as discussed in the introductory chapter. The cluster mass which is reconstructed from observations of galaxy infall can be compared with constraints obtained from gravitational lensing, which in the framework of GR should be consistent with one another. If there is a difference seen between the dynamic and lensing halo mass, then this would provide evidence of a deviation from the theory of GR. It has been shown that the numerical cosmic onion presented here could potentially be used to obtain cluster mass constraints from redshift space distortions on quasi-linear scales, and therefore would provide a way to measure the potential Ψ over a range of distances from the cluster centre indicating the scale at which any observed deviations from GR begin to take effect.

5.5.2 Modified gravity model constraints

Should the observations described above indicate that a correction to GR needs to be made, then the scales on which a difference is seen when reconstructing halo mass from the effects of lensing and redshift space distortions would be of vital importance in determining the modified gravity theories which could be used to explain these measurements. Many of these theories employ a screening mechanism which reduces their predictions to those of GR in regions of sufficiently high density, and the scale at which deviations from GR were observed for a given cluster mass would provide a means of either confirming or excluding a particular MG theory. In several of these frameworks the screening mechanism is predicted

to take effect at distances of a few tens of Mpch^{-1} from the primary halo for typical cluster masses, and therefore the ability to effectively model the galaxy density in redshift space on these scales is essential in order to obtain reliable halo mass constraints and compare these with results from gravitational lensing. The techniques introduced here to model the cosmic onion have been shown to provide an improvement on methods currently used to describe the galaxy infall and velocity dispersion around a cluster in the quasi-linear regime, and therefore could potentially be applied to redshift survey data not only for the purposes of testing GR, but also constraining the alternative MG theories.

5.6 Conclusions

In this chapter the models for galaxy infall and velocity dispersion which were previously presented have combined to provide a description of the redshift space distortions observed around a cluster, and how these vary with primary halo mass. The approach taken here was to use a numerical method to apply the RSD to the predicted galaxy distribution in real space, in order to model the cosmic onion for a given cluster mass. The redshift space galaxy density was calculated using this method for various different halo masses, and the results compared with those measured from stacked clusters in the simulations. The model was then used to fit the primary halo mass from the galaxy distribution in redshift space for various different datasets, and the constraints compared to the true value in order to establish if the cluster mass had been correctly reconstructed. These halo mass constraints were obtained using a variety of different galaxy infall and velocity dispersion inputs to the cosmic onion model, to determine the effect on the resulting reconstructed cluster mass. It was shown that both the transition and coherence models introduced here provided a significant improvement over the descriptions for galaxy infall and velocity dispersion which are currently used, when obtaining halo mass constraints from the redshift space distortions on quasi-linear scales around a cluster.

The numerical cosmic onion model described above could be potentially improved by examining a number of factors, which will be left as future work. Firstly, the model used to predict the galaxy distribution in real space to which the RSD are applied has been shown to strongly effect the cluster mass constraints fitted from $n^z_{obs}(r_\pi, r_\sigma)$ using the cosmic onion model, and inaccuracies in the density profile were seen to produce a bias in the reconstructed primary halo mass, especially for large clusters. A more precise method

for modelling the real space galaxy distribution would therefore be required in order to obtain reliable halo mass constraints in these cases, before this technique could be applied to real data. It was also demonstrated that the use of a grid with finite resolution in the numerical method used to calculate the cosmic onion could result in a slight bias in the reconstructed halo mass for smaller clusters, and it would therefore be useful to investigate the possibility of increasing the number of pixels in the grid with the aim of finding an optimum resolution which wouldn't lengthen the runtime by too great a degree. In addition to this, it was shown that a small bias was produced in the cluster mass constraints due to inaccuracies in the galaxy LOS velocity dispersion provided by the coherence model, however both this and the infall profile obtained from the transition model may be improved with the development of a better description for the predicted density profiles which are used in these calculations when integrating over secondary halo mass. Finally, it would be helpful to examine in detail the effect of uneven distributions across the wider halo mass bins used to stack clusters from the simulations, and whether this could be accounted for when modelling the cosmic onion.

In order to apply the numerical cosmic onion model to redshift survey data, the uncertainty within the HOD would need to be accounted for when constraining halo mass from the galaxy distribution in redshift space for stacked clusters in the observations. This could be achieved by fitting the parameters which have been shown to effect the predicted $n^z_{gal}(r_\pi, r_\sigma)$ for a specified galaxy population bin, and using this to infer the mean primary halo mass for the given dataset. It would also be essential to investigate the potential redshift dependence of both the galaxy infall and velocity dispersion obtained from the transition and coherence models respectively, as these have only currently been compared to simulations at a single redshift. It has been demonstrated that, given the suggested improvements summarised here, the numerical cosmic onion model presented in this chapter has the potential to provide accurate constraints on the primary halo mass from the redshift space distortions observed around clusters in the quasi-linear regime, which could be combined with measurements obtained from gravitational lensing in order to perform a test of General relativity and also differentiate between the various modified gravity theories.

Chapter 6

Conclusions

In this thesis, several models have been introduced which describe different aspects of galaxy dynamics around clusters in the quasi-linear regime. Galaxy infall and velocity dispersion models have been developed and tested using N-body simulation data, and used to predict the cluster-galaxy redshift space correlation function, or cosmic onion, for a given primary halo mass. The motivation of this work is to develop a robust technique to constrain dynamic cluster mass from the observed cosmic onion, which can then be compared with gravitational lensing measurements in order to perform tests of General Relativity.

6.1 Comparison with other work

Since this thesis was begun, several other works have been published on modelling the infall onto clusters of galaxies, the two most relevant are by Zu & Weinberg (2013) and Lam et al. (2013). In this section the underlying assumptions and N-body simulations used in these works will be discussed, and the modelling techniques and performance compared to the work presented in this thesis.

Zu & Weinberg (2013) prescribe a model for the galaxy-cluster redshift space correlation function (ξ^s_{cg}), so that the "Galaxy infall kinematics" (GIK) can be recovered. They calibrate and test this model using the Millennium simulation for the dark matter (2160^3 dark matter particles with $M_p = 8.610^8 h^{-1} M_{\rm solar}$ in a periodic box $500h^{-1}$ Mpc on a side),

populated using a semi-analytic model using an empirical galaxy formation recipe along the merger trees of dark matter halos as described by De Lucia & Blaizot (2007). They use a skewed t-distribution to model the velocity distribution as a function of radial and tangential velocity, having found other parameterisations (including sums of Gaussians) inadequate. They end up with a 7 component model at every radius from the cluster centre, depending on the virialized fraction, the velocity dispersion of the virialized component, the characteristic infall velocity, two velocity dispersions of the infall component (in the radial and tangential directions), a skewness parameter and a kurtosis parameter. They use this model to fit to the observed ξ^s_{cg} in SDSS and reconstruct the infall as a function of radius.

The paper by Lam et al. (2013) appeared just after the Zu & Weinberg (2013), and has some similarities, but the goal of the paper is to test modified gravity models with a small number of free parameters, rather than to reconstruct the infall velocity as a function of radius (with a large number of free parameters). They use the simulations of Valageas and Nishimichi ($1024h^{-1}$ Mpc on a side with 2048^3 particles) and a halo model for the galaxy positions. They use the spherical collapse model for the infall at small radii and assume a Gaussian distribution of the velocity dispersion in the radial and tangential directions. They consider $f(R)$ and DGP modified gravity models and propagate the effects of modifying gravity into the halo model.

The papers described above differ from the work presented here in several respects. The simulation details are compared in table 6.1. All three simulations are roughly comparable and differences are likely to be subdominant to the other assumptions. We and Lam et al. (2013) use a halo model approach to populating the simulations whereas Zu & Weinberg (2013) use semi-analytic modelling, which is superior because it takes into account the merger history in the simulation. We model the infall velocity using the spherical evolution model on small scales and linear halo streaming on large scales, bridged by a simple empirical transition model. Zu & Weinberg (2013) leave the infall as a free parameter as a function of radius, whereas Lam et al. (2013) use an empirical model motivated by the spherical collapse model. We all considered the velocity dispersion separately in the radial and tangential directions.

	This thesis	Zu & Weinberg	Lam et al
Simulations used	GADGET-2	Millennium	Valageas and Nishimichi
Number of particles	1024^3	2160^3	2048^3
Simulation box side	936 Mpc/h	500 Mpc/h	1024 Mpc/h
Galaxy biasing	Halo model	Semi-analytic modelling	Halo model

Table 6.1. Properties of the N-body simulations used by Zu & Weinberg (2013) and Lam et al. (2013), compared to those used for the work presented in this thesis.

6.2 Summary of work

The N-body simulations of dark matter used in this work were populated with galaxies using a halo occupation distribution (HOD) model, and this process is described in chapter 2. The populated simulations were used to generate mock observations of the cosmic onion, by stacking galaxy clusters of a given primary halo mass. Direct measurements of galaxy infall and velocity dispersion were also obtained from the stacked cluster datasets, in order to develop and test models which predict these dynamics in the quasi-linear regime. The dark matter halo catalogue for the N-body simulations was populated using a set of HOD parameters which correspond to a given absolute magnitude, allowing mock observations to be generated which emulate current galaxy redshift surveys. The process of creating a galaxy catalogue is described in detail, and various properties of the simulations such as the halo mass function and matter overdensity field are presented in chapter 2. Observations of the cosmic onion measured from stacked datasets in the simulations are used in subsequent work, in order to develop a method to reconstruct the dynamic cluster mass which could potentially be applied to data from galaxy redshift surveys.

In chapter 3, a model was developed which describes the effective galaxy infall velocity around a cluster, and its dependence on primary halo mass. This method, known as the transition model, combines predictions for halo streaming motions from linear theory with the description of density perturbation growth provided by the spherical evolution model. The predictions for galaxy infall onto clusters obtained using linear theory are only valid on sufficiently large scales, while the spherical evolution model in the limit of complete collapse provides a description which only applies at distances close to the primary halo. In order to fully describe galaxy dynamics around a cluster, a method is required which accurately predicts infall on quasi-linear scales. A model is presented in chapter 3 which

describes the transition between small and large scale behaviour for galaxy infall onto clusters, which uses a fitting function to predict galaxy infall in this regime. The primary halo mass dependence of the fitting function parameters was determined using the galaxy infall profiles measured from stacked clusters in the simulations.

The transition model was then combined with a numerical method for applying a velocity profile to the galaxy density distribution around a cluster, in order to predict the redshift space distortions which result from galaxy infall towards the primary halo. This method was used to obtain predictions of the cosmic onion for various different cluster masses, applying the transition model for galaxy infall combined with a line of sight velocity dispersion which was measured directly from the simulations. The effective galaxy velocity profiles predicted by the transition model showed good agreement with the simulations for the specified primary halo masses, indicating that it provides an accurate description of infall in the quasi-linear regime. Comparison with simulations also showed a qualitative agreement with model predictions for the cosmic onion, however also demonstrated how this is significantly affected by galaxy velocity dispersion. It can therefore be concluded that a method for predicting velocity dispersion on quasi-linear scales is required, in order to accurately describe the galaxy distribution in redshift space around a cluster.

In chapter 4, a model was presented which describes the velocity dispersion of galaxies around a cluster, and how this depends on distance from the primary halo. This model was developed by individually considering both the dynamics of secondary halos and the virial motion of galaxies that they contain, and how these effects combine to produce the overall galaxy velocity dispersion. The line of sight component of this effect was then calculated as a function of position relative to the cluster centre, with predictions given for different primary halo masses. Comparison with results observed for stacked clusters in the simulations showed a good agreement with these predictions, demonstrating that the model provides an accurate description of the galaxy velocity dispersion and its scale dependence. The predicted velocity dispersion was then applied to the numerical cosmic onion model in the form of a Gaussian convolution, in order to obtain a description of the galaxy distribution in redshift space. It was demonstrated that by combining these velocity dispersion predictions with the transition model for galaxy infall, a complete description of the redshift space distortions around a cluster is provided which is accurate in the quasi-linear regime.

In chapter 5, the models for galaxy infall and velocity dispersion described above were combined in order to predict the redshift space distortions around a cluster, for a given primary halo mass. The approach taken was to calculate the predicted galaxy distribution in real space, and apply the RSD using a numerical method to model the cluster-galaxy redshift space correlation function, or cosmic onion. Predictions were obtained for several different primary halo masses, and compared with the results observed from stacked clusters in the simulations. The galaxy distribution in redshift space was measured for various different cluster masses, and the numerical cosmic onion model used to fit the primary halo mass for each dataset. The constraints were then compared to the true cluster mass, in order to determine if it had been accurately reconstructed. Primary halo mass constraints were obtained using several different methods to calculate the galaxy infall and velocity dispersion inputs for the cosmic onion model, to establish how this affected the resulting reconstructed cluster mass. It was demonstrated that applying the transition and coherence models presented here results in a significant improvement on other methods used to predict galaxy infall and velocity dispersion, when constraining primary halo mass from the cosmic onion. The models introduced in this thesis were shown to provide a relatively accurate description of redshift space distortions on quasi-linear scales, and could potentially be applied to observational data in order to obtain constraints on the dynamic cluster mass.

6.3 Applications to observational data

The method proposed here could be applied to current data where spectroscopic redshifts for a large sample of cosmological redshift galaxies have been obtained, and halos identified. The relevant surveys of last decade are the 2dF Galaxy Redshift Survey and the Sloan Digital Sky Survey. The most relevant survey of the current decade is the Galaxy and Mass Assembly (GAMA) survey which measures redshifts for ∼300,000 galaxies down to $r < 19.8$ mag over ∼286 square degrees. The Extended Baryon Oscillation Spectroscopic Survey (eBOSS) survey measures redshifts of 300,000 luminous red galaxies over 7500 square degrees from $0.6 < z < 0.8$ and 189,000 emission line galaxies over 1000 square degrees over $0.6 < z < 1.0$. For this work it is particularly important to have sufficient galaxy density to identify halos, and therefore it is likely that the deeper GAMA survey would be more promising. If clusters were spherical in real space then a single well pop-

ulated cluster might be sufficient to carry out a measurement of cluster mass. However in practice clusters are elliptical and may be elongated along the line of sight, therefore, depending on the probability distribution function of cluster ellipticities, more clusters would be needed in practice. This would require further investigation in future work to quantify the trade-off between deep and wide.

Bibliography

Alimi, J.-M., Bouillot, V., Rasera, Y., Reverdy, V., Corasaniti, P.-S., Balmes, I., Requena, S., Delaruelle, X. & Richet, J.-N., 2012, *ArXiv e-prints*

Angulo, R. E., Springel, V., White, S. D. M., Cole, S., Jenkins, A., Baugh, C. M. & Frenk, C. S., 2012*a*, *MNRAS*, **425**, 2722

Angulo, R. E., Springel, V., White, S. D. M., Jenkins, A., Baugh, C. M. & Frenk, C. S., 2012*b*, *MNRAS*, **426**, 2046

Bartelmann, M. & Schneider, P., 2001, *PhysRep*, **340**, 291

Baumann, D., 2009, *ArXiv e-prints*

Baumann, D. & Peiris, H. V., 2008, *ArXiv e-prints*

Begeman, K. G., Broeils, A. H. & Sanders, R. H., 1991, *MNRAS*, **249**, 523

Bondi, H. & Gold, T., 1948, *MNRAS*, **108**, 252

Clowe, D., Bradač, M., Gonzalez, A. H., Markevitch, M., Randall, S. W., Jones, C. & Zaritsky, D., 2006, *ApJL*, **648**, L109

De Lucia, G. & Blaizot, J., 2007, *MNRAS*, **375**, 2

Dunkley, J., Komatsu, E., Nolta, M. R., Spergel, D. N., Larson, D., Hinshaw, G., Page, L., Bennett, C. L., Gold, B., Jarosik, N., Weiland, J. L., Halpern, M., Hill, R. S., Kogut, A., Limon, M., Meyer, S. S., Tucker, G. S., Wollack, E. & Wright, E. L., 2009, *ApJSS*, **180**, 306

Dyson, F. W., Eddington, A. S. & Davidson, C., 1920, *Philosophical Transactions of the Royal Society of London Series A*, **220**, 291

Friedmann, A., 1922, *Zeitschrift fur Physik*, **10**, 377

Gunn, J. E. & Gott, III, J. R., 1972, *ApJ*, **176**, 1

Guth, A. H., 1981, *PRD*, **23**, 347

Hamilton, A. J. S., Kumar, P., Lu, E. & Matthews, A., 1991, *ApJL*, **374**, L1

Heitmann, K., White, M., Wagner, C., Habib, S. & Higdon, D., 2010, *ApJ*, **715**, 104

Heymans, C., Van Waerbeke, L., Miller, L., Erben, T., Hildebrandt, H., Hoekstra, H., Kitching, T. D., Mellier, Y., Simon, P., Bonnett, C., Coupon, J., Fu, L., Harnois Déraps, J., Hudson, M. J., Kilbinger, M., Kuijken, K., Rowe, B., Schrabback, T., Semboloni, E., van Uitert, E., Vafaei, S. & Velander, M., 2012, *MNRAS*, **427**, 146

Hildebrandt, H., Viola, M., Heymans, C., Joudaki, S., Kuijken, K., Blake, C., Erben, T., Joachimi, B., Klaes, D., Miller, L., Morrison, C. B., Nakajima, R., Verdoes Kleijn, G., Amon, A., Choi, A., Covone, G., de Jong, J. T. A., Dvornik, A., Fenech Conti, I., Grado, A., Harnois-Déraps, J., Herbonnet, R., Hoekstra, H., Köhlinger, F., McFarland, J., Mead, A., Merten, J., Napolitano, N., Peacock, J. A., Radovich, M., Schneider, P., Simon, P., Valentijn, E. A., van den Busch, J. L., van Uitert, E. & Van Waerbeke, L., 2017, *MNRAS*, **465**, 1454

Hoyle, F., 1948, *MNRAS*, **108**, 372

Hubble, E., 1929, *Proceedings of the National Academy of Science*, **15**, 168

Jee, M. J., Tyson, J. A., Schneider, M. D., Wittman, D., Schmidt, S. & Hilbert, S., 2013, *ApJ*, **765**, 74

Juszkiewicz, R., Springel, V. & Durrer, R., 1999, *ApJL*, **518**, L25

Kuijken, K., Heymans, C., Hildebrandt, H., Nakajima, R., Erben, T., de Jong, J. T. A., Viola, M., Choi, A., Hoekstra, H., Miller, L., van Uitert, E., Amon, A., Blake, C., Brouwer, M., Buddendiek, A., Fenech Conti, I., Eriksen, M., Grado, A., Harnois-Déraps, J., Helmich, E., Herbonnet, R., Irisarri, N., Kitching, T., Klaes, D., Labarbera, F., Napolitano, N., Radovich, M., Schneider, P., Sifón, C., Sikkema, G., Simon, P., Tudorica, A., Valentijn, E., Verdoes Kleijn, G. & van Waerbeke, L., 2015, *ArXiv e-prints*

Lam, T. Y., Schmidt, F., Nishimichi, T. & Takada, M., 2013, *PRD*, **88**(2), 023012

Lyth, D. H. D. H. & Riotto, A. A., 1999, *PhysRep*, **314**, 1

Maldacena, J., 2003, *Journal of High Energy Physics*, **5**, 013

Mandelbaum, R., Seljak, U. & Hirata, C. M., 2008, *JCAP*, **8**, 6

Misner, C. W., Thorne, K. S. & Wheeler, J. A., 1973, *Gravitation*

Mo, H. J. & White, S. D. M., 1996, *MNRAS*, **282**, 347

Navarro, J. F., Frenk, C. S. & White, S. D. M., 1996, *ApJ*, **462**, 563

Nityananda, R. & Padmanabhan, T., 1994, *MNRAS*, **271**, 976

Padmanabhan, T., 1993, *Structure Formation in the Universe*

Peacock, J. A., 1999, *Cosmological Physics*

Peebles, P. J. E., 1980, *The large-scale structure of the universe*

Penzias, A. A. & Wilson, R. W., 1965, *ApJ*, **142**, 419

Planck Collaboration, Ade, P. A. R., Aghanim, N., Armitage-Caplan, C., Arnaud, M., Ashdown, M., Atrio-Barandela, F., Aumont, J., Baccigalupi, C., Banday, A. J. & et al., 2014*a*, *A&A*, **571**, A15

Planck Collaboration, Ade, P. A. R., Aghanim, N., Armitage-Caplan, C., Arnaud, M., Ashdown, M., Atrio-Barandela, F., Aumont, J., Baccigalupi, C., Banday, A. J. & et al., 2014*b*, *A&A*, **571**, A16

Planck Collaboration, Ade, P. A. R., Aghanim, N., Arnaud, M., Ashdown, M., Aumont, J., Baccigalupi, C., Banday, A. J., Barreiro, R. B., Bartlett, J. G. & et al., 2015, *ArXiv e-prints*

Prada, F., Klypin, A. A., Cuesta, A. J., Betancort-Rijo, J. E. & Primack, J., 2012, *MNRAS*, **423**, 3018

Refregier, A., Amara, A., Kitching, T. D. & Rassat, A., 2011, *A&A*, **528**, A33

Riess, A. G., Filippenko, A. V., Challis, P., Clocchiatti, A., Diercks, A., Garnavich, P. M., Gilliland, R. L., Hogan, C. J., Jha, S., Kirshner, R. P., Leibundgut, B., Phillips, M. M., Reiss, D., Schmidt, B. P., Schommer, R. A., Smith, R. C., Spyromilio, J., Stubbs, C., Suntzeff, N. B. & Tonry, J., 1998, *AJ*, **116**, 1009

Roberts, M. S. & Whitehurst, R. N., 1975, *ApJ*, **201**, 327

Robertson, H. P., 1935, *ApJ*, **82**, 284

Rubin, V. C. & Ford, Jr., W. K., 1970, *ApJ*, **159**, 379

Rubin, V. C., Ford, W. K. J. & . Thonnard, N., 1980, *ApJ*, **238**, 471

Ryden, B., 2003, *Introduction to cosmology*

Schechter, P. L., 1980, *AJ*, **85**, 801

Schneider, P., 2006, *Extragalactic Astronomy and Cosmology*

Sheth, R. K., Diaferio, A., Hui, L. & Scoccimarro, R., 2001, *MNRAS*, **326**, 463

Sheth, R. K. & Tormen, G., 1999, *MNRAS*, **308**, 119

Springel, V., White, S. D. M., Jenkins, A., Frenk, C. S., Yoshida, N., Gao, L., Navarro, J., Thacker, R., Croton, D., Helly, J., Peacock, J. A., Cole, S., Thomas, P., Couchman, H., Evrard, A., Colberg, J. & Pearce, F., 2005, *Nature*, **435**, 629

Suzuki, N., Rubin, D., Lidman, C., Aldering, G., Amanullah, R., Barbary, K., Barrientos, L. F., Botyanszki, J., Brodwin, M., Connolly, N., Dawson, K. S., Dey, A., Doi, M., Donahue, M., Deustua, S., Eisenhardt, P., Ellingson, E., Faccioli, L., Fadeyev, V., Fakhouri, H. K., Fruchter, A. S., Gilbank, D. G., Gladders, M. D., Goldhaber, G., Gonzalez, A. H., Goobar, A., Gude, A., Hattori, T., Hoekstra, H., Hsiao, E., Huang, X., Ihara, Y., Jee, M. J., Johnston, D., Kashikawa, N., Koester, B., Konishi, K., Kowalski, M., Linder, E. V., Lubin, L., Melbourne, J., Meyers, J., Morokuma, T., Munshi, F., Mullis, C., Oda, T., Panagia, N., Perlmutter, S., Postman, M., Pritchard, T., Rhodes, J., Ripoche, P., Rosati, P., Schlegel, D. J., Spadafora, A., Stanford, S. A., Stanishev, V., Stern, D., Strovink, M., Takanashi, N., Tokita, K., Wagner, M., Wang, L., Yasuda, N., Yee, H. K. C. & Supernova Cosmology Project, T., 2012, *ApJ*, **746**, 85

The Dark Energy Survey Collaboration, Abbott, T., Abdalla, F. B., Allam, S., Amara, A., Annis, J., Armstrong, R., Bacon, D., Banerji, M., Bauer, A. H., Baxter, E., Becker, M. R., Benoit-Lévy, A., Bernstein, R. A., Bernstein, G. M., Bertin, E., Blazek, J., Bonnett, C., Bridle, S. L., Brooks, D., Bruderer, C., Buckley-Geer, E., Burke, D. L., Busha, M. T., Capozzi, D., Carnero Rosell, A., Carrasco Kind, M., Carretero, J., Castander,

F. J., Chang, C., Clampitt, J., Crocce, M., Cunha, C. E., D'Andrea, C. B., da Costa, L. N., Das, R., DePoy, D. L., Desai, S., Diehl, H. T., Dietrich, J. P., Dodelson, S., Doel, P., Drlica-Wagner, A., Efstathiou, G., Eifler, T. F., Erickson, B., Estrada, J., Evrard, A. E., Fausti Neto, A., Fernandez, E., Finley, D. A., Flaugher, B., Fosalba, P., Friedrich, O., Frieman, J., Gangkofner, C., Garcia-Bellido, J., Gaztanaga, E., Gerdes, D. W., Gruen, D., Gruendl, R. A., Gutierrez, G., Hartley, W., Hirsch, M., Honscheid, K., Huff, E. M., Jain, B., James, D. J., Jarvis, M., Kacprzak, T., Kent, S., Kirk, D., Krause, E., Kravtsov, A., Kuehn, K., Kuropatkin, N., Kwan, J., Lahav, O., Leistedt, B., Li, T. S., Lima, M., Lin, H., MacCrann, N., March, M., Marshall, J. L., Martini, P., McMahon, R. G., Melchior, P., Miller, C. J., Miquel, R., Mohr, J. J., Neilsen, E., Nichol, R. C., Nicola, A., Nord, B., Ogando, R., Palmese, A., Peiris, H. V., Plazas, A. A., Refregier, A., Roe, N., Romer, A. K., Roodman, A., Rowe, B., Rykoff, E. S., Sabiu, C., Sadeh, I., Sako, M., Samuroff, S., Sánchez, C., Sanchez, E., Seo, H., Sevilla-Noarbe, I., Sheldon, E., Smith, R. C., Soares-Santos, M., Sobreira, F., Suchyta, E., Swanson, M. E. C., Tarle, G., Thaler, J., Thomas, D., Troxel, M. A., Vikram, V., Walker, A. R., Wechsler, R. H., Weller, J., Zhang, Y. & Zuntz, J., 2015, *ArXiv e-prints*

Tinker, J. L., Robertson, B. E., Kravtsov, A. V., Klypin, A., Warren, M. S., Yepes, G. & Gottlöber, S., 2010, *ApJ*, **724**, 878

Vogelsberger, M., Genel, S., Springel, V., Torrey, P., Sijacki, D., Xu, D., Snyder, G., Bird, S., Nelson, D. & Hernquist, L., 2014, *Nature*, **509**, 177

Walker, A. G., 1935, *The Quarterly Journal of Mathematics*, **6**, 81

Weinberg, D. H., Mortonson, M. J., Eisenstein, D. J., Hirata, C., Riess, A. G. & Rozo, E., 2013, *PhysRep*, **530**, 87

Weinberg, S., 1972, *Gravitation and Cosmology: Principles and Applications of the General Theory of Relativity*

Zehavi, I., Zheng, Z., Weinberg, D. H., Blanton, M. R., Bahcall, N. A., Berlind, A. A., Brinkmann, J., Frieman, J. A., Gunn, J. E., Lupton, R. H., Nichol, R. C., Percival, W. J., Schneider, D. P., Skibba, R. A., Strauss, M. A., Tegmark, M. & York, D. G., 2011, *ApJ*, **736**, 59

Zel'dovich, Y. B., 1970, *A&A*, **5**, 84

Zu, Y. & Weinberg, D. H., 2013, *MNRAS*, **431**, 3319

Zwicky, F., 1937, *ApJ*, **86**, 217

"I'd take the awe of understanding over the awe of ignorance any day"

Douglas Adams